The Raymond and Beverly Sackler
School of Physics and Astronomy
The Raymond and Beverly Sackler
Faculty of Exact Sciences
Tel Aviv University

בית הספר לפיזיקה ולאסטרונומיה
ע״ש ריימונד ובברלי סאקלר
הפקולטה למדעים מדויקים
ע״ש ריימונד ובברלי סאקלר
אוניברסיטת תל אביב

RAMAT AVIV, 69978 TEL AVIV, ISRAEL

Detector R&D towards realistic luminosity measurement at the forward region of future e^+e^- linear colliders

Thesis submitted to the Senate of Tel Aviv University
towards the degree “Doctor of Philosophy”

by

Itamar Levy

May 2019

Thesis supervisors,
Prof. **Halina Abramowicz** and
Prof. **Aharon Levy**.

The research for this thesis has been carried out in
the Particle Physics Department of Tel Aviv University, under
the supervision of Prof. **Halina Abramowicz** and Prof. **Aharon Levy**.

To my wife and daughters,

In memory of my grandma Halina.

Abstract

The luminosity measurement at a future e^+e^- linear collider will be preformed with a specialized compact calorimeter foreseen in the very forward region. The design of the luminosity calorimeter (LumiCal) is based on a tungsten-silicon sandwich calorimeter. The R&D effort by the FCAL collaboration aims towards the assembly of the full calorimeter prototype, that will serve as a realistic demonstrator for the final detector. Two methods for silicon sensor automated testing were used for the characterization of LumiCal sensor prototypes. In these measurements the total capacitance, depletion voltage, donor density and the pad dark current were measured for each pad in the sensor. A first LumiCal prototype consisting of four planes was tested at the CERN PS accelerator T9 beam. An improved compact prototype, utilizing new thin detector modules, was tested at DESY with an electron beam of 1 GeV – 6 GeV. In the tests, the sensor performance was measured, the development of the electromagnetic shower was studied and the prototype energy and position reconstruction resolution were determined. The effective Moliére radii of the two prototypes were also extracted using a parameterization of the lateral shower shape. For the first prototype it was determined to be $24.0 \pm 0.6(stat.) \pm 1.5(syst.)$ mm, while for the more compact prototype it was determined to be significantly lower, $8.2 \pm 0.1(stat) \pm 0.3(syst)$ mm. Very good agreement was obtained between data and MC simulations. The smaller effective Moliére radius reached by the compact prototype indicate that the full LumiCal will be capable, in due time, to preform the luminosity measurement with the desired precision.

Acknowledgements

First and foremost, i would like to thank my supervisors, Prof. Halina Abramowicz and Prof. Aharon Levy, in general for everything. For accepting me to your group and to the world of experimental particles physics. For taking me under your wings professionally and personally and for all of the much needed support, encouragement, assistance, patience and understand along the way.

I would like to thank my colleagues and friends from our joint office and from the experimental group, Dr. Sergey Kananov, Dr. Zhenya Gurvich, Dr. Ronen Ingbir, Dr. Iftach Sadeh, Rina Schwartz, Dr. Yiftah Silver, Dr. Adi Ashkenazi, Dr. Oleg Kuprash, Hadar Cohen, Guy Koren, Alon Joffe, Moshe Barboy, for the time we spent together, the assistance, the fruitful discussion and new ideas. I particularly would like to thank Dr. Amir Stern, Dr. Orel Guetta and Oron Rosenblat,for the friendship and support they give me during this period.

In particular i would like to thank the FCAL team in Tel Aviv that walk with me for a long time, from the icy rivers of Moscow to August heat of Tel Aviv, Dr. Yan Benhammou, Meny Ben-Moshe, Dr. Oleksandr Borysov and Dr. Marina Borysova. For the care, professional support and personal help in any matter in the world. Without you, the completion of this work and this thesis, was impossible.

I would like to thank all of the colleagues and friends from the FCAL and CLICdp collaboration, especially, to Prof. Marek Idzik, Dr. Konrad Elsener,Dr. André Sailer, Dr. Wolfgang Lange, Hans Henschel and Prof. Wolfgang Lohmann for all the help to achieve this venture.

I also would like to thank the secretariat staff of the school of physics and astronomy of Tel Aviv University, in the past and present, Sharon Feldman, Michal Nissanov, Yakira Navaty, Galia Netzer-Erlichmen, Ester Benado, Lily Almog and Riki Cohen, for all the help, always with a smile, along the way.

Last but not least, i am especially grateful to my family, to me wife Hagar and to Ela, that bear with me and support me along this never ending roller-coaster. And to our parents that allow me to take the much needed time to bring this work to its end.

This work is partly supported by the Israeli Science Foundation, the German-Israel Foundation, the EU Horizon 2020 Research and Innovation program, and the I-CORE excellence center program.

Preface

I joined the high energy experimental group, and started my research activities within the FCAL (forward calorimetry for the future electron-positron linear colliders) Collaboration at the beginning of my master degree. The work presented in this thesis is a continuation of these activities, which aim at designing and testing a compact calorimeter for the precise measurement of luminosity based on the Bhabha scattering process ($e^+e^- \to e^+e^-$).

I played a key role in the FCAL detector development efforts towards a working prototype calorimeter. The progress in the detector R&D presented here as a whole is the outcome of a group effort of the Tel Aviv University (TAU) FCAL team. I will try to outline here my personal contribution.

My activities spanned three main areas of responsibility. I developed, and had a major contribution to the upgrade of the infrastructure of the TAU silicon lab. I was responsible for the setup and data acquisition system of all the beam-test campaigns, two of which are reported in this thesis. I was the main analyser of all the beam-test data and the resulting papers are based on my results. The details of my contributions in these three areas are given below.

Silicon sensor qualification

- Based on the experience in silicon sensor testing collected during the MSc period when I built the silicon lab at TAU, a process of upgrading the facilities of the silicon lab begun. The upgrade goals were to improve the quality of the measurements and the environment in which they were done, and to gain new capabilities for sensor tests and module assembly. Most of the upgrade stages were preformed as part of the I-CORE excellence center program, that was used to create new infrastructure in the TAU detector lab. During this time I took a major part in the planning and assembling of the lab, and in purchasing of the new equipment.

- As part of the lab activities, I trained and supervised bachelor and first year MSc students in LumiCal silicon sensor measurements, with the manual system I designed during my MSc, in an effort to measure all the LumiCal silicon sensors at TAU. The results of those measurements were part of the thesis of one of the MSc students. These measurements are the base of comparison for the sensor measurements presented here.

- As part of beam-tests preparation, I organized the sensor test campaign at DESY-Zeuthen. During these tests I learned how to use the semi-automated probe-station. I prepared the experimental setup and improved the sensor measurement time. I completed the measurements of all the TAU LumiCal sensors, prepared the software tools for the analysis of the results and supervised the analysis.

- Towards the end of this period, I installed the switching system on the TAU probe-station, and adapted the CERN Labview DAQ. With the help of a system developer, I took for the first time measurements of the LumiCal silicon sensors with the automated switching system.

beam-test campaigns

- During the PhD period, I participated in a total of five campaigns. In all of them I worked on the DAQ, and system integration and synchronization, and played a key role in the setup and data taking strategy.
- In the beam-tests during 2013-2014, I prepared the DAQ and actively participated in tests of diamond and sapphire detectors for the very forward BeamCal calorimeter which requires radiation hard sensors. I prepared the framework for the analysis of these data. The results of the tests of diamond and sapphire detector were published in two papers. These results are not part of this thesis.
- One of the main challenges in the 2014 test beam was the need to join two DAQ systems into one synchronized data stream. I designed the DAQ integration principle based on an auxiliary device and wrote the DAQ software to read it. I also prepared the software to decode the auxiliary device information and use it to synchronize the data-streams from the FCAL prototype calorimeter and the tracking telescope.
- After the 2014 beam-test and based on its results, I took part in the design of a new thin LumiCal module for the 2015-2016 test beam campaigns. During this time the thin module was prepared and an alternative front-end electronic was studied.

Data analysis

- After the 2014 first LumiCal multi-layer test beam I worked on the analysis in parallel to others in the FCAL collaboration. I prepared the tools for data-stream synchronization. In my analysis, I prepared all the different stages, including particle identification, noise handling, signal reconstruction and calibration. While a few analysers studied the longitudinal shower development, I was the only one to study also the position reconstruction and to determine the calorimeter position resolution. The study of the transverse shower development and the measurement of the effective Molière radius is my original idea. I developed the method used to combine the three configurations sampled during the beam-test into one result for an effective Molière radius.
- I modified the existing LumiCal simulation software, LUCAS, to describe the 2014 test setup and later the 2016 test setup. I prepared the simulation files using the different setups, for comparison with the beam-test data. I preformed the same analysis used on the data including calibration, position reconstruction, bad pad removal and corrections on the results of the simulation.
- While preparing this thesis, I adapted and improved the analysis used for the 2014 beam-test to the data recorded during the 2016 test beam, with the help of my colleagues Dr. Oleksandr Borysov and Dr. Marina Borysova. The preliminary results were so interesting that I took the strategic decision to make them part of the thesis at the cost of delaying its completion. The data from the 2016 beam-test turned out to be more involved due to the new sensor module design and new electronic readout. It required to incorporate a study of the layers misalignment, bad channels list, and inefficiency to small signal response in the analysis, all of which I also had

to include in the simulation. For the system calibration I suggested a solution using a cosmic test stand, up to a point where it became clear that a non-linear calibration for the readout is needed.

I presented my results in numerous international meetings. The results were regularly reported at the FCAL collaboration meetings, which takes place twice a year. They were also presented at the CLIC collaboration (2014, 2017) and at the European Linear Collider workshops (2013, 2016). The results of the 2014 test beam presented here in Chapter 4 were published in EPJ-C (C78 (2018) no.2, 135). and were presented by me at the Israel Physical Society meeting and at the 2017 European High Energy Physics Conference in Venice. The results of the 2016 beam-test presented here in Chapter 5 were already accepted for publication in EPJ-C with minor comments and the publication is imminent.

Contents

CHAPTER 1

Introduction

The 2013 Nobel prize in physics [1] honored Francois Englert and Peter W. Higgs for the theoretical proposal of a mechanism that contributes to our understanding of the origin of subatomic particles masses [2–5]. Awarding the prize to Englert & Higgs marked the recent big achievement for experimental particle physics, the discovery of the Higgs boson. In July 2012, the ATLAS and CMS experiments at the CERN Large Hadron Collider (LHC) announced the long-awaited discovery of a new "Higgs-like particle" with a mass of 125 GeV with many properties as foreseen in the standard model (SM) [6, 7].

The Higgs discovery was the last and final prediction of the SM of particle physics that describes the strong, weak, and electromagnetic interactions. The strength of the SM arises, among other qualities, from its gauge invariance, which allows stringent tests of its predictions. During the last 50 years, the validity of the SM was confirmed in various processes and at various accelerators, and so far the SM passed every test with brilliant colors.

However the SM is far from being the ultimate theory of nature. First, the SM provides no understanding of the origin of the spontaneous symmetry breaking (through the Higgs field). It neither provides a mechanism for the phenomenon nor predicts the mass scale at which it occurs. Second, the SM does not provide a particle to describe the dark matter and dark energy that make up 95% of the total matter in the universe. Third, the SM does not provide a mechanism to generate the baryon-antibaryon asymmetry of the universe.

No interaction in the SM can answer these important open questions in physics. In order to extend our understanding towards answering these questions, new fields and new interactions are required. According to quantum field theory, new particles will emerge as a sign of such new interactions. The search for these new particles is a high priority goal of the experiments at the LHC. Taking advantage of the high energy and large reaction rates possible in proton-proton collisions, the LHC experiments have searched for a wide variety of new particles predicted by theories that extend the SM to beyond the SM (BSM). So far, at the end of the LHC run II, these searches came out empty.

There is still a great opportunity to discover such particles when the LHC resumes operation in 2021, possibly at center of mass energy of $\sqrt{s} = 14$ TeV during run III. Especially since during that run, each of the LHC large experiments is expected to accumulate about 300 fb^{-1} on top to the 150 fb^{-1} of data already collected. Furthermore, in the foreseeable future after the run III period, an ambitious project for luminosity upgrade, known as the high-luminosity LHC, HL-LHC, will start, and a 10 time increase in the amount of collected data is expected.

In any scenario, whether the LHC will or will not find new particles, additional tools are needed. Although the LHC offers obvious advantages for experimenters in providing very high energy and very high rates in typical QCD reactions, it lacks in other areas like high-precision measurements to probe electroweak processes. Such attributes can be found at lepton colliders. It has long been agreed [8] that an electron positron, e^+e^-, collider operating in the TeV scale is important in order to complete the high-precision probe in this energy range.

1.1 Lepton colliders advantages

A proton - proton collider, like the present LHC or its upgrades in the future, offers obvious advantages by providing high energy and high interactions rates, with the latter mainly driven by QCD with its inherent uncertainties. The advantages of lepton colliders are different in that they permit high-precision measurements to be performed.

The environment for e^+e^- collisions is much more benign than for hadron-hadron collisions. While at the LHC each bunch crossing leads to about 70 proton-proton collisions, and each of these produces hundreds of energetic particles, at lepton colliders, like the International Linear Collider (ILC), at each bunch crossing one expects about one photon-photon collision, with only a few hadrons in the final state. This difference in the environment has profound implications for the detectors design. In lepton colliders the detector can be much more compact and can be moved closer to the interaction point, while at the LHC, detectors are much bigger, built from denser, more radiation-hard materials. This difference leads to better momentum and jet energy resolution and excellent tagging capabilities of b and c quarks and of the τ lepton. In addition, the complications in analyzing LHC events, due to hadrons from the underlying-event flow and pileup from multiple collisions in each beam crossing, are essentially removed in e^+e^- events. The e^+e^- environment provides a setting in which the basic, known, high-energy collisions can be measured with high precision.

At the LHC, interesting events occur at rates of $10^{-7} - 10^{-13}$ of the total event rate. This forces the trigger system to exclude all events but 1 in 10^6 before any data analysis is possible. Furthermore, only events with unusual and striking properties can be recognized by the complex trigger system over the much larger sample of background QCD, and a new particle can be studied only if its signals is clearly discriminated. For e^+e^- experiments that are foreseen in the near future, the processes under study are large fractions of the total electron-positron annihilation cross section, so no trigger is needed, and all bunch crossings can be recorded and any needed event reduction can be performed offline. Since there is no trigger, no special selection is needed in classifying events. That is, all final states of a decaying particle can be used for physics analyses and therefore measurement of absolute branching ratios or total widths is possible. One of the most important advantages of a lepton collider is that it is easier to recognize W and Z heavy gauge bosons in their hadronic decay modes, since the hadronic background is low. This advantage is important for measurements of absolute branching ratios of heavy exotic particles, and also of the top quark and the Higgs boson whose decay products typically include the weak bosons.

At the LHC, cross section calculations are QCD based. Any theoretical calculation (signal or background) has systematic uncertainties from the parton distribution functions in the proton, from unknown higher order perturbative QCD corrections, and from nonperturbative QCD effects. For example, NLO QCD corrections to cross section calculations are typically estimated to be at the 30-50% level. At the e^+e^- colliders, the initial state consists of point-like elementary particles, coupling only to the electroweak interactions, and the first radiative corrections to cross sections are at the few-percent level. The high precision theoretical understanding of SM signal and background processes, make it possible to find elusive new physics interactions, and to characterize these interactions fully.

1.2 Physics potential of e^+e^- colliders

The Physics potential of a high energy e^+e^- collider is broad, and includes topics like properties of the Higgs boson, top quark measurements, precision measurements of the SM, super symmetry, and the quest for new BSM particles. In the last few years, the topic of precision measurements of the newly discovered Higgs boson properties and interactions, became much more important. Highlighting these priorities is the fact that the Higgs boson is the only discovery at the LHC up to now. Since new effects are the key to finding new physics, today, precision studies of the Higgs boson properties and interactions are among the most promising paths to open a window to physics beyond the SM. For that reason, special emphasis is placed on the Higgs boson measurements program of future e^+e^- colliders under the title of "Higgs factory".

Comprehensive reviews of TeV scale physics, and in particular for the physics case of a high energy e^+e^- linear collider, is beyond the scope of this thesis which concentrates on detector development to address the challenges of precision measurements. A recent comprehensive summary can be found in reviews like [9, 10] or dedicated reports like [11, 12]. Here only a taste of the basic important measurements in e^+e^- colliders is presented briefly.

Unlike in the LHC where gluon fusion provides by far the maximum rate for intermediate Higgs masses, in e^+e^- the main production processes is "Higgsstrahlung", or $e^+e^- \longrightarrow ZH$, that dominates at lower $\sqrt{s}$. The two other major Higgs production processes are $e^+e^- \longrightarrow \nu_e\overline{\nu}_eH$, "$W$ fusion", and $e^+e^- \longrightarrow e^+e^-H$, "$Z$ fusion", that rise with $\sqrt{s}$. The three relevant Feynman diagrams are presented in Fig. 1.1

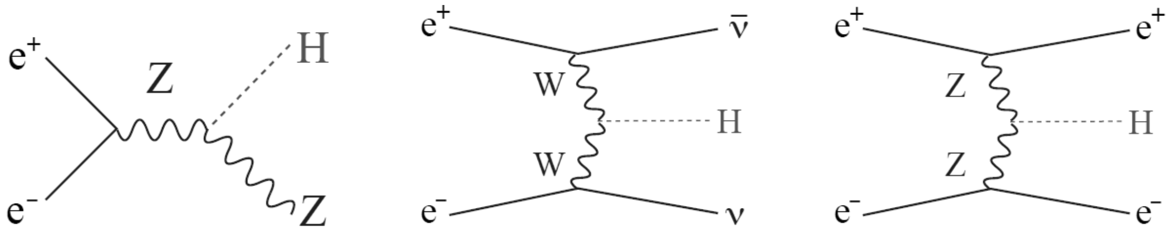

Figure 1.1: Feynman diagrams for the three major Higgs production processes at the ILC, $e^+e^- \longrightarrow ZH$, "Higgsstrahlung", on the left, $e^+e^- \longrightarrow \nu_e\overline{\nu}_eH$, "$W$ fusion" in the middle, and $e^+e^- \longrightarrow e^+e^-H$, "$Z$ fusion", at the right.

As can be seen in Fig. 1.2, where the Higgs production cross section is shown as a function of $\sqrt{s}$, "Higgsstrahlung" dominates at lower energies and peaks around 250 GeV. This process offers a unique opportunity for the studies of the Higgs boson, and is at the base of any Higgs measurement program in e^+e^- colliders. With the "Higgsstrahlung" it is possible to identify the Higgs without reconstructing its decay products. It is enough to identify the Z boson in the laboratory frame with energy corresponding to the recoil against the 125 GeV Higgs boson. It allows to observe all Higgs decays, into visible and invisible states, and measure the cross section σ_{ZH}. Investigation of the invisible decay modes of the Higgs can identify exotic decays into dark matter particles, or into other long-lived particles that do not couple to the SM interactions.

In addition, measurements of the decay of the Z to e^+e^- or $\mu^+\mu^-$ gives a very precise determination

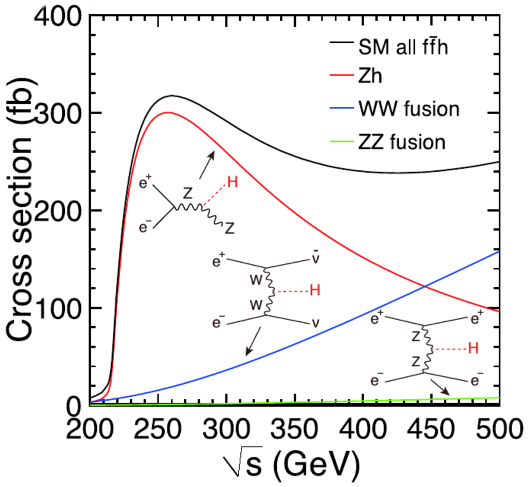

Figure 1.2: Cross sections for the three major Higgs production processes as a function of $\sqrt{s}$ at the ILC with the left-handed polarization combinations: $P(e^-, e^+) = (-0.8, +0.3)$

of the mass of the Higgs boson. The mass of a particle recoiling against a lepton pair is given by

$$M_H{}^2 = (P_{CM} - (P_{l^+} + P_{l^-}))^2 \tag{1.1}$$

where P_{CM} is the 4-momentum of the annihilating lepton-antilepton system. Combining the e^+e^- and $\mu^+\mu^-$ channels allows to determine the Higgs mass to better than 30 MeV and the cross section to a sub-% level. These levels are better than the current precision in the LHC of 160 MeV, and similar to the expected levels of the full run of the HL-LHC [13]. The precision of determining the cross section can be further improved by adding events with decay of the Z to quarks.

The $e^+e^- \longrightarrow ZH$ process will also be used to measure various Higgs branching ratios. In order to extract couplings from branching ratios, the total width is needed, since the coupling of the Higgs boson to a particle A, g_{HAA} squared is proportional to the partial width which is given by the total width times the branching ratio:

$$g^2_{HAA} \propto \Gamma(H \longrightarrow AA) = \Gamma_H BR(H \longrightarrow AA) \tag{1.2}$$

When using Eq. (1.2) the Z boson as A, with the additional information of σ_{ZH} from the recoil mass measurement, the Higgs total width Γ_H can be determined. The Higgs total width is used to extract the coupling of other particles from their branching ratios. In the SM, a linear relation is expected between the Higgs coupling to a particle and the particle mass. As can be seen in Fig. 1.3, from simulation results for the expected full program of the ILC and for the expected precision achievable with the ATLAS detector at the HL-LHC, the coupling resolution is better for the e^+e^- collider, including the addition of the coupling of the Higgs boson to c that is very hard to measure at a proton-proton collider.

At higher energies the Higgs boson self-coupling forms a central part of the Higgs physics program at a high energy linear collider. The trilinear Higgs self-coupling can be measured through the $e^+e^- \longrightarrow ZHH$ and $e^+e^- \longrightarrow HH\nu_e\overline{\nu}_e$ processes. At $\sqrt{s} = 500$ GeV the $e^+e^- \longrightarrow ZHH$ process

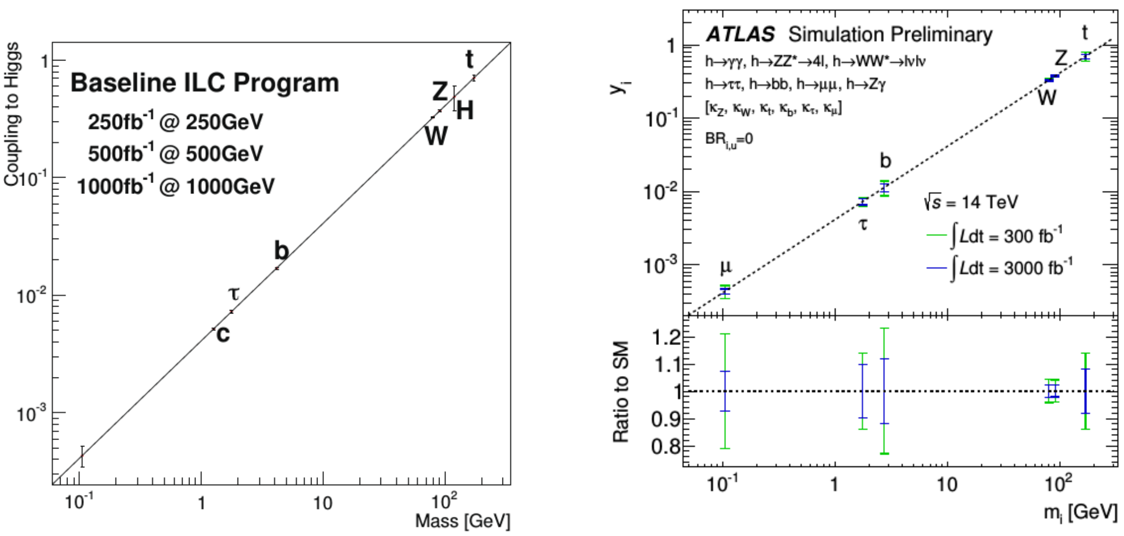

(a) **(b)**

Figure 1.3: Expected mass-coupling relation for the SM Higgs after (a) the completion of the full ILC program, and for (b) the ATLAS experiment with integrated luminosity of 300 fb^{-1} or 3000 fb^{-1} at 14 TeV.

dominates, but a very large integrated luminosity is required to measure the Higgs self-coupling [11]. The sensitivity for the process $e^+e^- \longrightarrow HH\nu_e\overline{\nu}_e$ increases with $\sqrt{s} > 1$ TeV and it can be used to preform the Higgs boson self-coupling measurement that determines the shape of the fundamental Higgs potential [14].

1.3 Future colliders

As a result of the Higgs boson discovery, and the first measurement of its mass, the European Particle Physics Strategy Update (EPPSU) in 2013 [15], unambiguously recognised the importance of an e^+e^- collider that can study the properties of the Higgs boson and other particles with unprecedented precision and whose energy can be upgraded. This statement further strengthens the case of future linear e^+e^- colliders, that were already under development during this period like the ILC, and the Compact Linear Collider, CLIC.

This statement, and the relative low mass of the Higgs boson, invoke a discussion on other projects that can meet the EPPSU recommendation. The primary idea is an e^+e^- circular colliders associated with a post-LHC hadron circular collider. In this context two projects are being developed these days. The first is the CERN-based Future Circular Collider, FCC, with its e^+e^- option, FCC-ee [16–18]. The second one is the Circular Electron Positron Collider, CEPC, proposed by the Chinese High Energy community in 2012 [19, 20].

One of the main limitation of a circular e^+e^- colliders is synchrotron radiation that depends on the colliding particle mass. This limitation prevented the Large Electron Positron (LEP) at CERN from achieving energies necessary to produce a Higgs boson, while it was on the verge of the discovery 20 years ago. The design of the ILC and CLIC as linear colliders overcomes this limitation. In addition, they provide the option to increase the collider energy over time, by adding more accelerating units and extending the collider's total length. Another advantage of the design is the increase in luminosity with increasing energy. The draw back of this design is the requirement that the acceleration gradient must be high for a finite length accelerator.

The design of FCC-ee and CEPC takes advantage of the the superiority in luminosity that can be reached with circular colliders to create a "Higgs factory". The design relies on technology improvements from LEP's times and the higher energy is achieved by increasing the circumference to about 100 km, to allow an upgrade in $\sqrt{s}$ up to 400 GeV e^+e^-, well above LEP's 209 GeV and above the pair production threshold of the top quark. A comparison between the $\sqrt{s}$ and luminosities for the different future lepton colliders, linear and circular, is presented in Fig. 1.4. It demonstrates the superior luminosity of the circular colliders at lower $\sqrt{s}$, used for electroweak precision measurements. But it also demonstrates similar luminosity performance of the two accelerator types in the mid energy range used for the Higgs measurements. The linear colliders extend their coverage to much higher energies and higher luminosities for an extended Higgs program and open the possibility for discovering new physics at energies which are inaccessible by circular colliders.

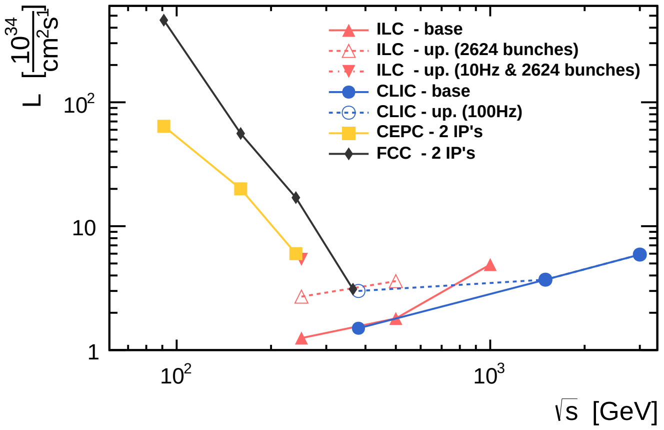

Figure 1.4: Comparison between the planned energies and luminosities for the different future e^+e^- colliders, as presented in the summary talk by L. Rivkin on the Accelerator Science and Tehcnology during the 2019 Granada Open Symposium on the European Particle Physics Strategy Update.

1.3.1 Circular colliders

With the current technologies, a very large circular hadron collider appears to be the only feasible approach to reach $\sqrt{s} = 100$ TeV in the coming decades. It is only reasonable that such a proton-proton machine will become the new energy frontier after the LHC will finish its full program. As in the case of LEP and its successor, the LHC, it makes sense to plan a new infrastructure that could hold a future circular e^+e^- collider followed by a proton-proton collider. Two such projects are presently under development.

1.3.1.1 FCC-ee

European studies of post-LHC circular energy-frontier accelerators at CERN had already started during the start of the LHC run I, in 2010–2013, for both hadron [21] and lepton colliders [22], separately, at the time called HE-LHC/VHE-LHC and LEP3/DLEP/TLEP, respectively. In accordance with the EPPSU 2013 statement, the FCC study was launched [23] as a staged project that aims to start with a high luminosity, high precision lepton circular collider, named FCC-ee, and continue to a high energy hadron collider named FCC-hh, where an intermediate stage of an electron-proton (FCC-eh) option is also under study.

During 2018, as the first steps towards the upcoming European strategy update to be approved during mid 2020 were under way [24], the FCC studies were summarized in a four-volume Conceptual Design Report, CDR [16–18, 25].

The FCC-ee is designed to deliver the highest rates in a clean, well-defined, and precisely determined environment, at the Z pole ($\sqrt{s} = 91$ GeV), at the WW threshold ($\sqrt{s} = 161$ GeV), as a Higgs factory ($\sqrt{s} = 240$ GeV), and around the $t\bar{t}$ threshold ($\sqrt{s} = 340$ to 365 GeV), at two interaction points. It is also designed to provide high precision calibration of the beam energy, at 100 keV level, at the $Z-$ mass and at the WW threshold, a unique feature of circular colliders. For a $\sqrt{s} = 365$ GeV, as required for the $t\bar{t}$ threshold operation, the cost-optimised circumference is about 100 km.

The FCC-ee is designed as a double ring collider, to allow a large number of bunches. The two beam lines cross at two interaction points (IPs) with a horizontal crossing angle of 30 mrad. The large crossing angle is important to keep the background from synchrotron radiation and various other beam-beam effects under control, but at the same time it reduces the instantaneous luminosity, since the bunches do not collide head on. To compensate for the luminosity loss, a crab waist collision scheme [26] will be implemented. The latter consists of squeezing and shaping the transverse beam profiles at the IP for maximum bunch overlap under large crossing angles. This scheme will boost the luminosity by more than four orders of magnitude compared to previous colliders like the LEP at the Z pole. This novel collision scheme has been successfully used at DAΦNE since 2008 [27]. The beam current varies greatly between the Z pole and the $t\bar{t}$ threshold. The current is adjusted primarily by changing the number of bunches to keep synchrotron radiation at an acceptable level for all energies. With such a device, precision electroweak physics, precision Higgs physics, and measurements of the top quark and W boson properties will reach orders of magnitude improvements.

Figure 1.5 presents the FCC-ee proposed layout where the two experiments are situated in points A and G. A zoom of the IP and the crossing angle can be seen in the inset of the figure. This collider is to be implemented in stages.

1.3.1.2 CEPC

The Chinese particle physics community initiated in 2012 a study of a large circular collider project that would be hosted in China. The project suggested to construct a 100 km long circular e^+e^- collider, the CEPC. The CEPC design shares many of the design aspects and views of the European FCC-ee. The tunnel for such a machine will be built in a way that it could host at the same time also a Super Proton Proton Collider (SPPC) to reach energies beyond the LHC, that will be built at a later stage.

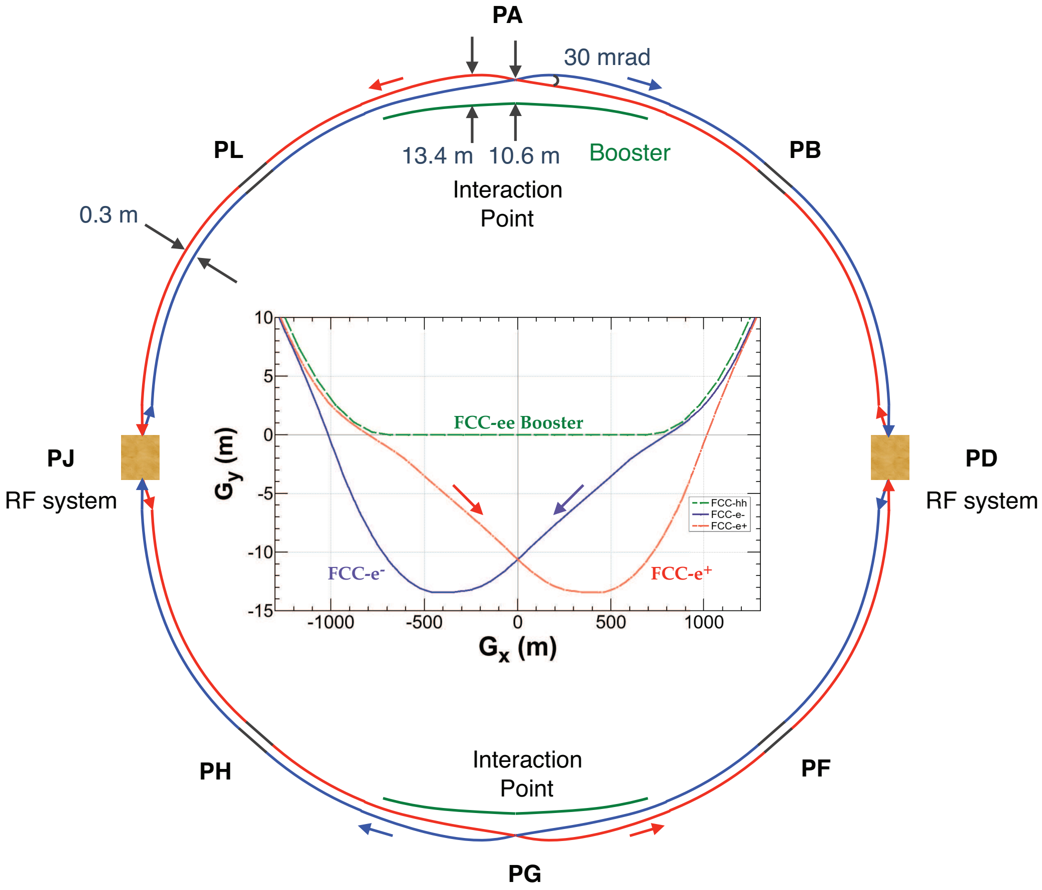

Figure 1.5: Overall layout of the FCC-ee with a zoomed view of the trajectories at the interaction point G.

The CEPC is designed to operate at around $\sqrt{s} = 91.2$ GeV as a Z factory, at around $\sqrt{s} = 160$ GeV of the WW production threshold, and at $\sqrt{s} = 240$ GeV as a Higgs factory. It will produce large samples of Z, W and Higgs bosons to allow precision measurements of their properties. The CEPC plans to keep the amount of synchrotron radiation constant (30 MW) using three operational modes with different bunch spacing (25 ns, 210 ns, and 680 ns respectively) to control the total beam current.

During 2018 the project released a two-volume CDR, describing the design of the CEPC accelerator complex [19] and the physics potential with possible detector concepts [20]. The CEPC construction is expected to start in 2022 and would be completed in 2030. Prior to the construction, there will be a five-year R&D period (2018–2022). During this period, two international collaborations will be formed to produce a Technical Design Report, TDR.

1.3.2 Linear colliders

The Linear Collider Collaboration is an organization established by the International Committee for Future Accelerators, ICFA, to coordinate the global R&D efforts on the two candidates for the role of the next high energy linear collider, the ILC and CLIC.

1.3.2.1 ILC

The studies for the ILC project are the longest ongoing among the projects presented here, and, likely, technologically the most mature. Over the past decades, studies in Asia, Europe and North America have built the scientific case for a baseline future e^+e^- linear collider. From 2005 to the publication of the TDR [28] in 2013, the design of the ILC accelerator was conducted under the mandate of ICFA as an international collaboration under the name of the Global Design Effort. Since 2013, as noted above, ICFA has placed the international activities together with the CLIC project, under the Linear Collider Collaboration (LCC). The ILC TDR describes in four volumes the physics case and a mature, ready for construction, technical design of a $\sqrt{s}$ = 500 GeV linear e^+e^- collider, that can be extended up to an energy of $\sqrt{s}$ = 1 TeV. In addition, the electron beam will be polarised to 80 %, and the baseline plan includes an positron source which will deliver 30% positron polarization. A schematic layout of the ILC with 500 GeV from the TDR is presented in Fig. 1.6, were the electron and positron paths are highlighted, and all of the major subsystems are included.

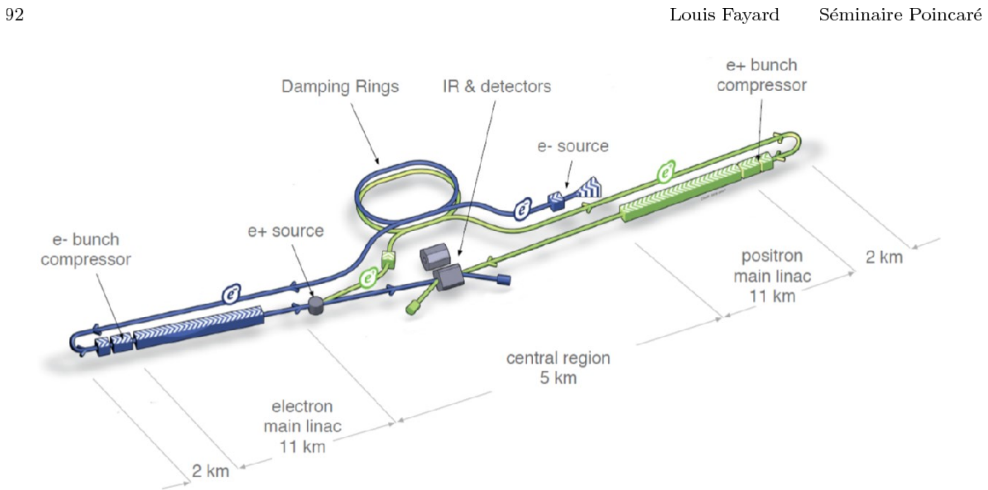

Figure 1.6: Schematic layout of the ILC, indicating all of the major subsystems (not all to scale).

The Japanese government expressed an interest to host the ILC in Japan. To this end, the TDR design is being converted into a site-specific one located in the Kitakami highland in the Iwate prefecture in northern Japan. Up to this day the linear collider community is waiting for a clear decision from the Japanese government regarding the future of the ILC in Japan.

The ILC design is based on superconducting radio-frequency (SCRF) acceleration technology, using 1.3 GHz niobium cavities as the accelerating structures. The European XFEL [29] provides presently an operating 1/10-scale demonstration of the fundamentals of the SCRF technology, and the successful manufacture of the accelerating structures.

Once the mass of the Higgs boson was measured, it was established that the linear collider should start its ambitious physics program with an initial $\sqrt{s}$ = 250 GeV, operating as a “Higgs factory” [30], with a reduced cost relative to that quoted in the TDR. Advances in the theoretical understanding of the impact of precision measurements at the 250 GeV ILC indicate that this operating point already gives substantial sensitivity to physics beyond the SM.

This staged version of the ILC would have two main linac tunnels, about half the length of the 500 GeV TDR design (6 km instead of 11 km). Other systems, in particular the beam-delivery system and the main dumps, would retain the dimensions of the TDR design. Then the 250 GeV ILC could be upgraded to energies of 500 GeV or even 1 TeV with a reasonable effort, without extensive modifications to the central region. Another upgrade option, which could come before or after an energy upgrade, is a luminosity upgrade. The doubling of the luminosity can be achieved by doubling the number of bunches per pulse to 2625 at a reduced bunch separation of 366 ns, or by an increase of the pulse repetition rate from 5 to 10 Hz at 250 GeV; these options were presented at Fig. 1.4.

1.3.2.2 CLIC

The Compact Linear Collider (CLIC) is a multi-TeV high-luminosity linear e^+e^- collider under development by the CLIC accelerator collaboration [31]. It is the only mature proposal for a multi-TeV lepton collider. The CLIC CDR was published in 2012 [32–34]. The main focus of the CDR was to demonstrate the feasibility of the CLIC accelerator at 3 TeV and to confirm that high-precision physics measurements can be performed in the presence of particles from beam-induced background. The CDR presented an accelerator complex optimised for 3 TeV with two initial lower-energy stages, at 500 GeV and 1.4/1.5 TeV, which were not technically optimised at this point. The CDR was finalised just before the discovery of the Higgs boson, hence, the Higgs mass was not fully taken into account in the choice of the CLIC energy staging. Detailed studies of Higgs and top-quark physics set the first stage with the working point to be at $\sqrt{s} = 380$ GeV. The results of a comprehensive optimization study, following the completion of the CDR, led to optimised accelerator design parameters for the proposed staging scenario, with operation at 380 GeV, 1.5 TeV and 3 TeV [35].

The ongoing CLIC development studies provide a project implementation plan for CLIC construction. The CLIC collaboration plans to go ahead with a preparation phase after 2020, where all parameters, systems and experiments will be finalised with an expected TDR during 2025, and the start of construction some time after that. The CLIC project is waiting for the decision on the next CERN project at the energy frontier, expected in the upcoming EPPSU [24]. An implementation plan for the three CLIC stages and the main linac footprint at CERN is shown in Fig. 1.7.

The CLIC accelerating mechanism is based on the novel two-beam accelerator scheme. The 12 GHz RF power is extracted from a low-energy, high-current drive beam, which is decelerated in power-extraction and transfer structures of low impedance. This power is then directly transferred into the high-impedance structures of the main linac and used to accelerate the high-energy, low-current main beam. The two-beam approach to acceleration offers a solution that avoids the use of a large number of active RF elements in the main linac. In order to limit the overall extension, the scheme is based on average accelerating-gradient of 100 MV/m which results in a total length of 48 km for the 3 TeV stage. For the first energy stage, a lower gradient of 72 MV/m is the optimum to achieve the luminosity goal, which requires a larger beam current than at higher energies. CLIC aims to provide also ±80% longitudinal electron polarization and proposes a sharing between the two polarization states at each energy stage. The CLIC beam consists of bunch trains 156 ns long in a 50 Hz repetition rate. Within a bunch train, the 312 bunches are separated by 0.5 ns. Similar to the ILC, the CLIC project came up with a luminosity upgrade option for the first stage by doubling the repetition rate.

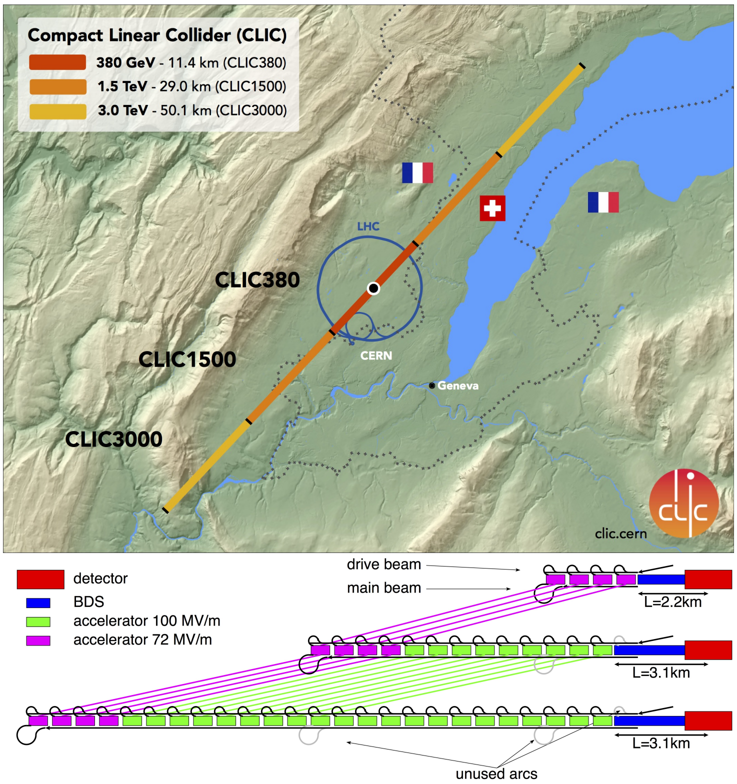

Figure 1.7: The CLIC main linac footprint near CERN, showing the three implementation stages. The latter also appear at the bottom of the figure.

These options were presented in Fig. 1.4. The challenging timing structure and the significant beam related backgrounds of CLIC, set tough requirements for the CLIC detector.

1.4 Detector concepts

The physics program of the future e^+e^- collider places stringent requirements on the detector performance. These include precise momentum resolution, vertex reconstruction, particle identification, excellent jet reconstruction and hermetic coverage. To allow, especially at the linear colliders, for flexibility in the beam energy and possible staging of the accelerator, these requirements have to be met over a range of $\sqrt{s}$. Since all detectors, whether for linear or circular colliders, have to meet these requirements, their conceptual designs are similar. For the circular colliders, at least two detectors are expected to run simultaneously. At the ILC, also two detectors are planned but they will have to share the beam time (push/pull option), while in CLIC only one detector is foreseen. The R&D of the ILC and CLIC detectors is ongoing from the start of the projects. Now, the detector concepts are mature, after a long and thorough optimization process. The detectors concepts for the circular colliders were adopted from the linear colliders detectors that will be discussed here.

For the ILC, two general purpose detector concepts have been developed over the last decade, the International Large Detector (ILD) [36] and the Silicon Detector (SiD) [37]. Both of these concepts were evaluated and validated. For CLIC, two detector models were previously defined based on concepts for the ILC detectors and adapted for the higher $\sqrt{s}$ at CLIC, and were used in the CDR [33]. Based on the lessons learnt during these years, as well as the experience from several additional optimization studies, a new single detector model, CLICdet, was introduced [38]. The overview of the ILD for the ILC, and CLICdet for CLIC, can be seen in Fig. 1.8.

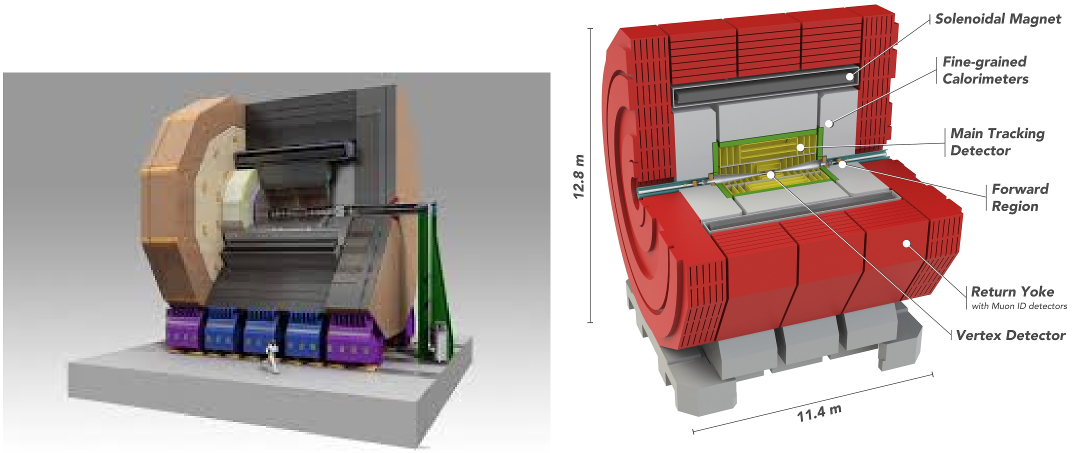

(a) **(b)**

Figure 1.8: General overview of the detectors for (a) ILC (ILD) and (b) CLIC colliders.

Following the physics requirements, it is not surprising that the main building blocks of the two designs are very similar. Both are cylindrical detectors with tracking and calorimetry inside a solenoid. The two of them share the following main design principles:

- very efficient tracking detectors with excellent momentum reconstruction in a high field solenoid;
- secondary vertex reconstruction with a powerful pixel detector as close as possible to the beam-pipe;
- low material budgets in the tracking devices;
- highly segmented electromagnetic and hadronic calorimeters inside the solenoid;
- Particle Flow Algorithms (PFA) [39] for optimal jet reconstruction define the layout of the detector, in particular for the calorimeters;
- hermeticity of the detector, crucial for an excellent determination of missing energy which is an important signature for new physics processes;
- instrumented return yoke for muon identification.

However, particular choices and the overall approach are quite different. The ILD tries to optimize jet reconstruction with calorimetry at large radii to separate the outgoing particles as much as possible at the cost of a lower magnetic field, and with a precision tracking system based on Time Projection Chamber (TPC) which provides up to 200 precise track measurements. The consequence is an overall radial size like the CMS detector at the LHC. On the other hand, the SiD design is as compact as possible to provide a cost-optimized detector, resulting in a high magnetic field within a solenoid of minimal radius and with precision all-silicon tracking.

A comparison of detector concept parameters for both ILC and CLIC is presented in Table 1.1.

Table 1.1: Comparison of detector concepts for ILC (ILD and SiD) and CLIC (CLICdet) parameters.

Concept	ILD	SiD	CLICdet
Tracker	TPC/Silicon	Silicon	Silicon
Solenoid Field (T)	3.5	5	4
Solenoid bore radius (m)	3.3	2.6	3.5
Solenoid Length (m)	8.0	6.0	8.3
VTX Inner Radius (mm)	16	14	31
ECAL r_{min} (m)	1.8	1.3	1.5
ECAL Δr (mm)	172	135	202
HCAL Absorber	Fe	Fe	Fe
HCAL interaction lengths	5.5	4.8	7.5
Overall Height (m)	14.0	12.0	12.9
Overall Length (m)	13.2	11.2	11.4

1.5 Scope of the thesis

To match the physics potential of a high energy e^+e^- linear collider, an R&D program is ongoing to continue develop the technologies for detectors for precision measurements. The precision is influenced by the knowledge of the beam energy, the absolute luminosity and the beamstrahlung and more, which affects the average beam energy as well as the effective beam energy spread. In particular, the luminosity measurement should achieve a precision of 10^{-4} to match the required precision on the Higgs couplings at the ILC, and 10^{-3} at CLIC.

The subject of this study is the luminosity measurement at a future e^+e^- linear collider and the R&D of the luminosity calorimeter, LumiCal, towards a proof of concept of a more realistic luminosity measurement. In Chapter 2, the planned concept of the luminosity measurement at a future e^+e^- collider will be reviewed, and the forward region design of a future detector, including the luminosity calorimeter, will be described.

The LumiCal calorimeter is based on silicon sensors and tungsten absorbers layers. Before the silicon sensors can be used in a detector, they need to undergo a careful inspection and qualifications. For this purpose the TAU high energy experimental group developed a laboratory for the characterization and measurements of the silicon sensors. Nowadays, a silicon sensors prototype exists only for the ILC designed LumiCal and it is the subject of studies presented here. Since the LumiCal designed for CLIC is based on the ILC design and differs only in the pads size (about twice the size of the ILC ones), the studies presented here validate also the CLIC sensor design. The silicon sensors prototype currently in use in the FCAL collaboration, the silicon laboratory upgrade and the sensors characterization measurements will be presented in Chapter 3.

A major step in the detector prototype development is to prepare and conduct a test beam study of a multi-plane structure. The objectives of such a test is to demonstrate that a highly compact and efficient electromagnetic shower reconstruction in a prototype calorimeter can be achieved as required for a high precision luminosity measurement. The first test was performed in October 2014, at CERN. In Chapter 4, the test beam instrumentation will be described, the analysis of the raw data will be explained and the results will be presented.

In order to meet the LumiCal design, and improve the results obtained in the first test beam, a new thin LumiCal sensor module was designed. The new sensor module was tested and used for an improved detector prototype in a test beam in 2016 at DESY. The new module and the 2016 test beam with its results are the subjects of Chapter 5.

CHAPTER 2

The very forward region

Forward calorimeters at future e^+e^- collider detectors are indispensable to measure precisely the luminosity, a key quantity needed to convert counting experiments into cross sections. The gauge process is the low angle Bhabha scattering, which can be calculated with high precision in quantum electrodynamics. Since Bhabha scattering has a very steep dependence on the polar angle, an excellent angular resolution is required for its measurement, which poses a challenge to the mechanical precision of the device and its granularity.

2.1 Luminosity in e^+e^- colliders

In an e^+e^- collider, the integrated luminosity, $\mathcal{L}_{int}$, is determined by using Bhabha scattering events. The advantage of Bhabha scattering as a gauge process is that the event rate exceeds by far the rates of other physical processes. In addition, Bhabha scattering is a well-known and theoretically-controlled process. By counting the number of small-angle Bhabha events, N_B, and comparing it to the expected cross section, σ_B, $\mathcal{L}_{int}$ can by calculated from the ratio

$$\mathcal{L}_{int} = \frac{N_B}{\sigma_B} \, . \tag{2.1}$$

The luminosity measurement limit, in this method, is determined by the expected uncertainty on the theoretical cross section. At the end of LEP runs it was at a level of 5.4×10^{-4} [40]. Recently, progress in the calculation of higher orders claims to reach a precision level of 3.8×10^{-4} [41], on the way to a goal of 1×10^{-4}.

Bhabha scattering is the elastic scattering process of an electron and a positron ($e^+e^- \rightarrow e^+e^-$). In practice, the process is always accompanied by the emission of electromagnetic radiation ($e^+e^- \rightarrow e^+e^-(\gamma)$). The Bhabha scattering includes at the Born level γ and Z exchanges, both in the s- and the t-channel, as presented in Fig. 2.1.

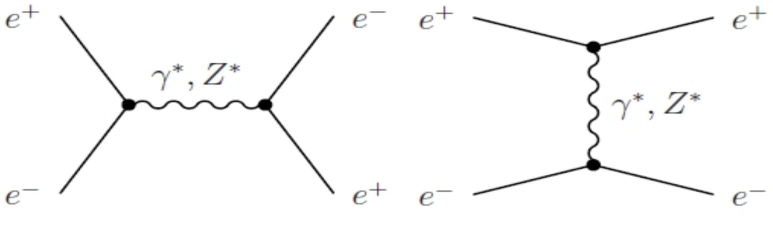

(a) s-channel **(b)** t-channel

Figure 2.1: Feynman diagrams of the (a) s- and (b) t-channel Born-level elastic Bhabha scattering.

The Bhabha scattering process may be written in terms of ten contributions, where four terms correspond to pure γ and Z exchanges in the s- and the t-channels, and the other six correspond to

$\gamma - Z$ and $s - t$ interference [42]. Taking into account the purely electromagnetic part with only the γ exchange, the Bhabha cross-section may be presented as the sum of three terms,

$$\frac{d\sigma_{\mathrm{B}}}{d\Omega} = \frac{\alpha^2}{2s}\left[\frac{1+\cos^4(\theta/2)}{\sin^4(\theta/2)} - 2\,\frac{\cos^4(\theta/2)}{\sin^2(\theta/2)} + \frac{1+\cos^2\theta}{2}\right], \tag{2.2}$$

where the scattering angle, θ, is the angle of the scattered lepton with respect to the beam, and α is the fine structure constant. The first and last terms correspond to γ exchange in the t- and s-channels, respectively, and the middle term reflects the $s - t$ interference.

For small angles ($\theta \leq 10°$), Bhabha scattering is dominated by the t-channel exchange of a photon. Neglecting the s-channel contributions, one can rewrite equation (2.2) in terms of the scattering angle as:

$$\frac{d\sigma_{\mathrm{B}}}{d\theta} = \frac{2\pi\alpha^2}{s}\frac{\sin\theta}{\sin^4(\theta/2)} \approx \frac{32\pi\alpha^2}{s}\frac{1}{\theta^3}. \tag{2.3}$$

As discussed above, it is planned for the ILC to deliver longitudinally polarized beams. For longitudinally polarized colliding beams, the purely electromagnetic part of the Bhabha cross-section in equation (2.2) changes to

$$\left(\frac{d\sigma_{\mathrm{B}}}{d\Omega}\right)_{Polarized} = \frac{d\sigma_{\mathrm{B}}}{d\Omega}\left(1 + P_{-}P_{+}A^{D}_{EM}\right)\ , \tag{2.4}$$

where $P_{-}(P_{+})$ is the electron (positron) beam polarization and A^{D}_{EM} is the double spin asymmetry. For beam energies of hundreds of GeV, the polarization of the beams changes the Bhabha integrated cross-section by a few percent [43]. Hence the polarization of the beams has to be taken into account in the measurement of luminosity.

In case of the ILC, and even more so at CLIC, the phenomenon of beamstrahlung plays an important role. The beamstrahlung process is the result of the interaction between the charged particles in a bunch with the field generated by the second bunch. At the planned high energies, beamstrahlung causes a significant energy loss and beam energy spread. In general, the collision parameters that lead to high expected luminosities, also lead to large smearing of the luminosity spectrum. This results in the need to measure the differential luminosity spectrum on top of the integrated luminosity.

The required accuracy of the luminosity measurement is derived from the physics program. At the ILC, the most rigid requirements come from the GigaZ program [44]. This program focuses on the measurement of fundamental parameters from the Z line shape. To fully exploit the GigaZ physics potential, the luminosity uncertainty must be below 2×10^{-4} [45]. Luminosity precision of better than 10^{-3} for the ILC and better than 10^{-2} for CLIC, is essential to study processes like $e^+e^- \longrightarrow W^+W^-$ or fermion production, $e^+e^- \longrightarrow f^+f^-$. The cross section of the W pair production is strongly peaked forward, and a precise luminosity measurement is needed to probe anomalies in the electroweak $e\nu W$ couplings. The process $e^+e^- \longrightarrow f^+f^-$ is sensitive to new physics at very high energy scales via interference with the SM amplitude. To detect deviations from the SM, precise cross section measurements are necessary. During the optimization and staging process ongoing presently in the CLIC project, the luminosity precision requirements are bound to increase.

To achieve a precise determination of the Bhabha event rates, a good position and energy resolution are needed. In future e^+e^- linear colliders, the luminosity measurement is performed through specially designed detectors in the forward region.

2.2 Layout of the forward region

The R&D and optimization of the very forward region and its instrumentation for the ILC and CLIC, are performed by the FCAL Collaboration [46]. Two specialized calorimeters are foreseen: LumiCal, for precise measurement of the luminosity and BeamCal, for a fast estimate of the luminosity and for the control of beam parameters. To support beam-tuning, an additional single layer silicon-pixel detector, referred to as pair-monitor, will be positioned just in front of BeamCal.

The design of the forward region is complicated by the small crossing angle of the two beams and thus the design of the forward detectors is somewhat different for the ILC and for CLIC, as summarized in Table 2.1. LumiCal and BeamCal are cylindrical electromagnetic calorimeters, centered around the outgoing beam. In the ILC, LumiCal is positioned inside and aligned with the forward electromagnetic calorimeter (ECAL endcap), while in the CLIC design, LumiCal is positioned just behind the ECAL endcap and some overlap exists for the larger polar angles in LumiCal. BeamCal is positioned just in front of the final focus quadrupole QD0. Both forward calorimeters will also improve the hermeticity of the main detector at very small polar angles. For example, in the ILC case, BeamCal covers polar angles between 5 and 40 mrad and LumiCal between 31 and 77 mrad. The main change in the forward region design for the ILC came from the change in the position of QD0. The distance from the interaction point, IP, to QD0, L^*, was changed in both ILD and SiD to 4.1 m to allow for simple exchange of detectors in the push-pull option. The reduction in space for the ILD (which expected $L^* = 4.4$ m) forced the move of BeamCal forward in place of the vacuum pump, which was then moved behind QD0. The LHCal in the ILC case stands between LumiCal and BeamCal and is meant to extend the coverage of the hadronic calorimeter (HCAL) in the end-cap to smaller polar angles. The forward region layout foreseen for CLIC and the ILC are shown in Fig. 2.2.

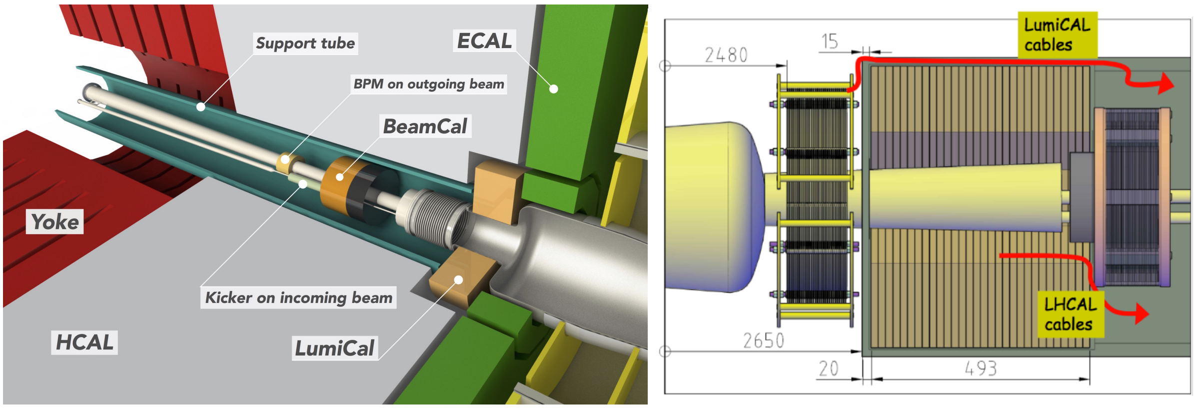

(a) (b)

Figure 2.2: Layout of the forward region design for (a) the CLICdet and (b) the ILD with $L^* = 4.1$ m where BeamCal is placed just after LHCal and the graphite shield is inside LHCal (units are in mm).

Table 2.1: Comparison of the LumiCal and BeamCal designs in the ILC (ILD) and in CLICdet.

		ILC(ILD)	CLICdet
LumiCal	geometrical acceptance [mrad]	31 - 77	39 - 134
	fiducial acceptance [mrad]	41 - 67	44 - 80
	z (start from IP) [mm]	2480	2539
	number of layers (W + Si)	30	40
BeamCal	geometrical acceptance [mrad]	5 - 40	10 - 46
	z (start from IP) [mm]	3200	3181
	number of layers (W + sensor)	30	40
	graphite layer thickness [mm]	100	100

2.2.1 BeamCal

The BeamCal calorimeter serves three major goals:

1. improving the detector hermeticity down to polar angles of a few mrad;
2. reducing the back-scattering from low-energy e^+e^- pairs into the inner detector parts as well as protecting the final magnet of the beam delivery system;
3. assisting in beam diagnostics by detailed analysis of the shape of the pair energy deposition.

BeamCal will be hit after each bunch crossing by a large number of beamstrahlung pairs. The total energy, up to several TeV per bunch crossing, and the shape of these deposits can be used for a bunch-by-bunch luminosity estimate and the determination of beam parameters [47]. However, deposits of single high energy electrons must be detected on top of the wider spread beamstrahlung. By using an appropriate subtraction of the pair deposits and a shower-finding algorithm which takes into account the longitudinal shower profile, the deposits of the high energy electron can be detected with high efficiency albeit with modest energy resolution.

For the ILC (CLIC), BeamCal base design consists of a 30 (40) layers sandwich-calorimeter with tungsten as absorber and a solid-state sensor, as illustrated in Fig. 2.3(a). BeamCal covers the polar angle range between 5 (10) and 40 (46) mrad. The tungsten absorber-disks will be one radiation-length thick and interspersed with thin sensor-layers equipped with front-end electronics positioned at the outer radius. In front of BeamCal, a 10 cm thick graphite block will be placed to absorb low energy back-scattered particles.

Due to the BeamCal location, the biggest challenge in its design is the development of radiation-hard sensors, that can withstand radiation doses of up to 1 MGy per year. As a possible solution, polycrystalline CVD diamond-sensors of 1 cm^2 size, and GaAs pad-sensors (with pad sizes varying from $4 \times 4\,\mathrm{mm}^2$ to $8 \times 8\,\mathrm{mm}^2$, produced by Tomsk State University) as shown in Fig. 2.3(b) were studied [48]. Since large area CVD diamond-sensors are still very expensive, they might be used only in the innermost part of BeamCal.At larger radii, GaAs-sensors seem to be a promising option.

Single crystal sapphires (Al_2O_3) are a new, very promising alternative of non-expensive radiation-hard sensors, for CVD diamond-sensors. Sapphire, is however, characterized by low charge collection efficiency, of ~ 5-10%, due to high level of impurities. A sapphire detector, designed to detect minimum ionizing particles (MIP) was tested in a beam test by the FCAL collaboration with promising

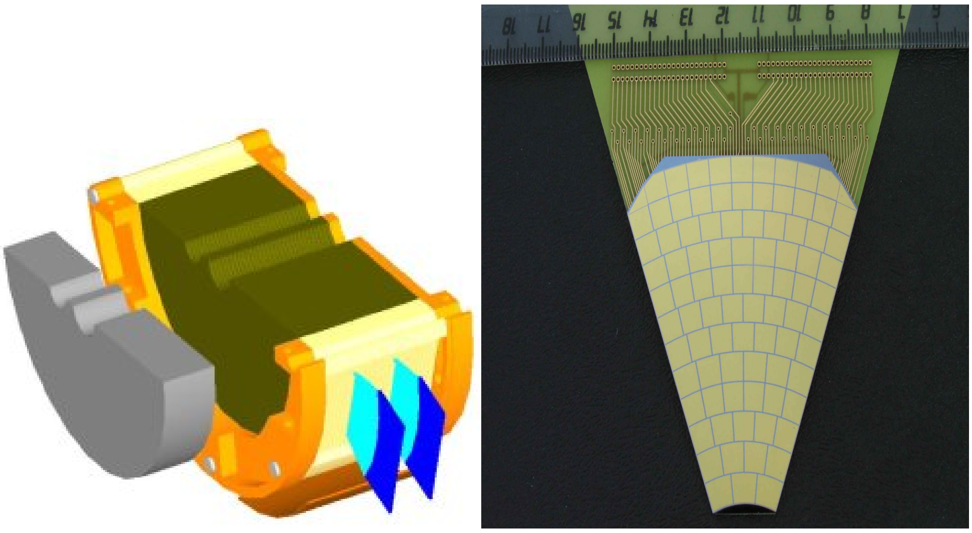
(a) (b)

Figure 2.3: (a) A half-cylinder of BeamCal for the ILC. The brown block is the tungsten absorber structure interspersed with sensor layers. The orange structure represents the mechanical frame. The blue segments at the outer radius indicate the front-end electronics. Shown in grey in front of the calorimeter is the graphite shield for absorbing back-scattered particles. (b) One of the GaAs-sensor prototype for BeamCal.

results that were published in [49]. Based on those results a new preliminary design for BeamCal was suggested [50]. It contained 12 tungsten absorber layers, 10 mm thick, with plates of sapphire sensors embedded inside. The proposed layer design is presented in Fig. 2.4(a), as well as the corresponding BeamCal layout in Fig. 2.4(b).

2.2.1.1 Pair Monitor

Additional and independent information on beam parameters will be obtained from the pair monitor. The pair monitor consists of one layer of silicon-pixel sensors, with pixel size of $400 \times 400\ \mu\text{m}^2$ just in front of the BeamCal, to measure the distribution of the number of beamstrahlung pairs.

In Fig. 2.5, the pair monitor located in front of the first layer of BeamCal can be seen. Monte Carlo simulation has shown that the pair monitor will give essential information for beam tuning. For example, after averaging over several bunch crossings, the beam sizes at the interaction point can be reconstructed with percent precision [51]. A special Application-Specific Integrated Circuit (ASIC), also shown in Fig. 2.5, is presently developed for the pair monitor. At a later stage, the pixel sensor and the ASIC will be embedded in the same wafer.

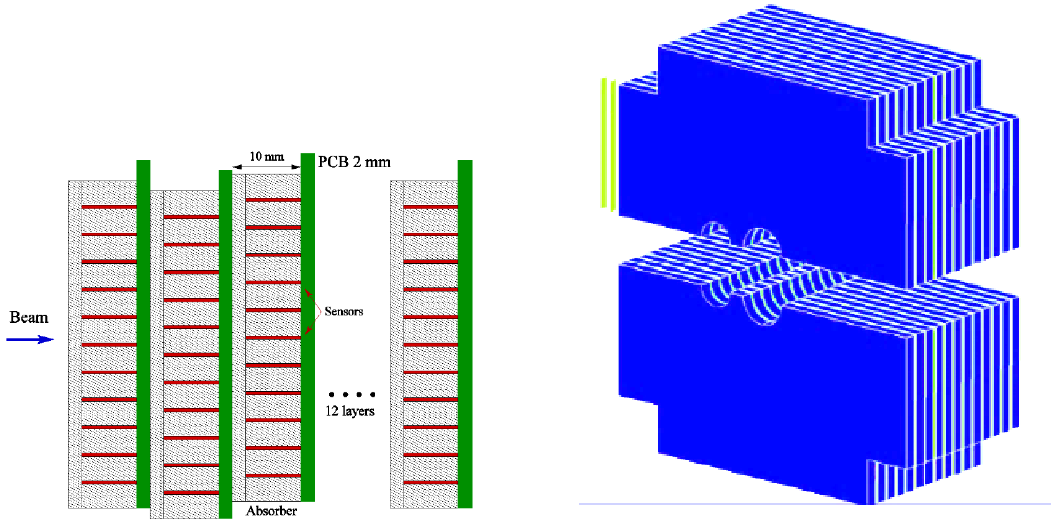

(a) **(b)**

Figure 2.4: The new ILC proposed (a) BeamCal sapphire layers structure, and (b) BeamCal full detector layout.

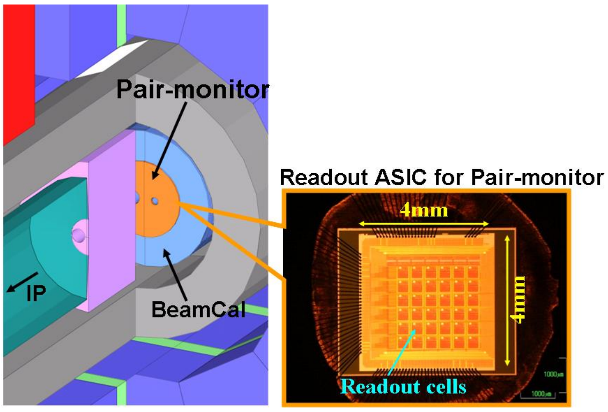

Figure 2.5: The pair monitor located at the first layer of BeamCal with its readout ASIC.

2.2.2 LumiCal

The LumiCal calorimeter also serves three major purposes:

1. measuring the rate of Bhabha scattering events at low angles for precise determination of the luminosity;
2. reducing beam-background by acting as a mask for the inner tracking detector;
3. improving the hermeticity of the main detector by providing electron and photon identification down to low polar angles.

The main challenge in the LumiCal design is to achieve the desired precision on luminosity determination with a precision of 10^{-3} at the ILC and CLIC in the Higgs factory mode.

Because of the steep θ dependence of the Bhaba cross section as seen in Eq. (2.3), the most critical quantity to control when counting Bhabha events is the inner acceptance radius of the calorimeter, defined as the lower cut in the polar angle, θ_{min} . Hence a very precise θ measurement is needed. Furthermore, the θ-range must be chosen such that the number of Bhabha events measured provides the required relative statistical uncertainty of less than 10^{-3} . The measurement of the polar angles is accompanied by a non zero bias in the polar angle, $\delta\theta$. Such a bias would cause a shift in the luminosity measurement if not corrected for, since events may migrate in and out of the fiducial volume.

Comprehensive simulation studies [48,52–54] for the ILD with the ILC beam conditions, showed that by choosing the lower bound of the polar angle between 40 and 60 mrad the statistical requirement can be easily reached. In addition, the studies showed that the bias and the resolution in the polar angle measurement depend on the polar angle pad size. For pad sizes less than 2 mrad the shift in the luminosity measurement is smaller than 10^{-3} thus guaranteeing a lesser uncertainty on the measurement.

A Bhabha event in LumiCal is identified as a pair of electron and positron, appearing in a back to back configuration in each of the two LumiCal arms, on the opposite sides of the interaction point. In order to separate the Bhabha scattering from any background process in LumiCal, the electron and positron energies should be similar and each of them should have at least 80% of the beam energy. In order to control the number of events above this threshold, the energy resolution should be well known and controlled to a level of 400 MeV. The energy resolution should also be constant across the fiducial volume, implying that the showers are well contained.

Monte Carlo studies have shown that a compact silicon-tungsten sandwich calorimeter is an adequate technology for LumiCal [53] . In the current design for ILC [48], as sketched in Fig. 2.6, LumiCal covers the polar angular range between 31 and 77 mrad (39 − 134 mrad for CLIC). The 30 (40) layers of tungsten absorbers (1 radiation length, X_0 thick) are interspersed with silicon sensor planes. The use of a compact silicon-tungsten calorimeter with small Moliére radius allows to spread the acceptance region or fiducial volume to most of the instrumented area. The LumiCal fiducial volume covers the polar angular range between 41 and 67 mrad. In this range the relative energy resolution is

$$\frac{\Delta E}{E} = \frac{0.21}{\sqrt{E(\text{ GeV})}}.$$

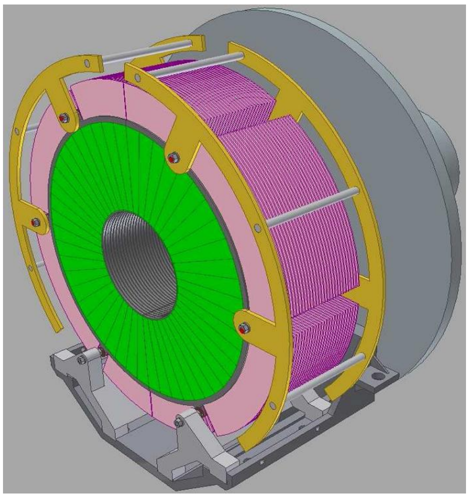

Figure 2.6: Mechanical structure of LumiCal.

For the ILC, as a compromise between the pad size and the number of readout channels, the baseline for the design was set to the polar angle pad size of 0.7 mrad, which corresponds to 64 radial divisions of the sensor. The azimuthal granularity was set to be 7.5° which correspond to 48 azimuthal sectors in each layer. For this segmentation the polar angle resolution and bias amount to $\sigma_\theta = 21.8 \pm 0.1\,\mu$rad and $\delta\theta = 3.2 \pm 0.1\,\mu$rad, respectively, which would induce a relative shift in the luminosity of $(\Delta L/L) = 1.6 \times 10^{-4}$, if no correction was applied.

The calorimeter is also sensitive to displacement and deformation of its mechanical structure coming from the calorimeter weight and temperature gradient. To match the requirements on the precision of the lower polar angle measurement, the sensor positions at the inner acceptance radius must be controlled to better than 40 μm. Other critical quantities are the distance between the two calorimeters and the position of the beam with respect to the calorimeter axis. The former must be known to about 1 mm and the latter to 500 μm. A laser based position monitoring system is envisaged to control the position of LumiCal over short distances with few micrometer precision.

To reduce the material budget the readout electronic is to be located on the outer radius of the calorimeters. One outcome of this design is a noncritical radiation dose exposure of the readout electronic. To cope with the expected occupancy in LumiCal, it must be read-out after each bunch crossing. Therefore special front-end and ADC ASICs have been developed which match the timing of the ILC-bunch trains with a frequency of 5 Hz and about 1 ms duration with 300 ns between bunches. The readout electronic is supposed to work in two modes, the physics mode and the calibration mode. In the physics mode, electromagnetic showers will be measured with large energy depositions on the pads up to at least 6 pC per channel. In the calibration mode, signals from single muons will be measured. The minimum size of these signals is 2 fC, corresponding to the low end of the Landau distribution in 300 μm thick silicon.

Silicon sensors for LumiCal in the ILC design, have been delivered by the Hamamatsu Corporation. The characterization and qualification of silicon sensors in test-bench and after instrumentation with front-end electronics in the beam-test was described in [55]. The assembly and performance of multi-layers LumiCal prototype in beam tests are the main subject of this thesis.

2.2.3 LHCal

At the ILC, LHCal is a supportive calorimeter in the forward region, which extends the coverage for hadrons to the LumiCal polar angle region, and provides hadronic hermeticity to the whole detector. The LHCal geometry is not final, since it was not studied as heavily as the other calorimeters in the forward region. The already packed layout of the forward region leaves just a small space for LHCal, and basically fixes the LHCal outer size. The LHCal fits in the square hole of the HCAL and surrounds the beam pipe which, in that region, is centred on the outgoing beam.

LHCal will probably be a silicon sensor sandwich-calorimeter similar to LumiCal, with either tungsten or steel for the absorber layers. It will consists of 2 half detectors containing 29 layers of 16 mm each, to a total thickness of 464 mm. Each absorber layer will be 630 mm wide, and 315 mm high with a cutout of a 150 mm radius around the beam pipe. The design of half of the LHCal detector, as presently considered in [56], is presented in Fig. 2.7

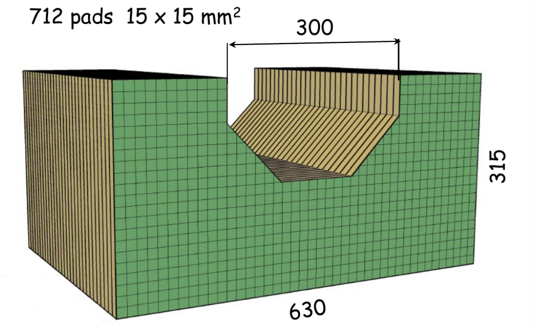

Figure 2.7: Bottom half of LHCal predicted design.

CHAPTER 3

LumiCal sensors qualification

The aim of this work is to present the first multi-layer LumiCal prototype beam tests and their results, described in the next chapters. As noted before, LumiCal is based on silicon sensors and tungsten absorber layers, and so are its prototypes. Before the silicon sensors can be used in a prototype, they need to undergo a careful inspection, qualifications and be mounted onto a sensor module assembly. For this purpose, the TAU high energy experimental group developed a laboratory for the characterization and measurements of the silicon sensors. In the following, the silicon sensor prototypes currently in use in the FCAL collaboration, their characterization measurements and the module assembly used for the beam tests, are described.

3.1 Silicon-sensor prototype

As a result of Monte Carlo optimization of sensor granularity [52, 54], at the ILC each of the 30 silicon layers will be subdivided into 48 sectors (7.5 ° each) in the azimuthal direction (around the beam pipe) and into 64 rings in the polar direction (away from the beam pipe). The 48 sectors consist of 12 tiles, each containing four sectors. The active area corresponding to this sensor structure extends from 80 mm (inner radius) to 195.2 mm (outer radius) along the detector radius, as shown in Fig. 3.1 based on the structure of one tile.

The selection of the sensor type was based on a number of requirements:

- silicon-bulk material - should be n-type, because p^+ implants in n-material form isolated regions. Other solutions like double layer are expensive;
- resistivity of silicon-bulk - as high as possible, because it results in a smaller value of the depletion voltage and hence smaller power dissipation in the sensor;
- carrier lifetimes in silicon-bulk - as high as possible, because it results in a smaller value of the leakage current leading to a better signal-to-noise ratio (S/N). The S/N is a commonly used parameter to determine how well the signal can be observed above the background noise which in turn impacts the resolution of the signal;
- sensor-thickness - as small as possible, because it results in a smaller value of the depletion voltage and a higher value of the electric field inside the sensor at a given voltage. This leads to a better charge collection. It also implies less material for particles to traverse and allows to exploit the limited space in the experiment for other purposes.

Knowledge of available silicon-sensor technology, as well as remarks and suggestions from Hamamatsu experts, led to the detailed design of a single tile. These sensor tiles are made of n-type silicon, with p^+ strips on n^+ back-plane, and have crystal orientation of $\langle$ 100 $\rangle$. They are based on 6″ wafers technology and each tile contains four azimuthal sectors (denoted from left to right as L2, L1, R1 and R2), which for 12 tiles completes a full 360 ° layer. These wafers, which were originally of 500 - 700 μm in thickness, were thinned to 320 μm. The tiles were produced by Hamamatsu in 2009, and one of the sensor-tiles can be seen in more details in Fig. 3.1. The silicon-sensors have the following basic parameters:

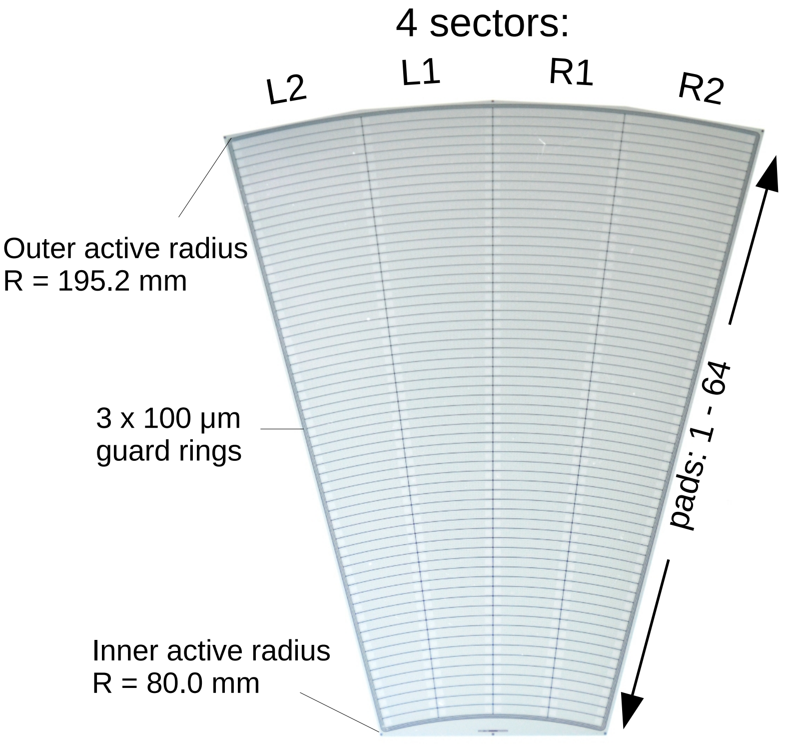

Figure 3.1: The silicon-sensor tile with four sectors, 7.5 ° opening angle each, and 64 pads in each sector.

- pad pitch of 1.8 mm;
- pad p^+width of 1.6 mm;
- pad Al metalization width of 1.7 mm;
- three guard rings, the presence of which restricts the leakage current from the active sensor area by insulating it from the edge of the sensor.

In total, Hamamatsu produced 40 such detectors; 20 for IFJ PAN Cracow, 10 for DESY Zeuthen and 10 for Tel Aviv University. Recently, the remaining 20 bare sensors that were not assembled up to now, were brought to the Tel Aviv laboratory for tests and assembly.

3.2 Measurement system description

The characterization measurements of the silicon sensors are a demanding both in time and in resources. Accurate measurements requires a large number of sampling points with many repetitions for each measured pad (diode). As noted earlier, each of the LumiCal prototype sensor-tile has 256 pads organized in 4 sector of 64 pads each. When considering that each one of the two LumiCal planned for the ILC (one for each detector) will have 720 such silicon sensors, the need of fast and efficient measurement tools is clear.

In the past few years, there is an effort to measure the LumiCal sensor in the FCAL collaboration lead by the Tel Aviv silicon laboratory. This effort gets paramount importance during the preparation period for major beam test campaigns, where a certain number of tested sensors is needed. The Tel Aviv laboratory joined this effort by developing a silicon sensor test stand, based on a probe-station [55] received from DESY-Zeuthen. An extensive measurement of the few sensors performed in the Tel Aviv lab are described in [57]. These measurements were preformed manually and lasted several working weeks for each sensor. This raised the need for an automated measurement system. Two different automated measurement systems that were used for LumiCal sensors are described next.

3.2.1 Semi-automated measurement systems

The first major effort for fast measurements of the LumiCal silicon sensor was carried out in 2015 with the collaboration of the FCAL group at DESY-Zeuthen. There, a unique system was developed for the measurements of silicon sensors for the tracking detectors of the CMS [58] and ATLAS [59] experiments. The system was based on the semi-automatic probe-station PA200 by Cascade Microtech [60] with a Labview-based data acquisition (DAQ) system that controls both the probe-station and the measurement instrumentation. The DAQ system is also connected to web based data-base that is saved for each measurement, including the raw data with all the calculated variables from the measurement. The probe-station is presented in Fig. 3.2.

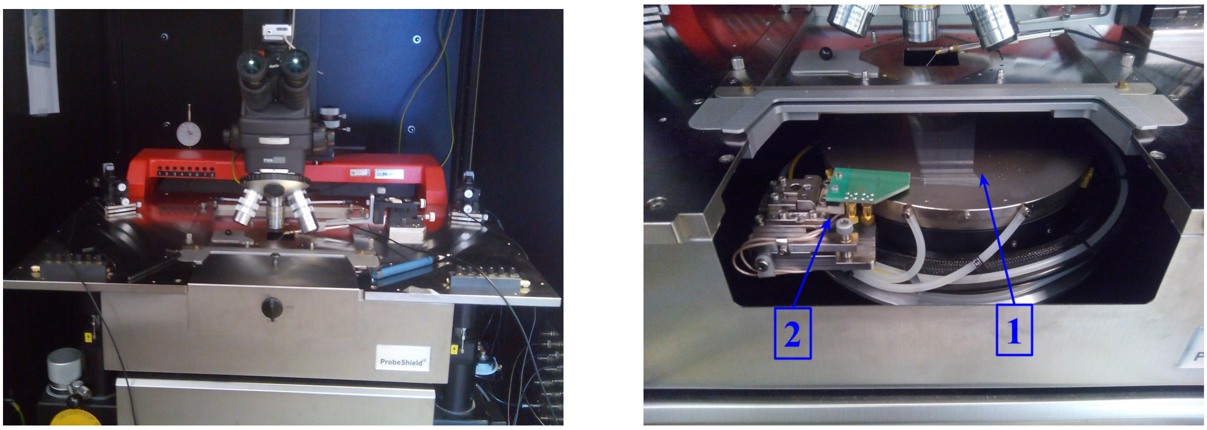

(a) (b)

Figure 3.2: (a) The semi-automatic probe-station, PA200, at DESY-Zeuthen in a closed position. (b) A closeup of the system in an open position where the electrical chuck (pointed by 1) with the wedge-card (in green, pointed by 2) is seen outside the system, ready to receive a sensor for measurement.

The electrical chuck is placed inside a closed compartment where the temperature and humidity is kept under close control. The closed compartment can be seen in a closed position in Fig. 3.2(a), and in an open position in Fig. 3.2(b), without a sensor loaded into the chuck. The chuck provides the voltage to the sensor, holds it in place by a vacuum system, and sets its temperature by an internal air-cooling system. The system automated principle is based on the electrical chuck movement control, while the measurement needles are kept at the same position. To switch between positions, the chuck movements proceed in three steps; first the chuck is moved down to disconnect the sensor from the needles, then it is moved in the new position for the next measurement, and only then it is slowly moved back up to establish the contact between the sensor and the needles. For grounding, the chuck holds a wedge-card that can contact the same position on the sensor throughout the measurement. The wedge-card (in green) can by seen on the left side of the golden chuck in Fig. 3.2(b). By programming in the DAQ the map of the measurement positions, the system moves automatically between positions.

One limitation of the system is that the needles remain in constant position, such that it cannot handle properly the geometrical differences along the sensor. This limitation complicates the measurement of LumiCal sensors by the system. Although, as noted in Section 3.1, the pitch between pads are constant, the position of the surrounding closest neighbors, needed for grounding, changes along the sensor and only three out of the four nearest neighbors of each pad can be grounded at the same time. This require that for each sector from the LumiCal sensor, three different positions are needed for each type of measurement (I V or C V), one for the first and last pad (where no ground is required on one of the sides) and one for the rest of the pads in the sectors.

In total the last six LumiCal sensors from Tel Aviv were fully measured during the campaign in preparation for the 2015-2016 beam tests. Three additional sensors from DESY were partly measured at a later stage. Usage of the semi-automated probe-station increased the measurement rate significantly, and a single sensor could be fully measured in less than two days.

3.2.2 Upgrades to the sensor measurement system

The description of the initial set-up for the measurement of silicon sensor at the Tel Aviv silicon laboratory was part of a previous work [55], and it was based on work by the FCAL laboratory from DESY-Zeuthen and Cracow [58, 61]. In the past few years, the Tel Aviv silicon laboratory has undergone a major upgrade as part of the center of excellence "the Quantum Universe" of the I-CORE program [62]. The main infrastructural improvement consisted of installing a class 10,000 clean room of $10\,\mathrm{m}^2$ size inside the laboratory area. Another improvement in the laboratory capabilities was due to the addition of a semi-automated wire bonding machine received from the DESY-Zeuthen laboratory, that allows on-site assembly of silicon sensor modules.

During the lab upgrade an effort was invested in improving the probe-station stand in order to have better control of the environmental conditions. Since the sensor dark current is highly dependent on the temperature, a new water cooled metal plate was placed in thermal contact with the electrical chuck for the sensor temperature stabilization and control. The plate is connected through thermally shielded pipes to a closed water cooling and circulation system that allows to set a specific water temperature. The temperature dependence can be seen in Fig. 3.3, which clearly shows the increase of the dark current with temperature on the same pad. Having temperature-stable measurements enables the comparison of response for different pads and tiles. In addition, a nitrogen flow system was introduced to remove humidity from the sensor surface for the purpose of current measurement stability.

An extensive measurement of a few sensors with these improvements was performed manually and the results are described in [57].

The latest upgrade of the probe-station consisted of adding a specially designed electronic switching system for automating the measurement process. The commercially available systems have a number

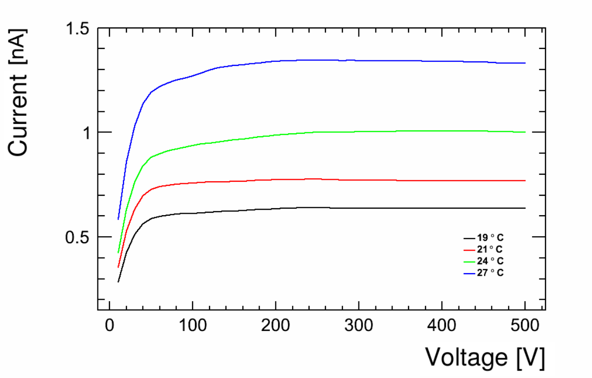

Figure 3.3: Measurements of the pad dark current, I, as a function of voltage, V, at different temperatures, for the LumiCal sensor prototype, after the probe-station upgrade.

of shortcoming. First they usually contain only a small number of channels; for large number of channels, several modules need to be placed together inside a dedicated crate. This kind of systems are expensive and complex. In addition, they require a large number of shielded cables to be connect to all the pads.

Recently a joint cooperation between the CMS experiment and the CLICdp collaboration successfully developed and commissioned an automated, compact, modular and cost efficient system for large area silicon pad sensor characterization [63]. The R&D of the system, under the name ARRAY (switching mAtRix pRobe cArd sYstem), was driven by the CMS experiment decision to adopt a similar concept to that of LumiCal, of a highly granular large sampling calorimeter (HGCAL) in the upgrade of its endcap calorimeters for the high luminosity upgrade of the LHC, HL-LHC [64]. In contrast to the semi-automated probe-station described earlier in Section 3.2.1 which moves the chuck, the ARRAY automation was achieved by connecting all pads in the sensor simultaneously, without moving parts, and switching the pads connections to the measurement devices as demonstrated in Fig. 3.4.

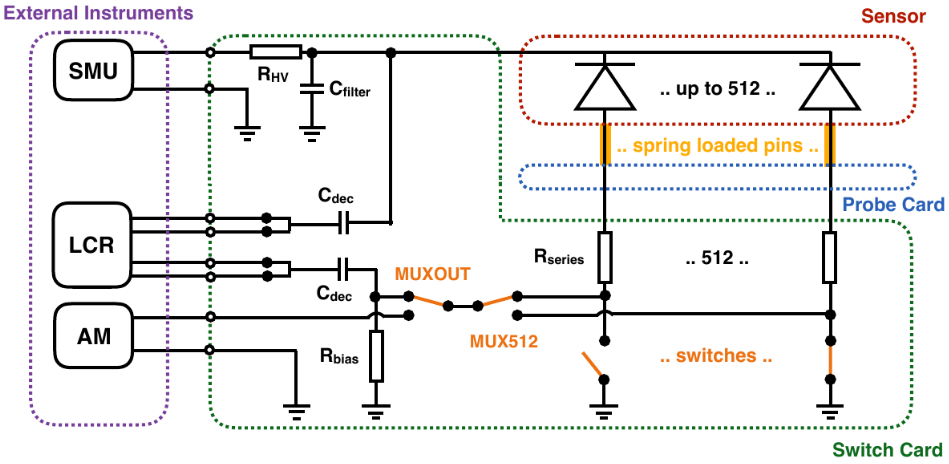

Figure 3.4: Sketch of the switching mAtRix pRobe cArd sYstem, ARRAY, layout. The switch card (inside the black frame) provides the sensor high voltage and connects the sensor pads through the probe card (inside the blue frame) to the measurement devices.

The HGCAL current design is based on both 6″ and 8″ size silicon wafers. To support the sensors development phase where several sensor layouts are tested and to be able to support other sensor layouts like the ones of LumiCal, ARRAY is built as an add-on to a probe-station with two parts. To allow the required flexibility, the first part is a relatively simple probe card that can be developed for each sensor layout. The probe card is a passive device that provides the connectivity to the sensor. As the sensor geometry changes, only the probe card layout has to be adapted. The probe card consists of an array of spring-loaded pins that are used to ensure a uniform and full contact to all pads in the sensor. The probe card provides an additional input that allows the use of external needles for the guard ring manual connection.

The heart of the system is the switch card that is common to all sensors. In the switch card, the signal originating from the probe card is routed via a three-level array of a solid state multiplexer towards the readout instruments. At the card output, the signals are routed through another multiplexer (output multiplexer) that enables the switching between the I V and C V output circuits. The switch card provides six coaxial BNC connections to a source measurement unit (denoted by SMU in Fig. 3.4) that supplies the high voltage and measures the sensor total current; to a LCR meter (LCR) for the capacitance measurement and an ammeter (AM) for the pad current measurement. The high voltage is connected to the switch card, routed via the filters to the probe card and applied to the sensor back plane via the chuck. The switch card is controlled through Labview or Python libraries [65] via a USB serial interface. The settings of the switch card can also be changed manually using keys on the switch card.

ARRAY was adapted also for the LumiCal prototype sensors described in Section 3.1. One set, including one switch card and two probe cards for the LumiCal sensors, was manufactured at CERN. The system was installed and tested on the Tel Aviv probe-station during 2018 with the help of the experts from CERN. Figure 3.5(a) shows the system installed in the probe-station with the two cards connected together and held by an aluminum add-on inside the probe-station. Figure 3.5(b) shows a closeup of the probe card, under the aluminum holder, with a sensor on the chuck during alignment. The thermal chuck with the water cooling pipes can also be seen. During the tests, one full LumiCal sensor was measured, with promising results, although the guard ring was not connected. The use of the system for the measurement of a LumiCal sensor reduced the measurement time to about 5 hours. Since the system measures a complete sensor in a static position, an additional advantage is gained by the fact that the probability to damage the sensor during movements is reduced.

3.3 Measurements of silicon sensor characteristics

The first step to qualify a silicon sensor is to measure its electrical properties. The basic electrical characteristics usually are the capacitance, C, and the current, I, in individual pads, and their behavior as a function of the reverse bias applied on the sensor, V. From the measured characteristics, information on the quality and uniformity of the sensor tile can be extracted. The so called C/V measurement, the dependence of C on V, is sensitive to the pad structure and uniformity and allows to extract the depletion voltage and the resistivity of a particular pad. The I/V measurement, the dependence of I on V, determines the value of the dark current at a voltage where the sensor is fully depleted and reveals deviations from the reverse diode behavior where breakdown occurs. These results quantify the quality of a single pad, and determine the pad performance as a sensing unit.

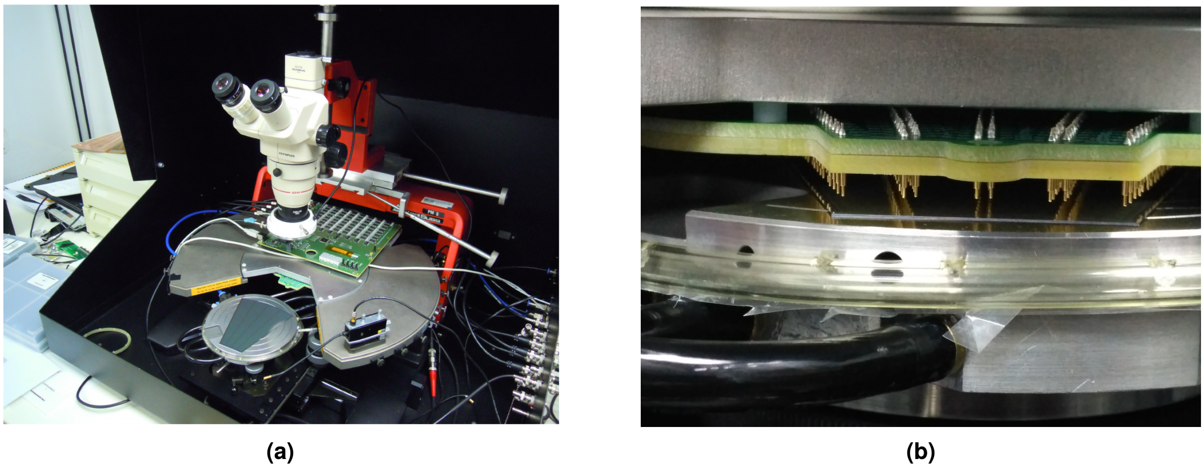

(a) (b)

Figure 3.5: (a) Full view of the ARRAY installed in the Tel Aviv laboratory probe-station where the switch card and its matrix of multiplexer is visible on top of the aluminum holder. (b) Closeup view of the probe-card with its spring-loaded pins above the LumiCal sensor on the electrical chuck. The thermal chuck with the water cooling pipes can also be seen below the electrical chuck.

3.3.1 Capacitance measurements

The pad total capacitance, C_t, is the sum of two major parts: the geometrical capacitance, C_g, arising from the separation of charges by the sensor depletion layer, and the inter-pad capacitance, C_i, that originates from the proximity of the pads to each other. From the capacitance measurements as a function of the voltage, a number of sensor characteristics like the depletion voltage, V_d, the depletion width, w, the donor density, N_d, and the sensor bulk resistivity, can be inferred.

Since the sensor tile has a relatively large pad area, C_t is mostly a geometrical property of the area. Capacitance in a semiconductor diode is created from the accumulated charges on both sides of the depletion layer that acts as a dielectric layer. The C_g capacitance can be assessed within the parallel-plates model with the depletion layer width as the separation between the plates. Therefore

$$C_g = A\frac{\varepsilon_{Si}\varepsilon_0}{w} = \begin{cases} A\sqrt{\frac{\varepsilon_{Si}\varepsilon_0 e N_d}{2V}} & \text{for } V < V_d \\ A\frac{\varepsilon_{Si}\varepsilon_0}{w_m} & \text{for } V > V_d, \end{cases} \tag{3.1}$$

where ε_0 is the vacuum permittivity, $\varepsilon_{Si} = 11.68$ is the relative permittivity of silicon, A is the pad area, V is the bias voltage, V_d is the depletion voltage, w is the depletion-layer width and is a function of the voltage V, w_m is the maximum depletion-layer width, e is the electron charge, and N_d is the donor density.

Equation (3.1) implies that the capacitance decreases with increasing width of the depletion layer which in turn increases as square root of the bias voltage up to the depletion voltage. The depletion voltage is the voltage when the depletion layer increases to the full width of the sensor. For bias voltage higher than the depletion voltage the capacitance is constant. A few examples of the pad capacitance as a function of the bias voltage, C/V for different pads along the same sector of one of the sensors (sensor Nr 20) are presented in Fig. 3.6

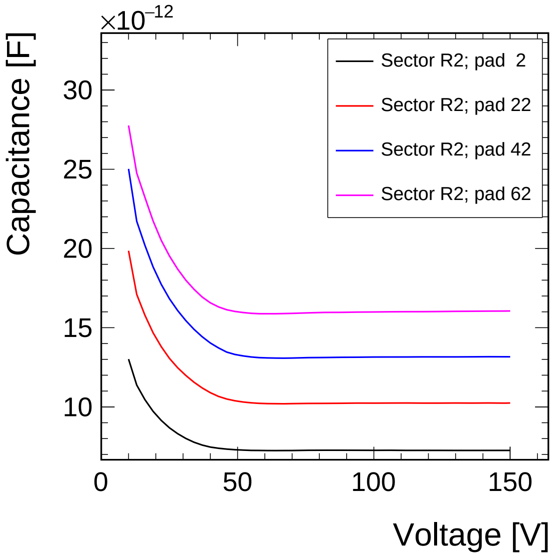

Figure 3.6: LumiCal pad capacitance measurements as a function of the bias voltage of pad 2 (black), 22 (red), 42 (blue) and 62 (pink) of the right edge sector R2 of sensor Nr 20 (see Fig. 3.1 for details).

The pad capacitance is determined as the average of the measured capacitance above 100 V. As expected, in Fig. 3.6 higher pad number correspond to larger capacitance values. Because the pad number inside a sector represents the radial distance from the bottom part of the sensor and since all pads have the same opening angle and radial width, it is also proportional to the pad area and its capacitance at full depletion. Moreover, since the pad area depends linearly on the pad number, the dependence of the measured capacitance should follow the linear trend and have similar behavior for different sectors and sensors. This is shown in Fig. 3.7 in which the pad capacitance is plotted as a function of the pad number for each sector of the sensors that were fully measured. Fig. 3.7(a) - Fig. 3.7(f) contain the results for the sensors that were measured at DESY-Zeuthen (see Section 3.2.1), and Fig. 3.7(g) presents the first measurements performed in Tel Aviv with the ARRAY system.

From Fig. 3.7 it seems that the capacitance measurements for all sensor are similar. The value of C for the sensor measured in Tel Aviv is systematically lower than for the sensors measured at DESY-Zeuthen by order of 0.9 pF in the inner sectors and 0.5 pF in the outer ones. However, since this particular sensor was only measured in Tel Aviv, it is difficult to make strong statements.

Only a few pads (like in sector L1 of sensor Nr 18 and in sector L2 of sensor Nr 24), deviate from the linear behavior, presumably due to weak contact of one of the probe needles. Sensor Nr 1 (Fig. 3.7(g)) shows a bump around pad 22 of sector L2, and at a lower level also of sector L1. This pad was the only one that was found post-factum not to be connected to the probe card during the measurement, probably due to imperfect alignment of the sensor relative to the card. The higher values of C in the pads surrounding pad 22 are due to the spread of the depletion layers and electric fields of the neighboring pads (that were connected) into the vacancy introduced by the lack of grounding in pad 22.

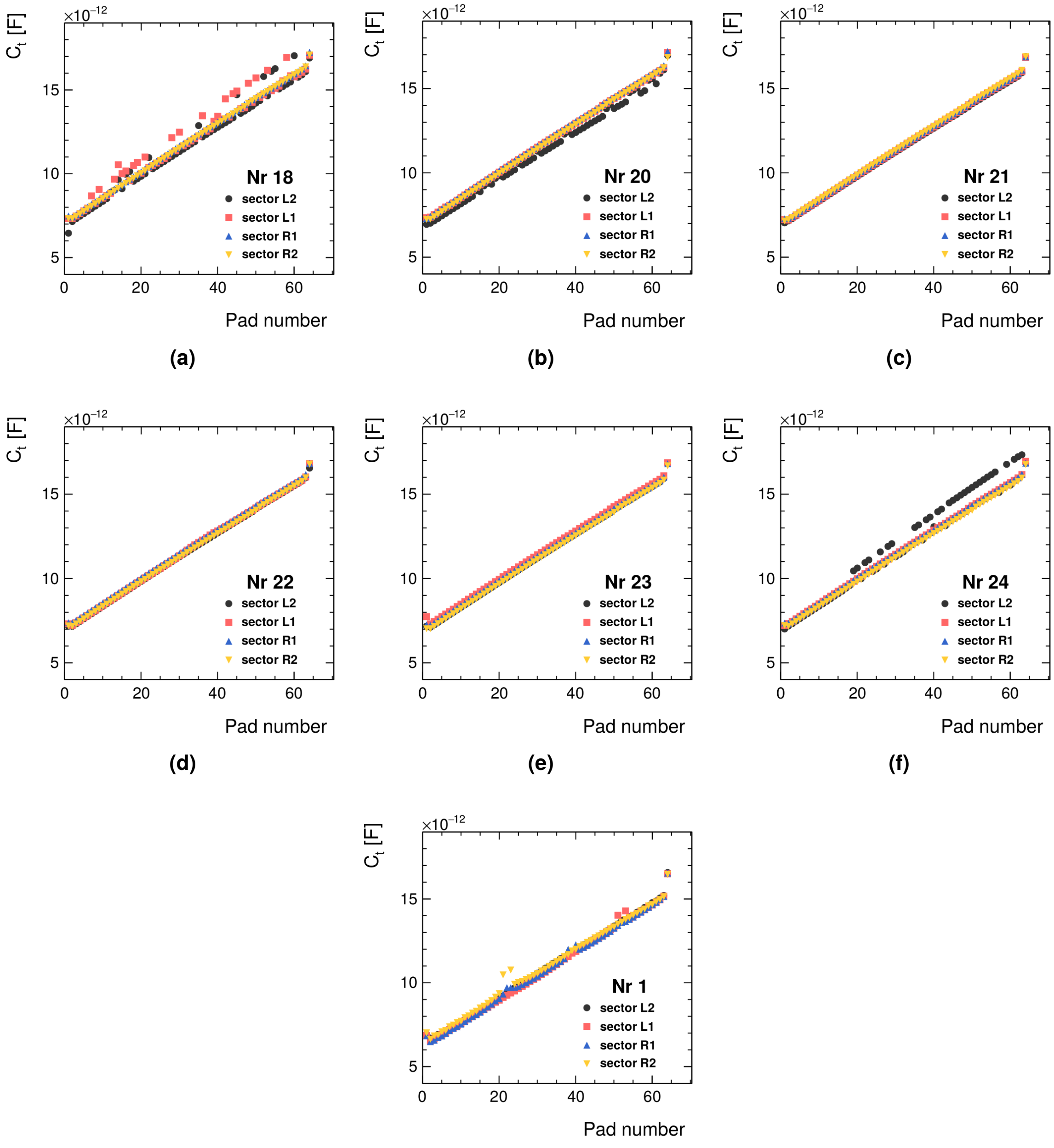

Figure 3.7: Pad capacitance as a function of the pad number for each sector as denoted in the figure, for sensors Nr 18, 20-24 that were measured with the semi-automated probe-station of DESY-Zeuthen, and for sensor Nr 1 that was measured with the ARRAY switching system in Tel Aviv.

3.3.1.1 Depletion voltage

As described above, the depletion layer width w depends on the bias voltage applied to the diode. When w reaches its maximum value, w_m, the diode is fully depleted. The value of w_m is limited by the thickness of the sensor d. The voltage needed to extend the depletion layer to the full thickness of the sensor is denoted by V_d and is given by

$$V_d = \frac{eN_d w_m^2}{2\varepsilon_0 \varepsilon_{Si}} . \tag{3.2}$$

In normal operating conditions, only the charge produced in the depleted volume can be detected and therefore the maximal signal charge is achieved when full depletion is reached. In order to determine the sensor operating voltage and to test for problems in sensor-thickness manufacturing, the depletion voltage needs to be determined. It can be determined from Eq. (3.1) and from Fig. 3.6.

It is easier to determine the depletion voltage from the C/V measurement using the $\log(C) - \log(V)$ plot, as shown in Fig. 3.8. For each pad, the depletion voltage is determined as the crossing point between two linear fits in the $\log(C) - \log(V)$ plot. The first linear fit is preformed for $V < 30\,\mathrm{V}$ and the second fit for $V > 100\,\mathrm{V}$.

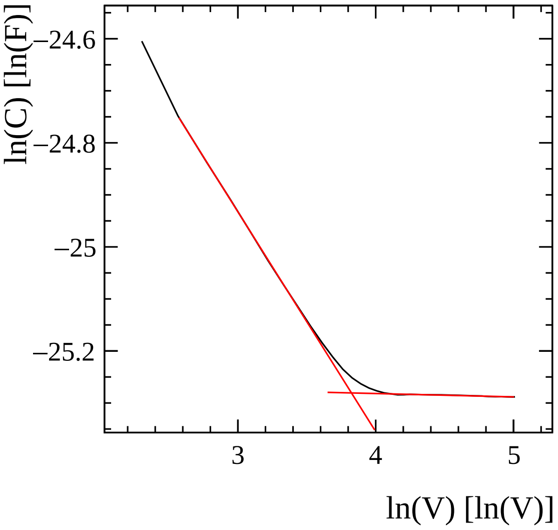

Figure 3.8: LumiCal pad measurements : the logarithm of the capacitance C as a function of the logarithm of the voltage V. The red line is the result of fitting straight lines below and above the region in $\log(V)$ that encompasses the value of the depletion voltage.

The depletion voltage, as noted in Eq. (3.2) does not depend on the pad area, and should be the same for all pads.

In Fig. 3.9 the depletion voltage of each pad is presented as function of the pad number, for each sector in the sensors that were fully measured. A previously, Fig. 3.9(a) - Fig. 3.9(f) represent the sensors that were measured at DESY-Zeuthen, while Fig. 3.9(g) presents the results from the ARRAY switching system in Tel Aviv. The differences between the depletion voltage of different pads, can be explained by the sensor property, like the donor density and the sensor thickness.

All measured sectors show similar bulk behavior, of higher depletion voltage in the sensor center and smaller values near the edges (sectors R1 and L1 in most of the sensors show locally a different

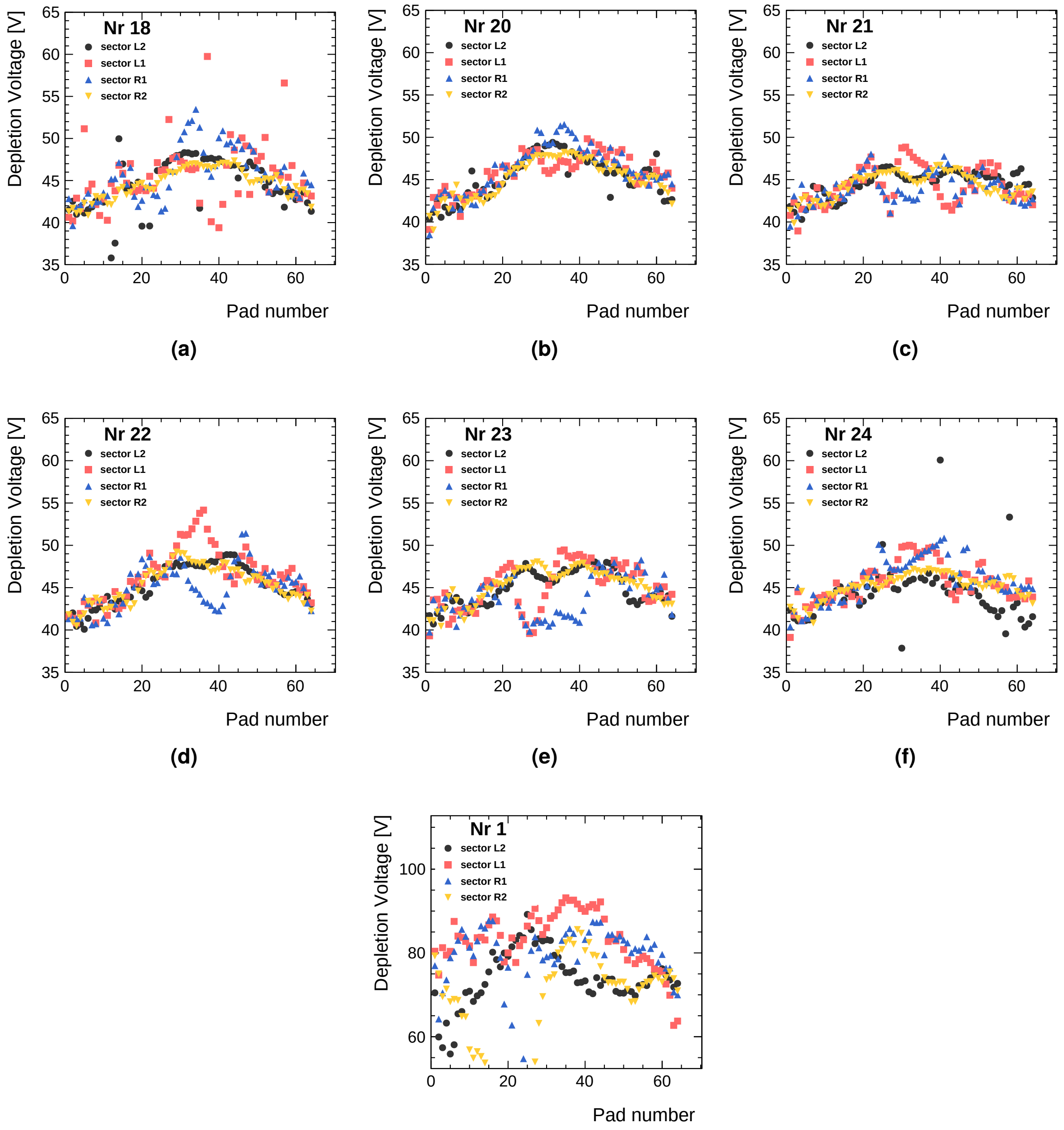

(a) (b) (c)

(d) (e) (f)

(g)

Figure 3.9: The depletion voltage as a function of the pad number for each sector as denoted in the figure, for sensors Nr 18, 20-24 measured with the semi-automated probe-station at DESY-Zeuthen, and for sensor Nr 1 measured with the ARRAY switching system in Tel Aviv.

behaviour for the very central pads because of limitations in the grounding options). This shape suggests that the donor density is higher in the center. The difference in scale between Fig. 3.9(a) - Fig. 3.9(f) and Fig. 3.9(g), can be explained by the fact that the measurement in Tel Aviv had issues with grounding, in particular because it was performed without grounding of the guard ring. Since the guard ring shields the inner part of the sensor from edge effects, when it is left floating the capacitance curve is deformed from its expected shape, and the depletion voltage calculation becomes biased.

3.3.1.2 Donor density

The donor density is a characteristic of the n-type silicon-bulk. As seen from Eq. (3.2), the depletion voltage and width depend on the donor density. Since the dark current of the sensor has a $\frac{1}{\sqrt{N_d}}$ dependence, the total power of the sensor will depend on N_d like $\sqrt{N_d}$, leading to a requirement of low density. As mentioned in Section 3.1, a high resistivity silicon-bulk is one of the requirements for the sensor.

The donor density in the n-type silicon-bulk can be determined from the C/V measurements. The first part of equation (3.1) can be rewritten as

$$\frac{1}{C^2} = \frac{2}{\varepsilon e N_d A^2} V. \tag{3.3}$$

An example of this relation for the same measurements as shown in Fig. 3.6, can be seen in Fig. 3.10. From the slope determined by a linear fit applied to the V range below the depletion voltage, one can estimate the average N_d in the pad area which comes out to be about $1 \times 10^{12}\ \frac{e}{cm^3}$. This result is similar to the one obtained in [61].

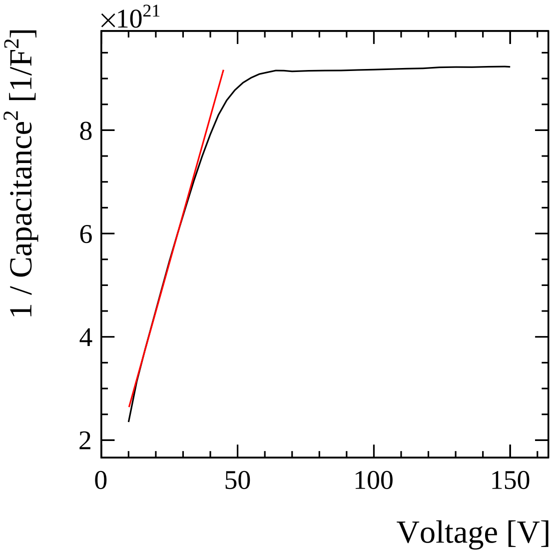

Figure 3.10: LumiCal pad measurements: the capacitance C expressed in terms of $1/C^2$ as a function of the voltage V. The red line represents a linear fit in the voltage range below the depletion voltage.

In Fig. 3.11 the donor density of each pad is presented as a function of the pad number for each sector in the sensors that were fully measured. The results show similar behavior to the results of the depletion voltage measurement shown before. It seems likely that, as conjectured before, donor density changes along the sensor lower and upper edges. Since N_d is derived from the capacitance measurement, similarly to the depletion voltage, it shows similar problems. Thus several pads from the central sectors of sensors Nr 18 and Nr 24 deviate from the continuity of all pads. The shift in scale of Fig. 3.11(g) from Fig. 3.11(a) - Fig. 3.11(f), can be explained by the grounding issues that deformed the capacitance curve and biased also the donor density.

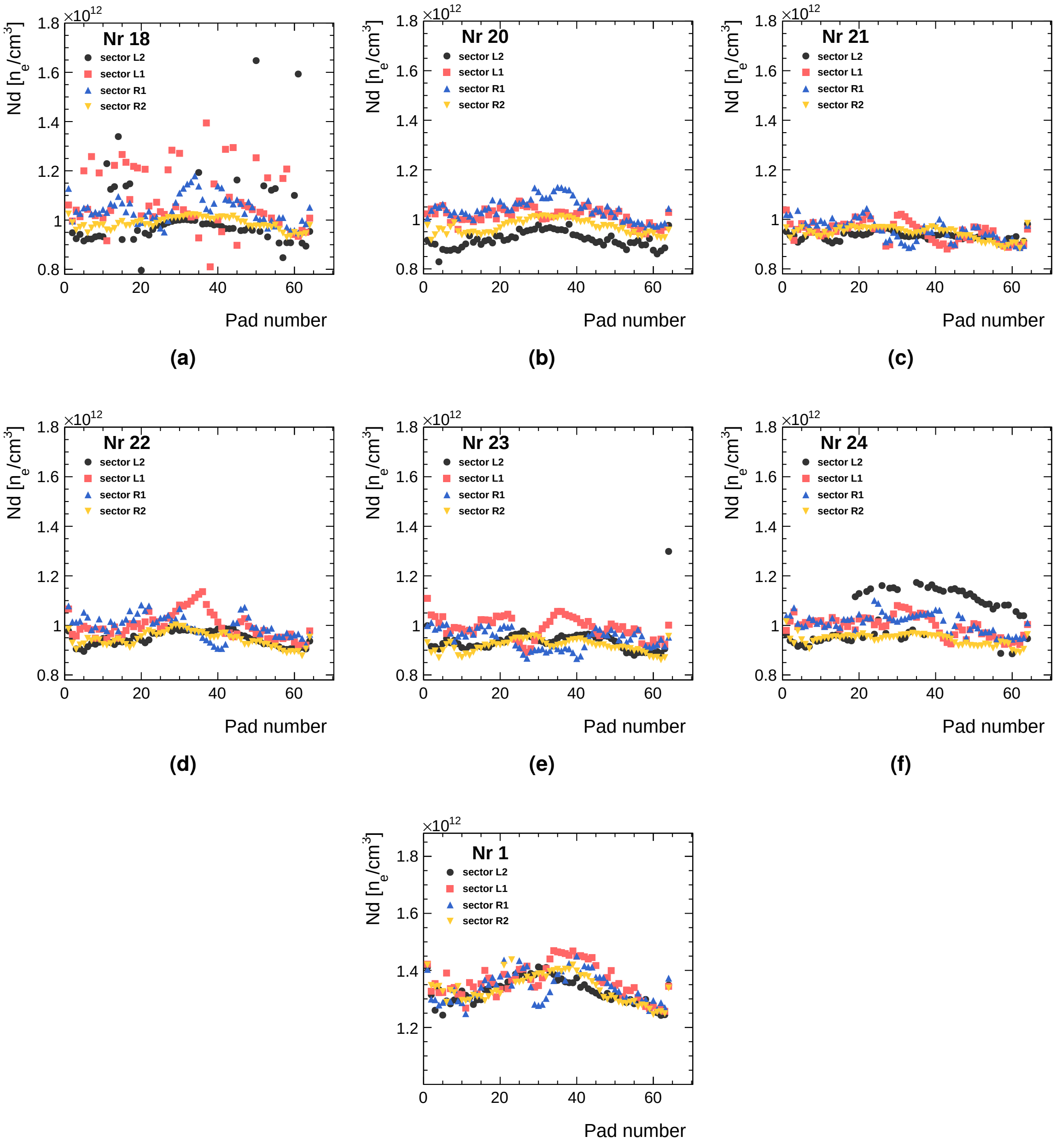

(a) (b) (c)

(d) (e) (f)

(g)

Figure 3.11: The estimated donor density as a function of the pad number for each sector as denoted in the figure, for sensors Nr 18, 20-24 measured with the semi-automated probe-station at DESY-Zeuthen, and for sensor Nr 1 measured with the ARRAY switching system in Tel Aviv.

3.3.2 Current measurement

When a reverse bias is applied to a semiconductor diode, a dark current is created. The leakage or dark current is the current flowing in the absence of external sources that move charges to the conduction band. The source of this current are charges that are randomly generated inside the depletion layer.

A typical current to voltage characteristic (I dependence on V, traditionally denoted as I/V) of a reversely biased silicon-sensor is composed of three ranges in V. In the first part, for voltage below V_d, the current increases according to equation (3.4). It is proportional to the current density on the surface of the pad, generated in the depletion volume, J_{vol}, which in turn is a function of the intrinsic carrier concentration n_i, and τ_g, the carrier generation lifetime,

$$I_{pad} = AJ_{vol} \approx -eA\frac{n_i}{\tau_g}\sqrt{\frac{2\varepsilon_0\varepsilon_{Si}}{eN_d}V}. \tag{3.4}$$

After the full depletion is reached, the I/V curve displays a plateau region in which the current increase is very small. This part also contains some additional surface-current contribution. At very high voltage, electrical breakdown occurs. This breakdown can eventually destroy the sensor. The measurement of the I/V curves is a very powerful tool for sensor testing. Almost all possible problems in the sensor production process lead to a deviation of the curve from the expected shape. An examples of I/V curves for few pads in the same sector of sensor Nr 20 is presented in Fig. 3.12(a). The I/V curve is affected by the grounding of the surrounding pads and of the guard ring, since charge is generated in all of the sensor volume, and it will be distributed to the grounded pads. As noted before, during the measurements on the semi-automated probe-station (Section 3.2.1) only three of the four closest neighbors were grounded. In the measurements of sector R1 and L1 (the middle sectors) the I/V curves are affected by this charge excess. This can be seen in Fig. 3.12(b) where two I/V curves are shown, one for a pad with only three neighbors (pad 2 of R2), all grounded, and one for a pad with only three neighbors out of four grounded (pad 22 of L1). In the latter case the I/V curve is very different, although the two pads have a similar response at low V values. In the region of $V < 200\,\mathrm{V}$, the rise of I with V is stronger than for a regular I/V curve because of the additional surface current which contributes above the depletion voltage. For $V > 200\,\mathrm{V}$ the rise in I is even stronger because when the electric field inside the depletion region becomes large, electric charges from the non-grounded neighboring pad are pulled in.

In Fig. 3.13 the current above the depletion voltage of each pad is presented as a function of the pad number for each sector, for the same sensors as for the C/V measurements. As expected from Eq. (3.4), the current is increasing with the pad number (increasing pad size) with a few exceptions. For the smallest and largest pad sizes, the current is larger due to the proximity to the sensor edge, although the guard ring was grounded. In other areas, bumps over a range of pads are observed, indicating that some pads draw extra current from the sensor. This behavior is mainly due to pulling current from the guard ring, as established by checking the behavior of the guard ring current in the same measurements (not shown). As can be seen in Fig. 3.13(g) for a sensor with all pads grounded, the current dependence on the pad number is much smoother, mainly because all pads are sharing the excess current. This indicates that connecting only three pads at the time amplifies any local imperfections in the guard ring, which become irrelevant when all pads are connected.

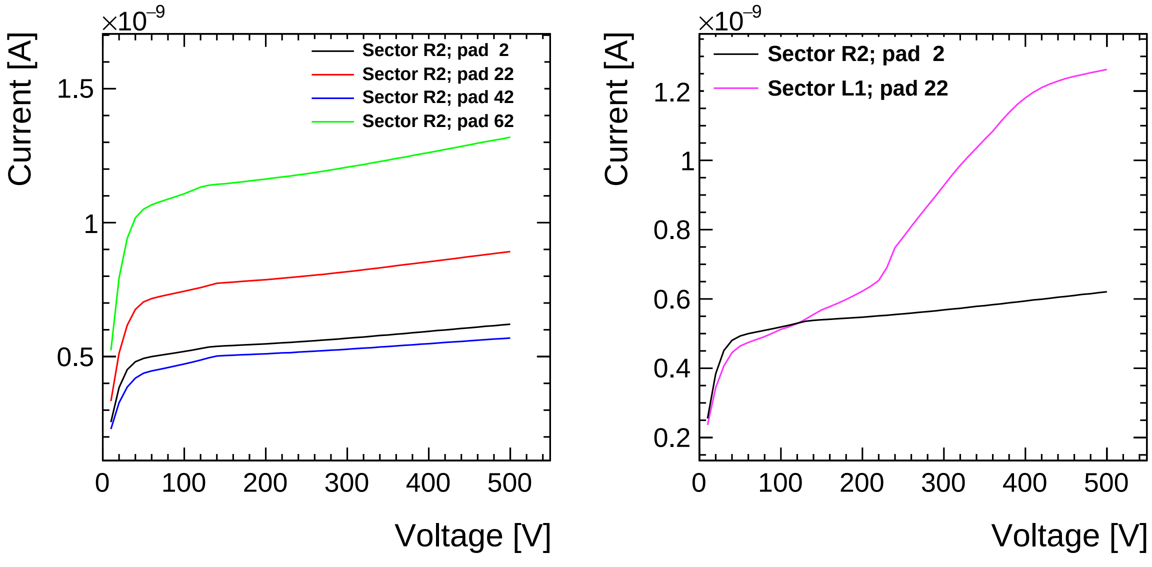

(a) (b)

Figure 3.12: (a) Pad current measurements in sensor Nr 20 as a function of the bias voltage in the right edge sector R2 for four selected pads as denoted in the legend. (b) A comparison between the I/V curve of pad 22 in the left middle sector L1 were one of the four neighbors is not grounded and a normal I/V curve for pad 2 in the right edge sector R2 where all three neighbors are grounded.

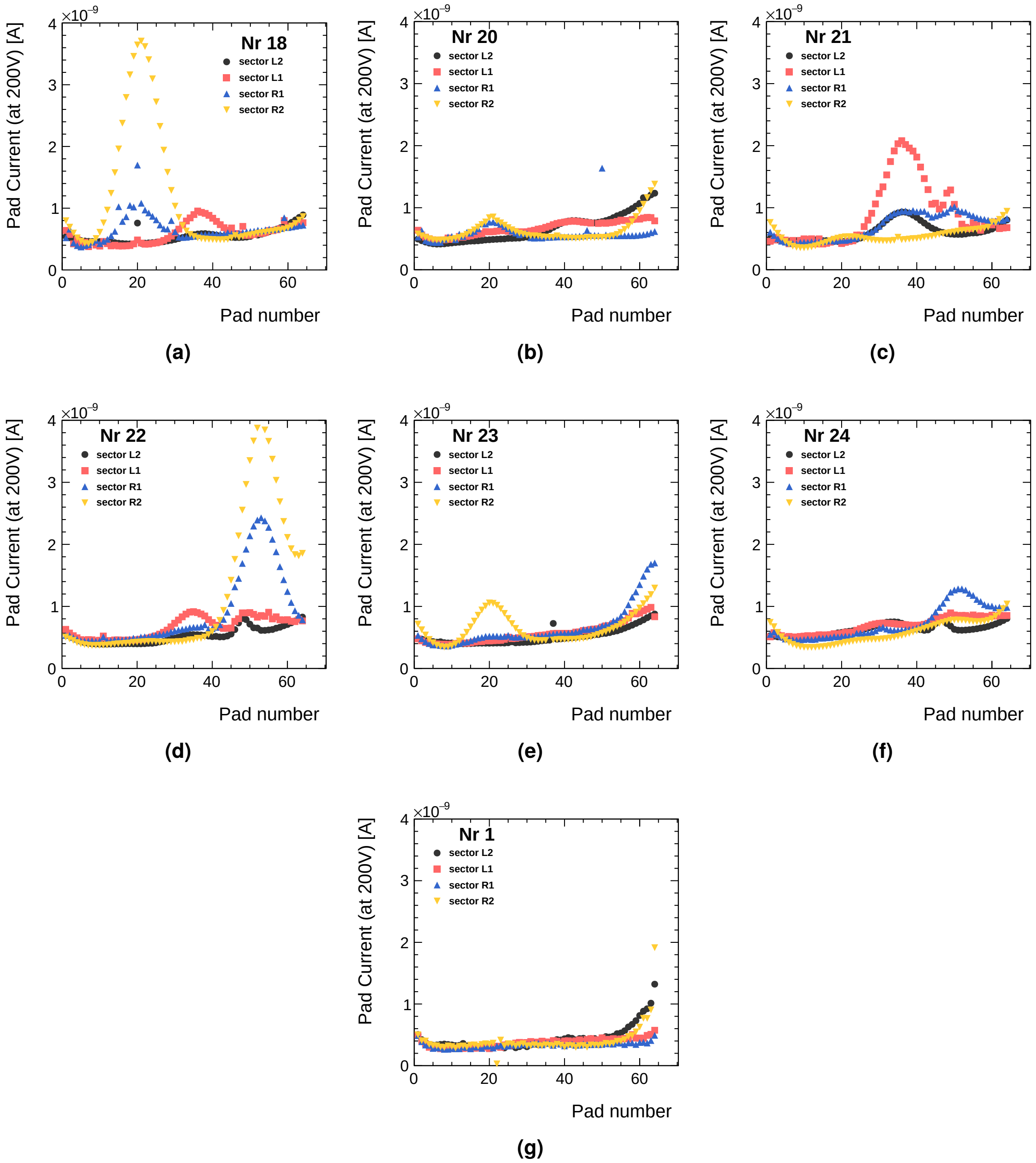

(a) (b) (c) (d) (e) (f) (g)

Figure 3.13: The plateau current as a function of the pad number for each sector as denoted in the legend, for sensors Nr 18,20-24 that were measured at the semi-automated probe-station at DESY-Zeuthen, and for sensor Nr 1 that was measured with the ARRAY switching system in Tel Aviv.

3.4 Thin LumiCal module

For silicon wafers to act as a detector, some connections are needed: a high voltage supply from the n^+side and a link to the electronic readout and ground is required from the other side. The sensors whose characterization results were presented, were used for assembling sensor modules that can be inserted to a calorimeter prototype to be tested in a test beam experiment.

The first LumiCal sensor module was designed for a single-layer campaign conducted between 2010-2011 whose results are summarized in [66]. This sensor module was also used in the first multi-layer prototype test held in 2014, the results of which will be discussed in Chapter 4. It used a thick 2.5 mm printed circuit board (PCB), serving as the mechanical support and high voltage supply. Conductive glue was used to mount sensor tiles to the high voltage printout on the PCB. A flexible Kapton foil with copper traces was glued to the sensor as a fan-out. Sensor pads were attached via wire bonding loops to the copper traces. A second wire bonding was used to connect the copper traces back to the PCB, that linked it to the electronic board through the connector. Figure 3.14 presents a picture, taken during the assembly of one sensor module with the microscope camera of the bonding machine, where all components can be seen. In the upper part of the picture, the machine bonding tool is seen. The sensor, in gray, seen through the orange Kapton foil, is glued to the green PCB, and the two sets of wire bonding can be seen. The first wire is between the sensor's pads and the golden rings that start the copper traces in the Kapton foil. The second wire connects the end of the traces in the Kapton foil to the traces on the PCB that lead to the output connector of the sensor module (not shown in the picture). Two such sensor modules were produced in Tel Aviv, one of which was used as a backup module for the 2014 test beam. The other module, assembled later, was equipped with different output connectors for testing alternatives to the multi-channel electronic chip, to be used as the default FCAL electronics when ready.

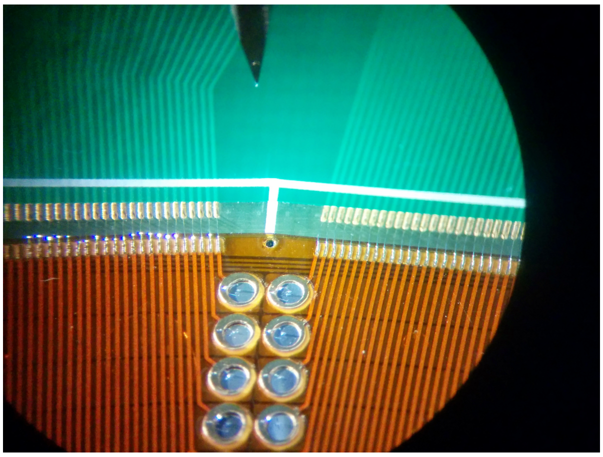

Figure 3.14: A microscope picture of an assembled sensor module from above, with the green PCB as a support from the backside (seen in the upper part). The silicon sensor is covered with the orange Kapton fan-out foil with its copper traces going from the gold rings to the small bonding pads at the fan-out end. The sensor, in gray and black lines, can be seen through the Kapton and the gold rings, wire bonding connections are also seen in the gold rings and at the edge of the Kapton fan-out.

In order to reach the design goals of LumiCal, it was essential to design and use new thin submilimeter sensor modules to be inserted in the narrow gaps between the tungsten planes. The LumiCal design calls for a 1 mm gap between the disks of tungsten absorbers. Since the roughness and thickness uncertainty of the test tungsten plates can go up to 50 μm, the new LumiCal module needed to be no thicker than than 900 μm. The new module needed to be flat to preserve the desired thickness and in order to be able to handle it with vacuum holders. On top of the thickness requirements, the module had to be mechanically solid to protect the fragile silicon sensor and to allow for easy handling during assembly and installation. And most importantly, it had to preserve all the functionality of the first LumiCal module described at [66].

The design of the new thin submilimeter sensor modules is presented in Fig. 3.15. The module was assembled on top of a support structure made of carbon fiber composite with a thickness of 100 μm in the sensor-gluing area and of 750 μm in the surrounding area ("solders") that provided extra mechanical strength for the module and to set its maximum thickness. For the support structure, plastic 3D printing was also tested but was found to be less suitable than the carbon fiber solution. The powering circuits and the fan-out part were made from flexible Kapton-copper foils. The thickness of the high voltage part was about 70 μm and it was glued to the back n-side of the sensor with conductive glue, and with epoxy glue to the support structure. The fan-out part was about 120 μm and was glued to the front side (p-side) of the sensor using epoxy glue. All 256 pads of the sensor and the inner guard ring were connected to the fan-out traces. Special fixtures were designed and produced to ensure the necessary thickness and uniformity of three glue layers between different components of the LumiCal detector module all over the area of the sensor. The thickness of adhesive layers between components was within $10 - 15\,\mu$m.

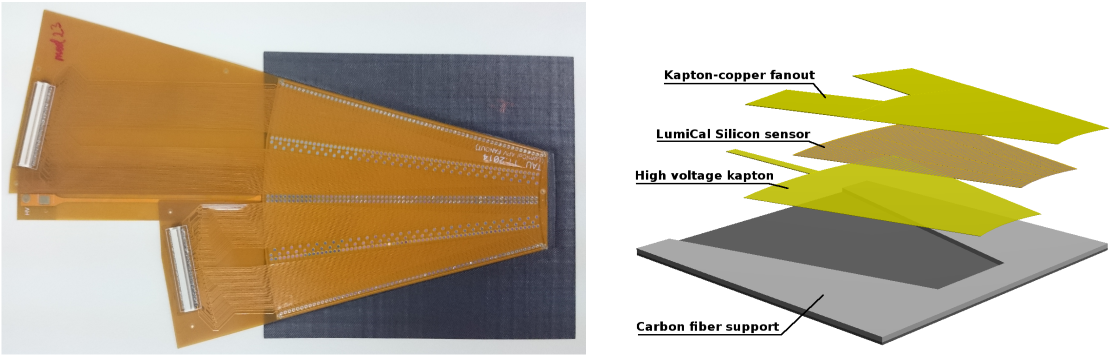

(a)

(b)

Figure 3.15: (a) A thin LumiCal module. The black part is the carbon fiber support. The silicon sensor is covered by the Kapton-copper fan-out which has two connectors for front-end boards. (b) The module layers assembly, the thickness of adhesive layers (not shown) between components is within 10 - 15 μm. The total thickness is 650 μm.

The fan-out part was redesigned from the first LumiCal module. In the new design the copper traces were extended from the sensor area into two separate bands ("bunny ears"), each carrying the traces of two sensor sectors to a 130 pin Panasonic connector of the front-end board. In order to study the effect of the longer traces, the two bands were designed with asymmetric lengths, the left one short, only 5 cm, similar to the distance between the traces end and the board connector of the first LumiCal module. The right band was long and extended to a length of 10 cm, allowing more flexibility in the connection to the front end cards. The placement of the Panasonic connector on top of the Kapton layer was possible by hardening the end side of the Kapton band. Since the connector was placed on the Kapton, a set of Ultrasonic wire bonding connections (for the 256 pads and guard ring) between the Kapton and a PCB, as in the LumiCal first module, was avoided.

Ultrasonic wire bonding was used to connect conductive traces on the fan-out to the sensor pads. The ultrasonic wire bonding proved to provide good electrical performance, but for a module thinner than 1 mm, the wire loops, which were typically 100−200 μm high, caused a serious problem when the module needed to be installed in a 1 mm gap between absorber plates. The parameters of the bonding machine were studied and tuned to make the loop as low as possible and technically acceptable. The sampling based measurements, which were done using a confocal laser scanning microscope, showed that the loop height is in the range from 50 μm to 100 μm.

Several alternative solutions were considered for connecting sensors with front-end electronics to avoid the damage-prone wire loops. One of them is the tape automatic bonding (TAB) technique [67], which was implemented in one of the sensor planes.

CHAPTER 4

First prototype calorimeter study

To check the performance of the LumiCal and BeamCal designs, a series of beam-test campaigns was conducted. In the beam tests performed between 2010 and 2011, the full functionality of a single LumiCal sensor plane was demonstrated. The results showed high efficiency for minimum ionizing particle detection. From studies of the detector response as a function of the electron-beam impact-point, a uniform performance was found, apart from a 10% reduction of the amplitude in the vicinity of the gaps between adjacent pads. The full description of the tests and the results of their analysis can be found in Ref. [66].

The next step in the detector prototype development was to prepare and conduct a beam-test study of a multi-plane structure. The main objective of this campaign was to demonstrate that a highly compact and efficient electromagnetic shower reconstruction in a prototype calorimeter can be achieved as required for high precision luminosity measurements. The first test was performed in October 2014, at the T9 beam line, located in the East Area of the Proton Synchrotron (PS) at CERN. The goals for the first test were, to preform single- and multi-board tests of the electronic readout, and to study the development of the electromagnetic shower and its description by Monte Carlo (MC) simulation. The two major requirements of the LumiCal design, the energy resolution and the precision reconstruction of the polar angle, were tested for the first time. In this chapter, the beam-test instrumentation will be described, the analysis of the raw data will be explained and measured results will be presented.

4.1 Beam test instrumentation

The PS is a key component in the CERN accelerator complex. Its main purpose today is to accelerate either protons to 24 GeV$/c$ or heavy ions to 5.9 GeV$/c$, and then to supply them to the Super Proton Synchrotron (SPS), and finally to the LHC. The PS beam is also used directly and indirectly, through secondary targets, for several beam lines for beam tests and experiments [68]. The LumiCal beam tests took place in the T9 beam line, using a secondary electron enriched beam created from a 200 mm beryllium and 3 mm tungsten target. The secondary beam, composed of hadrons, electrons and muons, was set with a narrow band centered at 5 GeV$/c$ of particle momenta, using a beam dipole magnet and collimators. The beam for the T9 area is provided in 400 ms long spills with a typical time separation of 33.6 s between spills.

At the entrance to the beam area the collimated beam was passing through two long Cherenkov counters filled with variable-pressure CO_2 gas. By setting appropriately the gas pressure, different types of particle can be tagged. Downstream from the Cherenkov counters, a pair of small wire chambers provided an online monitoring of the transverse, X and Y, beam profile.

In order to measure the particle track before the LumiCal structure, a beam Telescope was positioned just in front of the calorimeter stack. A simplified overall view of the beam and of the experimental set-up is presented in Fig. 4.1. The LumiCal structure, the beam Telescope and the data acquisition system (DAQ) will be describe in the following.

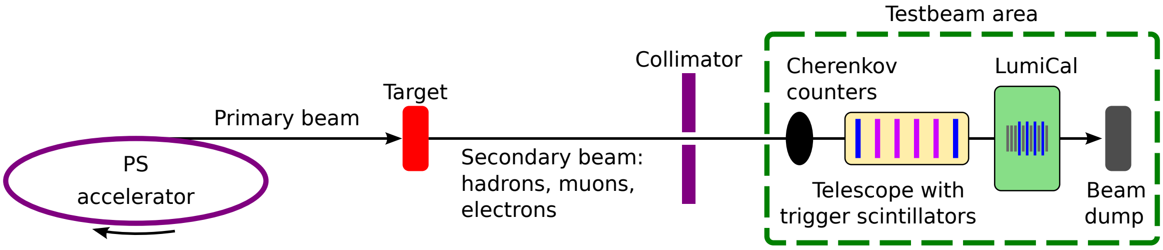

Figure 4.1: Schematic view of the beam and experimental set-up (not to scale).

4.1.1 LumiCal calorimeter prototype

The LumiCal prototype consists of of a mechanical structure with tungsten absorber planes interspersed with four fully assembled sensor planes inserted at different positions in-between the absorber layers.

4.1.1.1 Mechanical structure

To allow the multiple-plane operation, a mechanical structure was developed to meet the demanding geometrical requirements [69]. The required precision of the shower polar angle reconstruction imposed a precision in the positioning of the sensors of a few tens of micrometers. The most important component, the calorimeter layer positioning structure, included three aluminum combs with 30 slots each for the installation of the sensor planes with the required precision. Since only four detector planes were available to measure the longitudinal shower profile, the mechanical structure had to enable modifications in the prototype layout during the beam-tests. The overall view of the mechanical structure is presented in Figure 4.2.

As seen in Figure 4.2, the mechanical structure was placed under a modular aluminum hood. The hood served a few purposes; it kept the sensors in a dark controlled environment while functioning also as a Faraday cage, and it allowed an easy access to the front and back of the calorimeter stack without the need to dismantle the whole case. In addition, Figure 4.2 shows a bar reinforcement at one side of the case. It was designed to give flexibility with the orientation of the calorimeter stack, as it was used in the 2016 beam-test described in Chapter 5 and for cosmic muons measurements.

4.1.1.2 Absorber planes

As described above, the LumiCal design uses tungsten as an absorber. The absorber layers have a thickness of 3.5 mm, which is about one radiation length, X_0, for tungsten. The LumiCal prototype contained two types of absorbers made of two different tungsten alloys denoted hereafter as W-93 and W-95. The W-93 alloy consists of 93% tungsten, 5.25% nickel and 1.75% copper. The W-95 alloy has 95% tungsten and the fractions of nickel and copper is estimated as 3.5% and 1.5%, respectively.

In order to insert the tungsten plates, they are mounted in permaglass frames, as shown in Fig. 4.3. Special inserts located on both sides of the permaglass contain small bearing balls which provide precisely positioned support-points for the comb slots.

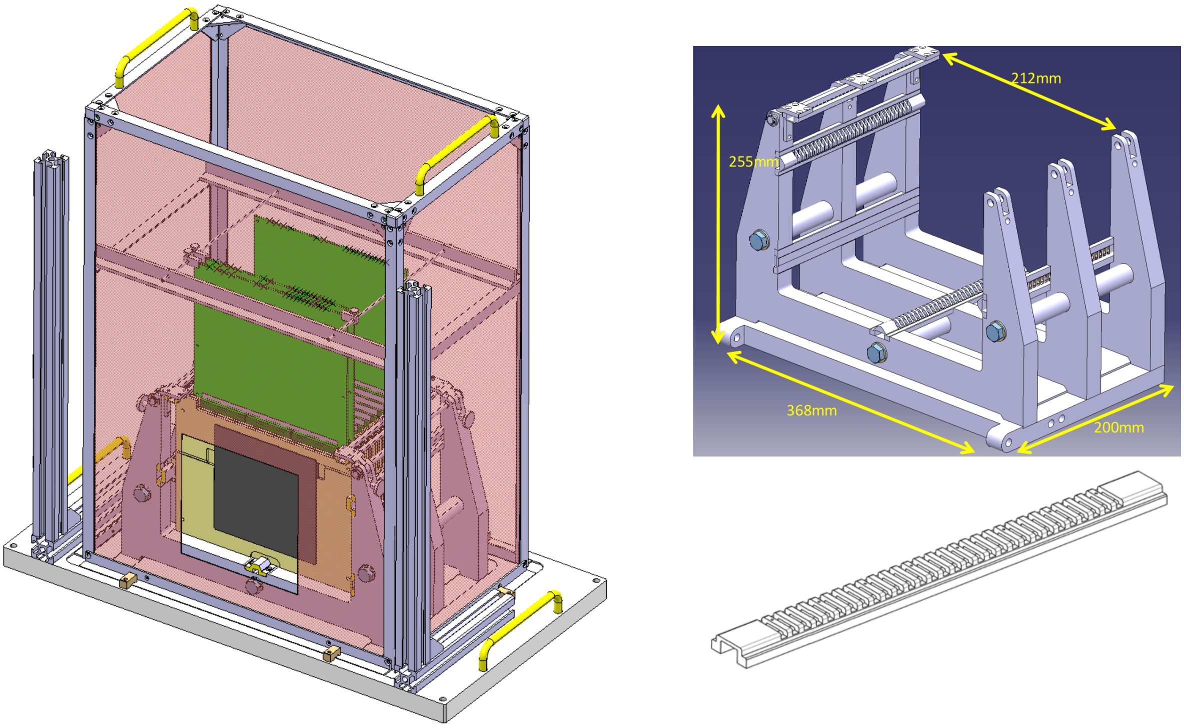

Figure 4.2: Left: scheme of the complete mechanical structure with the tungsten absorbers and readout boards installed. Top right: dimensions of the precision mechanical frame for the positioning of sensor and absorber planes. Bottom right: details of the retaining comb-jig for positioning of sensor and absorber planes.

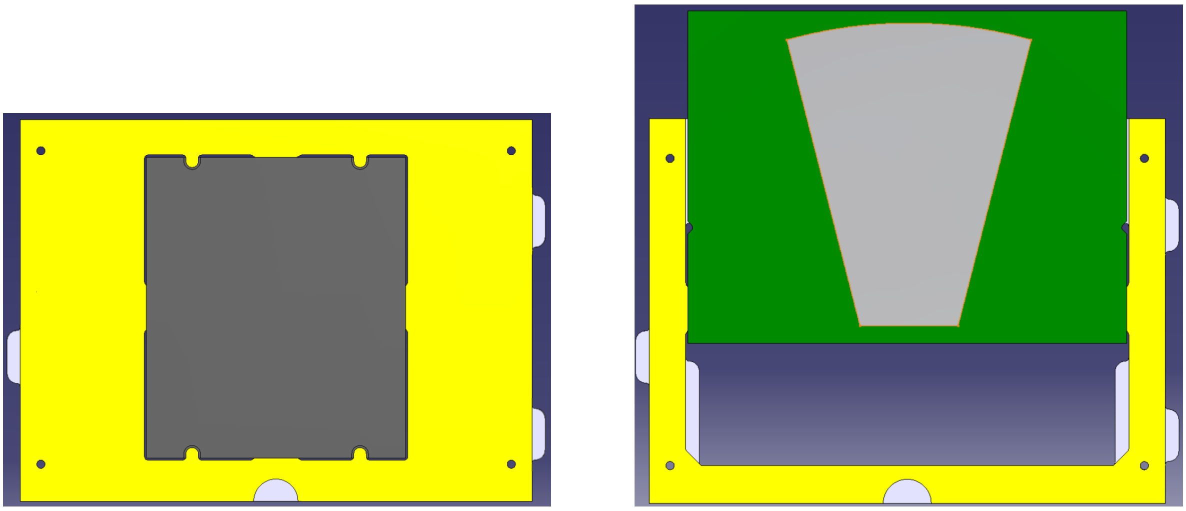

Figure 4.3: Detector layers supporting frames. Left: tungsten absorber (gray) in a permaglass frame (yellow). Right: sensor (gray) PCB (green) partially retracted from a permaglass frame (yellow).

The positioning precision of the supporting structure, as well as the tungsten absorber thickness uniformity, were extensively tested [69]. The maximum differences between the nominal and measured absorber plane positions did not exceed the required ±50 μm. A function test of the fully assembled stack was performed before the installation in the beam-test and the full prototype functionality was confirmed.

4.1.1.3 Detector module

The LumiCal detector module consists of two boards, the sensor board and the electronic board. The sensor board which was described in Section 3.4 was also mounted in a permaglass frame, as shown in Fig. 4.3, and was inserted into the structure slots in-between the tungsten layers.

The electronic board was connected via a 92 pin connector to the sensor board, and was used to process the analog signal, digitize it, and transmit it to the DAQ computer. In each electronic board, 32 channels were read out by four pairs of dedicated multi-channel front-end and 10-bit ADC ASICs. The sensor pads that were connected were pads number 51-64 of sector L1 and number 47-64 of sector R1, as shown in Fig. 4.4.

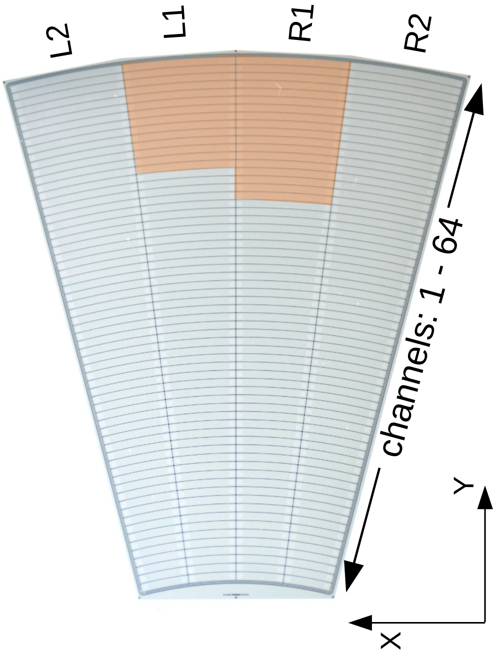

Figure 4.4: A prototype silicon sensor for LumiCal. L1, L2, R1 and R2 are labels for the sectors. The shaded area denotes the pads that were connected to the electronics in the beam-test.

Each channel of the front-end ASIC [70] consists of a charge-sensitive amplifier, a pole-zero cancellation circuit (PZC), and a first order CR-RC shaper. It was designed to work in two modes: a physics mode and a calibration mode. In the physics mode (low gain), the dynamic range of the front-end was adjusted to accommodate signals typically produced by electromagnetic showers, with up to 10 pC collected charge per channel. In the calibration mode (high gain), the dynamic range covered the signal amplitudes from relativistic muons to be used for calibration and alignment. To match the ILC timing, the shaper peaking time, T_{peak}, was set to about 60 ns. The prototype ASICs, containing 8 front-end channels, were designed and fabricated in 0.35 μm four-metal two-poly CMOS technology. For historical reasons, four of the channels (called hereafter MOS feedback) have about twice the gain of the other four (called hereafter R feedback).

To analyze the beam-test data and to perform pile-up studies, a sufficiently high ADC sampling rate and very high internal-data throughput between the ADC and the FPGA-based back-end electronics were assured. An 8-channel 10-bit pipeline ADC ASIC [71] was sampling the signals from the 8 front-end ASICs with 20 MS/s rate. The signals from 32 channels (4 pairs of front-end and ADC ASICs) were digitized with 10-bit resolution, resulting in a peak data rate of about 6.4 Gb/s. These data were processed by an FPGA-based data concentrator [72]. A picture of a fully assembled detector module is shown in Figure 4.5.

Figure 4.5: Photograph of a LumiCal readout module attached to a sensor.

4.1.1.4 Calorimeter configurations

During the beam-test, only four readout boards were available. Therefore only four sensor layers were used, noted here as S0-S3 according to the layer order in the stack. For 5 GeV electrons, the expected maximum of the shower is located around the 6$^{\text{th}}$ absorber layer. In order to measure the full shower development, at least 10 instrumented layers are required. Since only four layers were available, this condition could be met only with at least three absorber layers placed in-between the active sensor layers. However, this leads to a rather low sampling resolution which could result in large uncertainties in the shower shape.

Since the mechanical support-structure enables relatively simple detector geometry changes, a different approach was implemented. Three detector configurations were used, with the active sensor layers always separated by two absorber layers. By adding additional absorber layers upstream of the detector, the sensor layers were effectively moved downstream of the shower. The first stack configuration is shown in Figure 4.6. A summary of all configurations used is given in Table 4.1. A single absorber layer after the last silicon sensor was added in order to account for backscattering of particles as expected in the final detector.

This approach allowed the shower to be sampled up to the 10^{th} layer with a sampling resolution of one radiation length. The relative position of sensors S1–S3 in the first configuration was replicated by the S0–S2 sensors in the second one. The response of these sensors was expected to be the same in both configurations. This allowed to control the signal variation from one configuration to another.

Due to a malfunctioning of the FPGA on the readout board of S3 in the third configuration, only eight positions were used in the analysis. The data collected from all three configurations were combined in order to imitate the detector prototype consisting of nine active sensor layers.

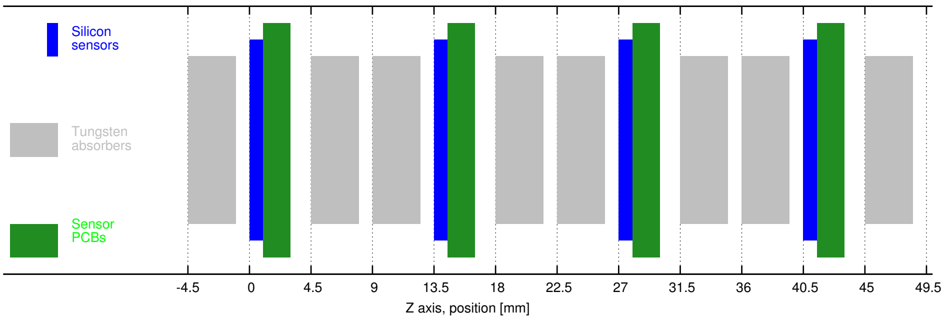

Figure 4.6: Geometry of the first configuration of the LumiCal detector prototype with active sensor layers and tungsten absorbers. The Y axis (perpendicular to Z) is not to scale.

	Radiation lengths in number of absorber layers									
Configuration	1	2	3	4	5	6	7	8	9	10
1	S0		S1		S2		S3			
2			S0		S1		S2		S3	
3				S0		S1		S2		S3

Table 4.1: Positions of active sensor layers in three configurations expressed in number of absorber layers (i.e. radiation lengths X_0 in absorber) in front of the sensor layer. S0–S3 stands for Sensor 0 – Sensor 3.

A closeup of the second configuration of the LumiCal stack can be seen in Fig. 4.7. The hood front panel was removed to enable the installation of two additional absorber layers to a total of three layers of absorber before the first LumiCal module (S0). The electronic board of the first LumiCal module, is visible above the absorber layers.

4.1.2 Telescope

To reconstruct the trajectories of beam particles, a four-plane tracking detectors, the so-called telescope, was used. The telescope was positioned upstream from the LumiCal. The distance between

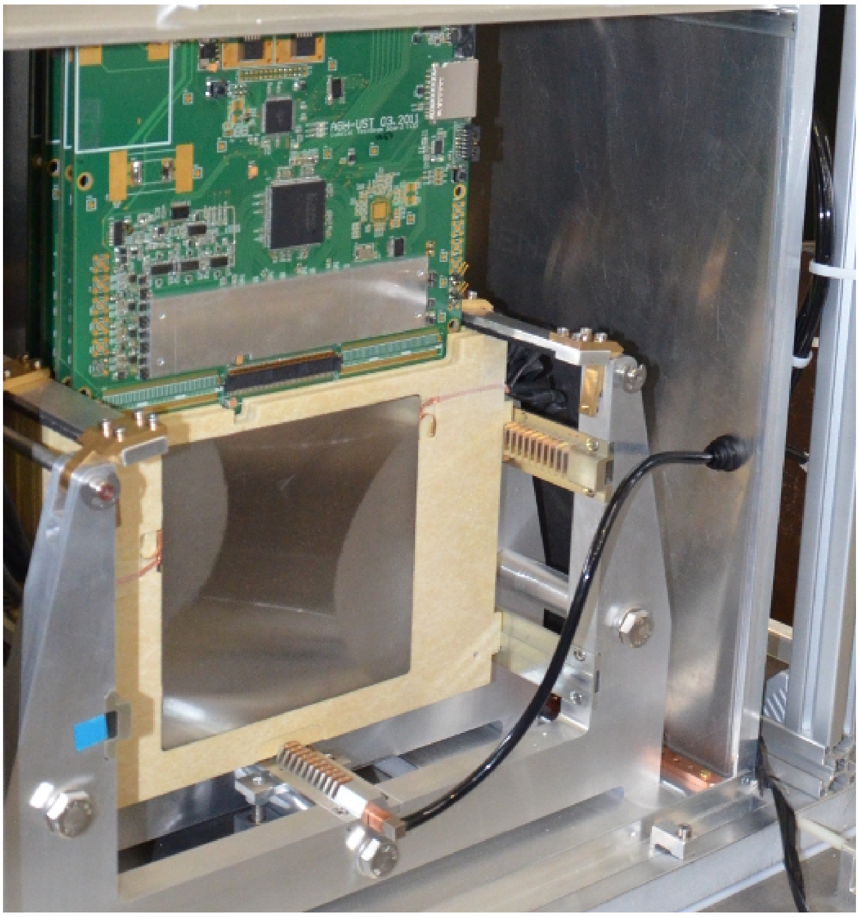

Figure 4.7: A closeup on the assembled LumiCal stack in the second configuration.

every two telescope planes was 20 cm, and the distance from the last plane to the first LumiCal sensor plane was 52 cm. The telescope is based on the MIMOSA-26 chip, a monolithic active pixel sensor with fast binary readout [73]. One MIMOSA-26 chip consists of 1152 × 576 pixels with 18.4 μm pitch, resulting in an active area of 21.2 × 10.6 mm^2. The binary readout accepts the pixel signals exceeding a preset discrimination level. The pixel matrix is read continuously providing a complete frame every 115.2 μs.

The data are triggered and stored by a custom DAQ system, based on the National Instrument PXI crate, developed by the Aarhus University in collaboration with the Strasbourg University. The telescope planes in aluminum boxes, each comprising one MIMOSA-26 chip, can be seen in Fig. 4.8.

4.1.3 Data acquisition and trigger

Two independent DAQ computers were used for the telescope and for the LumiCal, respectively. Figure 4.9 displays the connections and the flow of information in the system.

Three scintillation counters were used to provide a trigger for particles traversing the active part of

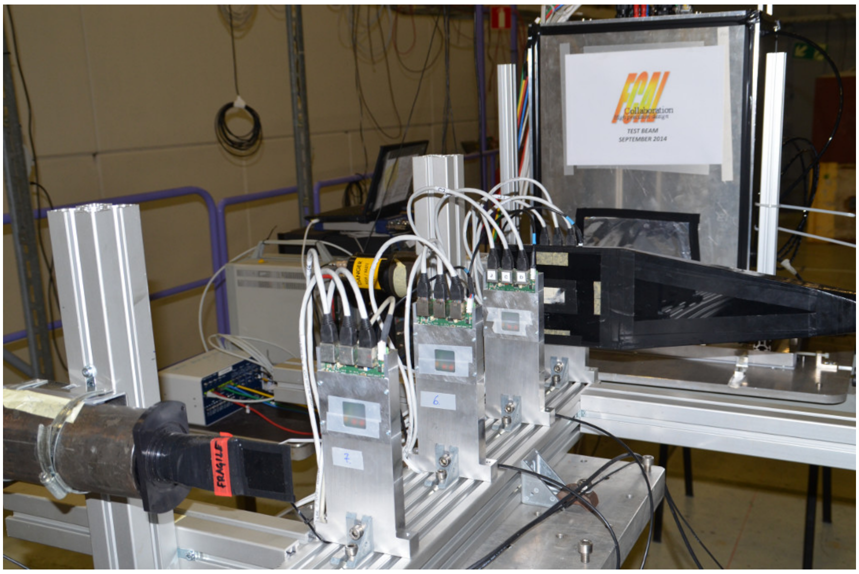

Figure 4.8: A closeup view of the telescope in the beam-test. Three of the telescope planes in aluminum enclosures are positioned on the beam path (from left to right). There is one trigger scintillator counter in front of the telescope and one behind the third telescope plane.

the telescope sensors and the region of the sensors in the calorimeter stack. Two 5×5 cm^2 scintillator tiles were placed upstream and downstream of the telescope and one, with a 9 mm diameter circular hole, was placed just in front of the last telescope plane, as shown in Figure 4.8. In order to ensure that triggers are only generated by beam particles in the sensitive area of the telescope, the signal from the hole-scintillator was set in anti-coincidence.

The trigger signal was combined with the Cherenkov counters response to create a trigger for leptons. A small fraction of particles passing through the active area of the anti-coincidence scintillator was not vetoed due to the inefficiency of the scintillator. In order to monitor and distribute the trigger signal correctly, a trigger logic unit (TLU) [74] was used. The TLU received the trigger signal and generated an integer TLU number, counting the number of triggers received. The TLU then passed on the trigger signal and the TLU number to the telescope and the LumiCal, respectively. In order to preserve the TLU number and the telescope frame number, a dedicated auxiliary (AUX) unit was used, saving these two numbers for the same event. The AUX unit was also responsible for delivering a long BUSY signal back to the TLU in order to veto triggers during the long readout time of the telescope. For each event, the TLU number from the LumiCal DAQ, the TLU number from the AUX and the telescope frame number from the AUX were stored to synchronize offline the LumiCal and the telescope data.

The number of accumulated events was determined by the spill structure of the beam, the rate capability of the telescope and the small electron content in the 5 GeV secondary beam. Of the 10^3–10^4 particles in the beam per 400 ms spill with about 2 spills per minute, only 5% were electrons. The trigger rate in the spill had to be limited, since the MIMOSA-26 chip of the telescope provides continuous readout. Otherwise, within the readout time of about 400 μs, a second particle could cross the telescope, and then the mapping to the electromagnetic shower would become ambiguous. In addition, the DAQ applied a veto against triggers during event data packing, thus rejecting some

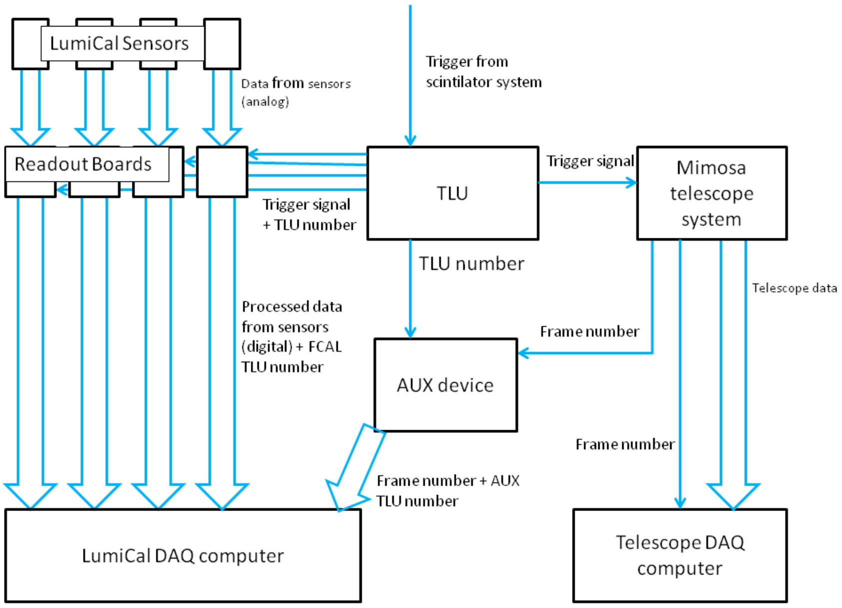

Figure 4.9: A schematics of the connections and the path of the signals in the system. Data flow is symbolized by a thick arrow, while simple bit information transfer (e.g. the trigger signal) is symbolized by a thin arrow.

of the valid electron triggers. Typically, an average rate of half an electron event per second were registered.

4.2 Data analysis

4.2.1 Telescope alignment and tracking

The raw information from each MIMOSA plane contains the pixels with deposited energy larger than the threshold set by the telescope DAQ. The MIMOSA plane is digital, in that no information on signal strength is available. In order to reconstruct tracks from the telescope raw data, a few steps are needed. First the raw data have to be extracted and a pixel cluster has to be identified. The hit coordinate is defined by the center-of-gravity of the pixel cluster. This was done using the standard procedure implemented in the telescope analysis framework (TAF) [75].

The distribution of hits from the last telescope plane is presented in Figure 4.10. The active area of the trigger, determined by the 9 mm hole-scintillator, is visible in Fig. 4.10(a), which shows a scatter plot of the Y versus X coordinates of the hits. However, in the hit distribution along the X direction, presented in Fig. 4.10(b), the active area is barely visible. This is due to a high level of noise registered in the MIMOSA plane originating from some light penetration that generates large number of clusters from pixels that are randomly fired.

As the positions of the telescope planes were only roughly set by the telescope mechanical support structure, an additional alignment was required to determine their relative position. After alignment, hits associated with a track were identified by the colinearity requirement between hits in the four telescope planes. These hits were used to calculate the track parameters. The track identification and

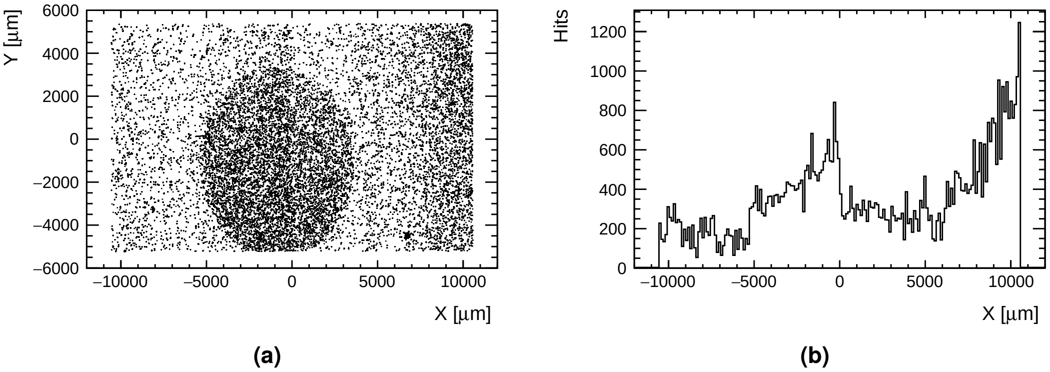

Figure 4.10: (a) Hit map from the last telescope plane, in the plane coordinate system, with the structure of the 9 mm hole in the second scintillator counter clearly seen. (b) Hit distribution along the plane X axis, where the same structure is seen distorted by a large number of noise hits from the light leak into the telescope plane.

reconstruction was carried out with the software supplied by Aarhus University. The distribution of hits that were associated with a reconstructed track is shown in Figure 4.11. Here the the active area of trigger is prominently visible, both in the Y-X scatter plot of the hits in Fig. 4.11(a) as well as in the hit distribution along the X direction in Fig. 4.11(b).

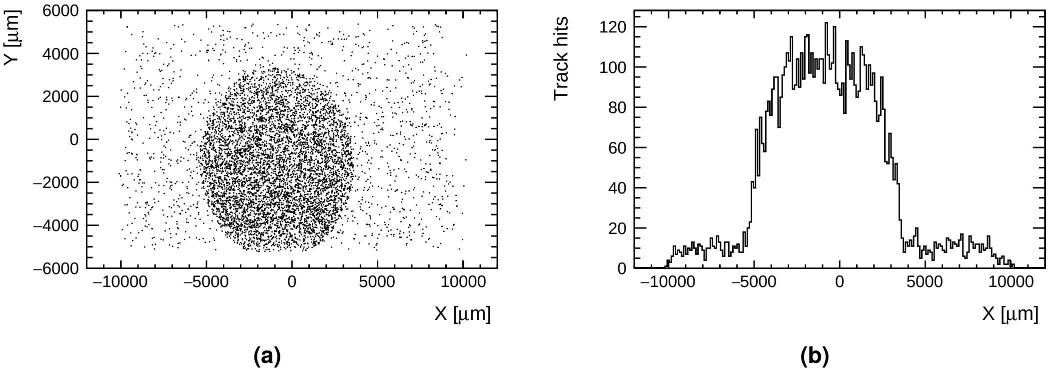

Figure 4.11: (a) Hit map from the last telescope plane, in the plane coordinate system, for hits that were associated with a reconstructed track; (b) the hit distribution along the plane X axis.

The track hit residual is defined by the difference, in each axis, between the reconstructed hit position of the track in a plane and the hit associated to that track in that plane. From the residuals distribution, the plane resolution can be estimated for each axis. Figure 4.12(a) presents, as an example, the hit residual distribution for the X and Y direction of plane number 3. The residuals in the X and Y plane behave the same way. A Gaussian fit to the residual distributions was performed leading to a root mean square (RMS) hit resolution of 8.9 μm (9.0 μm) [57] in the X (Y) direction.

As noted before the beam intensity had to be tuned by closing the collimators up to the point where, on average, there would be one reconstructed track in each trigger. Multiple track events cause two difficulties; first, in the association of a track hit with a track, and second, in the association of a track with the energy deposited in the calorimeter. Since the telescope recording time is 450 μs, much larger than the LumiCal's 1.6 μs, only the particle that generated the trigger will leave a record in the calorimeter. The distribution of the reconstructed tracks per event is shown in Fig. 4.12(b). The most probable value is one track per event and the average is slightly above one.

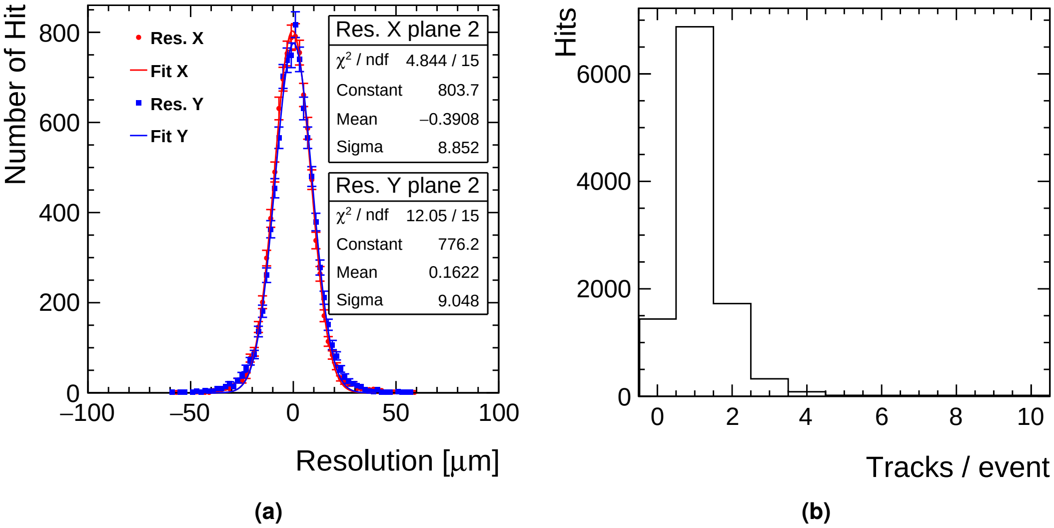

Figure 4.12: (a) The residuals distribution for the X and Y direction of plane 2 (symbols) fitted with a Gaussian distribution (lines). (b) The distribution of the number of reconstructed tracks per event.

The analysis of track angles and associated energy deposits in the LumiCal prototype showed that about 3% of all tracks result from noise hits in the telescope accidentally appearing within the colinearity tolerance criteria. These tracks are associated with LumiCal deposits close to zero. In addition, about 2% of all tracks can be attributed either to the inefficiency of the anti-coincidence scintillator or to noise tracks in the telescope associated accidentally to non-zero energy deposits in the prototype.

4.2.2 Data processing in the LumiCal detector

The ADC in each channel is running continuously at a sampling clock rate of 20 MHz. The recorded samples are stored in the on-board data buffer. That allows to control the number of the post- and pre-trigger samples in an event.

During the beam-test data taking, the number of pre-trigger samples was adjusted to the trigger arrival time such that the signal would arrive in the middle of the 32 samples window, as shown in Fig. 4.13 for two selected sets of eight channels. In the figure, the raw amplitude of each sampling is plotted as a function of the sampling time in each channel. A signal above threshold is observed in two of the channels.

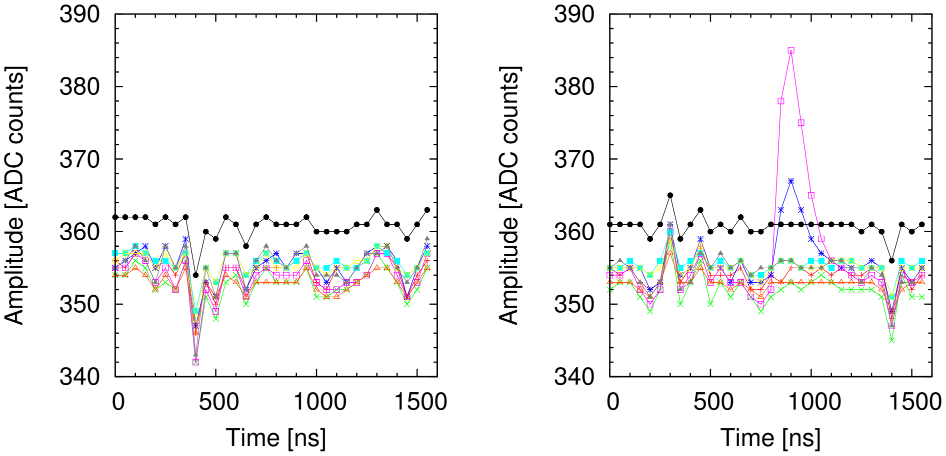

Figure 4.13: Raw amplitudes of two sets of 8 channels, drawn in different colors, as a function of time. One set (left) contains no signal and one (right) shows a signal in two channels (pink and blue).

4.2.2.1 Initial treatment of the data

As can be seen in Figure 4.13, the baseline for raw events has slightly different levels for each channel, but fluctuates as a function of time synchronously in all channels. This synchronous effect, denoted hereafter as common-mode noise, is presumably caused by power lines. The initial treatment of the data includes baseline and common-mode subtraction.

For each channel the baseline was calculated for every event by averaging the raw samples before the signal arrival time. The calculated average was subtracted from each sample, resulting in all channels fluctuating synchronously around zero. The common-mode noise was extracted by averaging each sample over all the channels in a chip. After the extraction, the common-mode noise was subtracted from each channel. After the baseline and common-mode subtraction, the raw event, presented in Figure 4.13, is transformed into the event shown in Figure 4.14.

4.2.2.2 Signal reconstruction by deconvolution

As noted in the beginning of Section 4.2.2, LumiCal signals were measured with the ADC ASICs, which sample the pulse with a frequency of 20 MHz. The LumiCal front-end electronics is designed for a synchronous reading mode, in order to best cope with the planned trigger-less operation of the ILC detectors. In this mode, the ADC clock is synchronized with the accelerator clock, ensuring that the detector signal evolves always at the same time within the recorded window.

During the beam-test, triggers appear randomly during the spill time window. In this case the ADC clock is running independently and the reading is in an asynchronous mode. In the asynchronous mode, the detector signal arrives at different times within the sampling window. Therefore, unless the ADC sampling frequency is much higher than the pulse shaping time, the ADC may not sample the pulse at the peak amplitude.

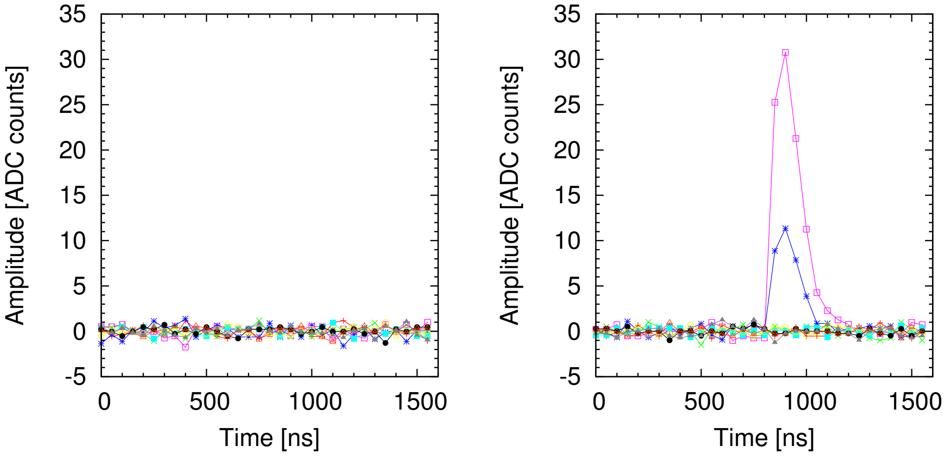

Figure 4.14: The amplitudes presented in Figure 4.13 after processing the raw LumiCal data.

Precise measurement of the pulse amplitude requires some processing of the measured samples. The simplest approach is to take the highest sample as an estimate of the pulse amplitude, but this will generate a negative bias or underestimate the amplitude. The method with the highest expected precision consists of fitting the sampled pulse shape with a pre-defined form. This method can be applied only during the offline analysis, and it is a rather slow procedure, which requires an initial guess of the fit parameters. In order to enable a fast amplitude reconstruction, a deconvolution method [76] was developed for the LumiCal readout. The advantage of this method is the possibility to implement it inside the digital signal processing block, significantly reducing the total amount of data transmitted from the detector.

Deconvolution is based on the idea that the pulse is a convolution of the sensor and the preamplifier-shaper chain responses. Since the pulse shape after the preamplifier-shaper chain is known, it can be inverted by deconvolution in order to reconstruct the pulse amplitude. For LumiCal, a simple semi-Gaussian response of the front-end $CR - RC$ shaper was implemented in order to reduce the complexity of the deconvolution filter [77]. The details of the deconvolution have been discussed elsewhere [66, 77]. The deconvolution method is utilized as a digital filter in the time-domain over the samples set of each event, and requires only two multiplications and three additions. The formulation of the deconvolution filter is detailed in Eq. (4.1) where the deconvoluted sample d_i is obtained as the weighted sum of the signal sample s_i and its two prior samples,

$$d_i = w_1 s_i + w_2 s_{i-1} + w_3 s_{i-2} \; . \tag{4.1}$$

Each weight depends on the sampling time T_{smp} and the shaping time constant τ. Denoting by x their ratio

$$x = \frac{T_{smp}}{\tau} \, , \tag{4.2}$$

the weights are determined as

$$w_1 = \frac{e^{x-1}}{x}, \quad w_2 = \frac{2e^{-1}}{x}, \quad w_3 = \frac{e^{-(x+3)}}{x} \, . \tag{4.3}$$

For the present system $T_{smp} = 50$ ns, and the shaping time-constant was estimated to be $\tau \approx 70$ ns [77] from the electronic test measurements.

For synchronous reading, the deconvolution filter provides exactly one non-zero sample value, directly proportional to the amplitude of the original signal. During the asynchronous reading, the filter may provide up to two consecutive non-zero sample values, with their ratio depending only on the sampling and shaping time-constants, and on the pulse arrival-time t. The pulse arrival-time can be derived from Eq. (4.4) in units of the sampling time constant, T_{smp},

$$t = \frac{\frac{d_2}{d_1}}{\frac{d_2}{d_1} + e^{-\frac{T_{smp}}{\tau}}} . \tag{4.4}$$

The sum of the two non-zero sample values is directly proportional to the original signal amplitude, A, but acquires a small dependence on the pulse arrival-time, t, as can be deduced from Eq. (4.5),

$$A = (d_1 + d_2)\frac{\tau e^{-\frac{T_{smp}(t-1)+\tau}{\tau}}}{T_{smp}(1 - t(1 - e^{-\frac{T_{smp}}{\tau}})} . \tag{4.5}$$

In this analysis, the deconvolution filter was applied indirectly by selecting two consecutive highest sample values in the range of $16 \leqslant i \leqslant 18$, where the signal peak is expected (see Fig. 4.15), and applying equations Eq. (4.4) and Eq. (4.5). The two samples were used only if both were above a cut of three times the noise level estimated from the first 15 samples for each event and channel. In case that only one sample was found above the noise cut, it was assumed that the arrival time was synchronized with the ADC clock and the sample value was treated as the amplitude.

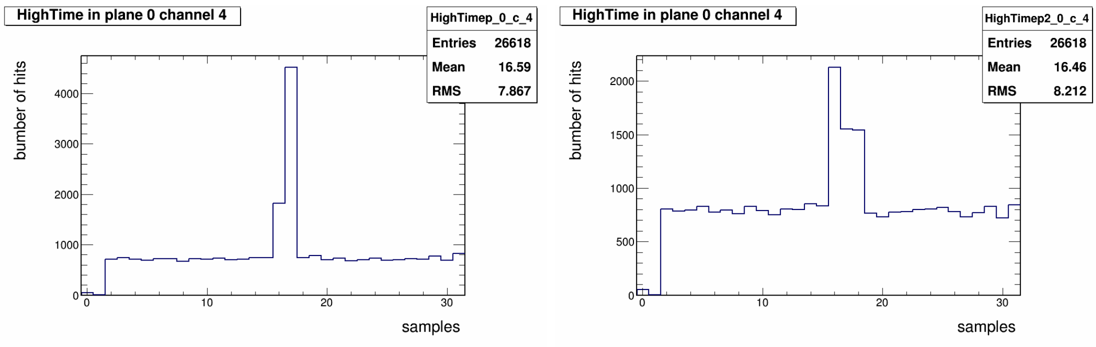

Figure 4.15: Distribution of the highest sample in an event.

After the initial treatment and deconvolution, the signals in the four planes of an electron event in configuration 1 are shown as an example in Figure 4.16.

4.2.2.3 Synchronization

The acquired data from the beam-test was saved in two different files, one that contained the LumiCal data and the other one that collected the information coming from the telescope. Synchronization between the different parts of the event is a key step in the analysis. Each system from the two DAQ

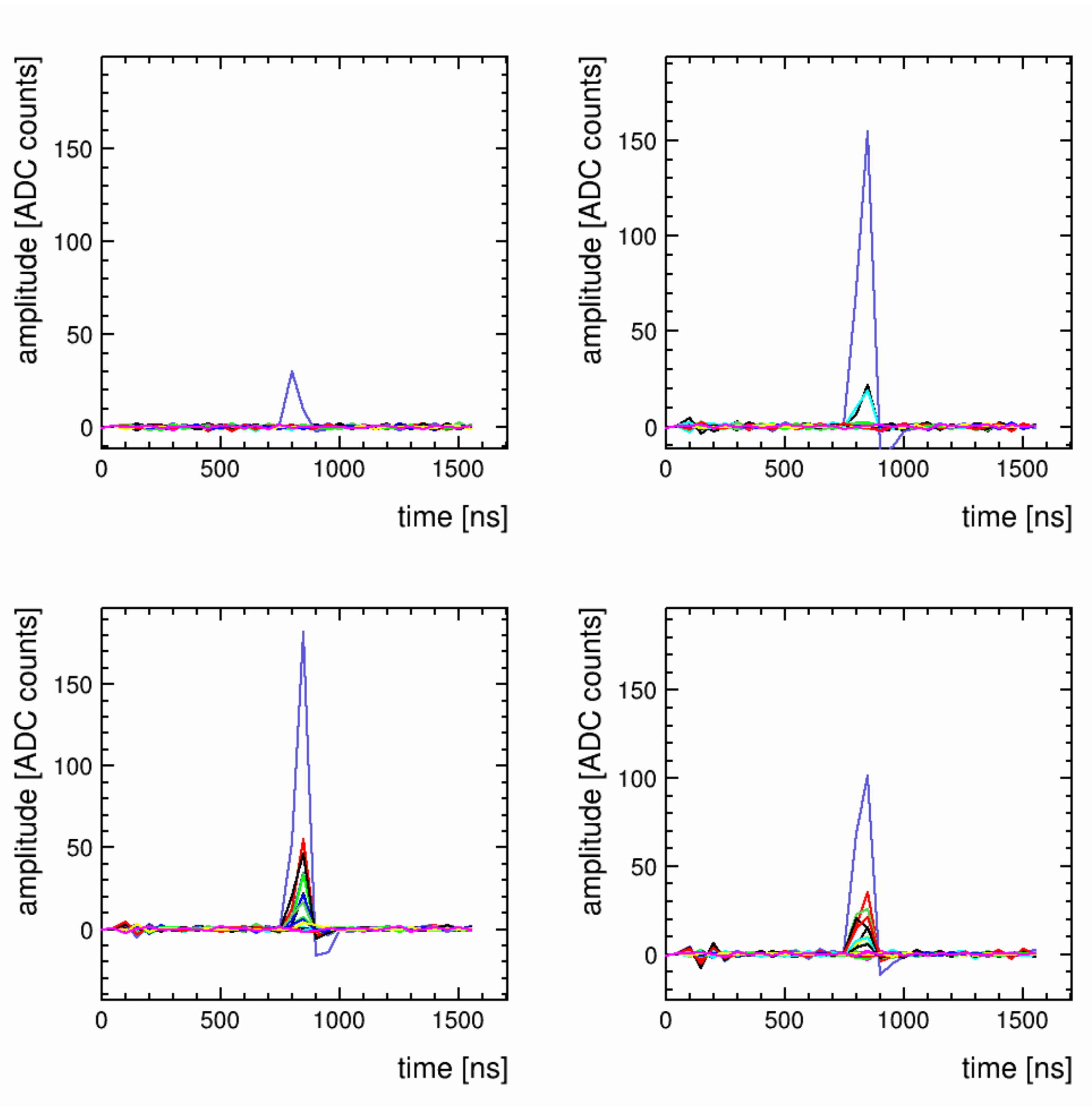

Figure 4.16: The amplitudes as a function of time in the 32 channels of an electron event after processing the signal in plane 1 (upper left), plane 2 (upper right), plane 3 (lower left) and plane 4 (lower right).

systems has its own synchronization method. LumiCal electronic boards were working within the EUDAQ system and were synchronized by the TLU. During each trigger, each board clocked out the TLU number directly from the TLU and saved it to the file. In the telescope DAQ, an internal number, called frame number, was used for synchronization between the four telescope planes. The AUX device was used to register both numbers for each event and to embed them into the LumiCal file. By matching these numbers between the two files, the full information for an event could be recovered. In case one of the numbers was missing in one of the systems, the event was skipped. Only complete events were used for the analysis. This procedure also coped with differences in the number of events coming from the initialization sequence of the complete DAQ system. In order to minimize problems that come from tracking inaccuracy/inefficiency, only events with a single track in the telescope which passed the track selection criteria were considered in the data synchronization process.

To ensure that the synchronization procedure is successful, hit maps like Fig. 4.17 can be studied. Each space point in Fig. 4.17 represents the expected hit position of the extrapolated telescope track to the first layer of LumiCal. The points create a cluster similar in size and shape to the circular 9 mm hole-scintillator in the trigger system that limited the beam size. Each point was assigned a color according to the channel number in the first layer of LumiCal which had a signal higher than the threshold of three times the noise level. The structure of the sensor is well reproduced, indicating that the assignment of the telescope information to a LumiCal event is correct.

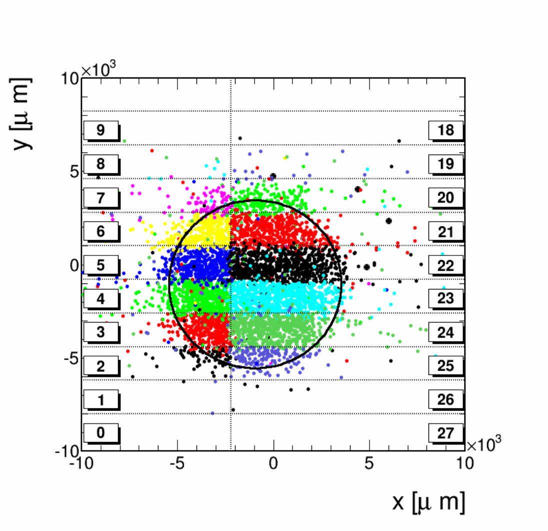

Figure 4.17: Expected position of the extrapolated telescope track in the first LumiCal sensor layer coded with a color determined by the channel number with a hit above threshold in the LumiCal.

4.2.2.4 Electron-muon separation

The T9 secondary beam contains a mixture of particles, thus the trigger system included the response of the two Cherenkov counters, as noted in Section 4.1.3. The Cherenkov counters response was adjusted by changing the gas pressure to create a trigger for both electrons and muons. Both are needed in the tests, electrons for the study of the electromagnetic shower, and muons for calibration and alignment. Because the trigger rate was very low, the Cherenkov counters in the trigger were setup such that the separation between electrons and muons was not possible, and that allowed to collect electron and muon data at the same time, saving run time.

The simplest method for electron/muon separation in the LumiCal data is by observing the total energy response of the calorimeter. Electrons will create an electromagnetic shower and will deposit, in total, a significant part of their energy, while muons in this energy range will act as MIP through all sensor and absorber layers, and will thus deposit only a small amount of energy. Figure 4.18 shows the raw energy spectrum for a beam containing electrons and muons, obtained as the sum of all the 128 channels in the stack for each event.

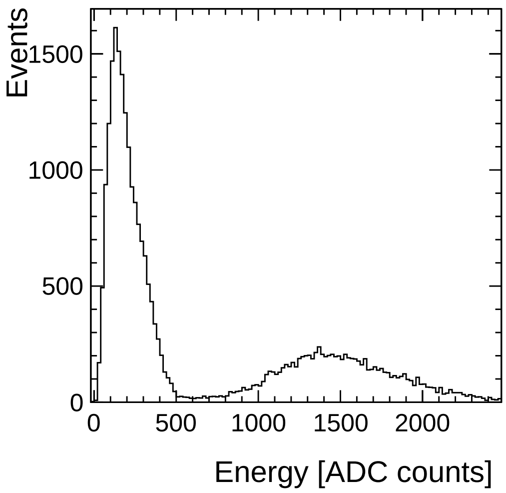

Figure 4.18: Energy distribution in the LumiCal for a beam comprising electrons and muons.

The narrow peak around 120 counts corresponds to the expectations for a muon of 5 GeV and is hence considered as originating from the muons in the beam. It is well separated from the wide distribution expected for electrons. Based on the distribution in Figure 4.18 a threshold of 550 ADC counts was chosen to separate electron from muon events.

4.2.2.5 Calibration with Muons

The signal amplitude represents the amount of energy deposited in a pad. So far, the signal amplitude was presented in arbitrary units of ADC counts. In order to measure energy, the signal amplitude must be converted to an energy scale. It is an essential step, especially since LumiCal front-end ASICs have two different amplification technologies with different gain in each chip.

For the energy calibration, the sensor response to muons is used. A convolution of a Gaussian and a Landau distribution is fitted to the measured spectra, as can be seen in Fig. 4.19. The most probable value (MPV) of the Landau distribution is used for the calibration. The MPV was defined as one unit of minimum ionizing particle, MIP.

The energy calibration should be implemented for each channel, since individual channels may differ in their response. Two limitations in the 2014 test prevented the calibration of individual channels. As can be seen in Fig. 4.17, the projected trigger area on the LumiCal sensors covers only several (order of 10) pads out of the 32 pads, in each layer. Since muons in the beam are confined to the projected trigger area, most of the pads will not contain a muon signal for calibration. In addition, the low statistics collected due to the beam condition created difficulties to perform separate fits even for the channels from the trigger area. Instead, the channels inside the trigger area, in each layer, were divided into two groups according to their amplification technology. Thus, two muon spectra were collected for each layer, and two gain constants were extracted and used to scale all energy measurements. An example of the two spectra from one layer can be seen in Fig. 4.19. The differences between the gains obtained from the two technologies can be clearly observed, where channels with MOS feedback (Fig. 4.19(a)) have about half the gain of the R feedback (Fig. 4.19(b)).

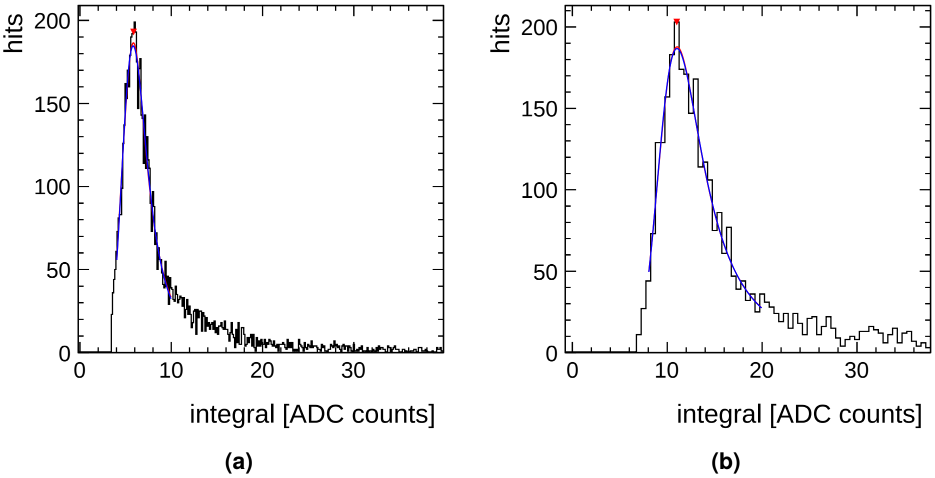

Figure 4.19: Example of two spectra from one layer, channels with (a) MOS feedback and (b) R feedback. The horizontal axis represent the sum of amplitudes in the event, in units of ADC counts.

4.2.3 Simulation

The beam-test setup was simulated using LUCAS [78], the LumiCal simulation program. LUCAS is a C++ object-oriented toolkit, based on GEANT4 [79] and ROOT [80]. It was derived from the code written for the ILD detector software package Mokka [81]. In the simulation, the standard QGSP_BERT [82] physics list with the GEANT4 range cut-off of 5 μm is used.

The implementation of the LumiCal module includes the silicon sensor, the PCB sensor board with its metalization layer, and the Kapton fanout with the copper traces. The silicon sensor is implemented as a sensitive area of arc shape with the sensor dimensions. The sensor is subdivided into software implemented virtual cells, to save computation time, and does not include inactive areas such as the edges and gaps between pads. The total energy deposited within a virtual cell constitutes the simulated response of the pad.

The beam was simulated as coming from the telescope area, one meter away from the LumiCal stack of square shape with an area of $7.6 \times 7.6\,\text{mm}^2$. The middle of the square was shifted so that the ratio of hits between the two connected sectors would agree with the ratio observed in the data. The track angular distribution was generated such that the distribution of the track projection on the X and Y axes reproduced the T9 beam characteristics with an RMS of 0.6 mrad. Similar to the data hit-map in Fig. 4.17, the extrapolated hit position on the LumiCal front layer from the simulated tracks is presented in Figure 4.20(a). A color was assigned to each hit, corresponding to the pad where the energy was deposited. For each of the three configurations used in the test, the specific layer arrangement was reproduced in the simulation. Sets of 10^4, 5 GeV electrons and muons were simulated for each configuration. In order to use the same energy scale in both data and simulation,

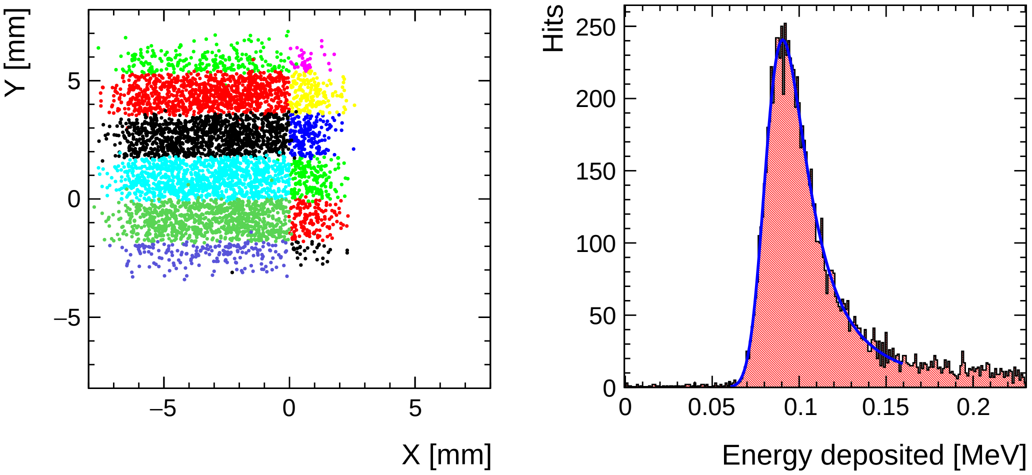

(a) **(b)**

Figure 4.20: In the simulation, distribution of the extrapolated hit position in the first layer of LumiCal, with a color code determined by the pad number where the energy was deposited.

the response for muons was used. A distribution of the simulated sensor responses to 5 GeV muons is presented in Fig. 4.20(b). The MPV of the Gaussian and Landau convolution fit to the distribution of the muon energy deposits yielded a value of 88.5 keV and was defined as one MIP.

4.3 Results

4.3.1 Electromagnetic shower

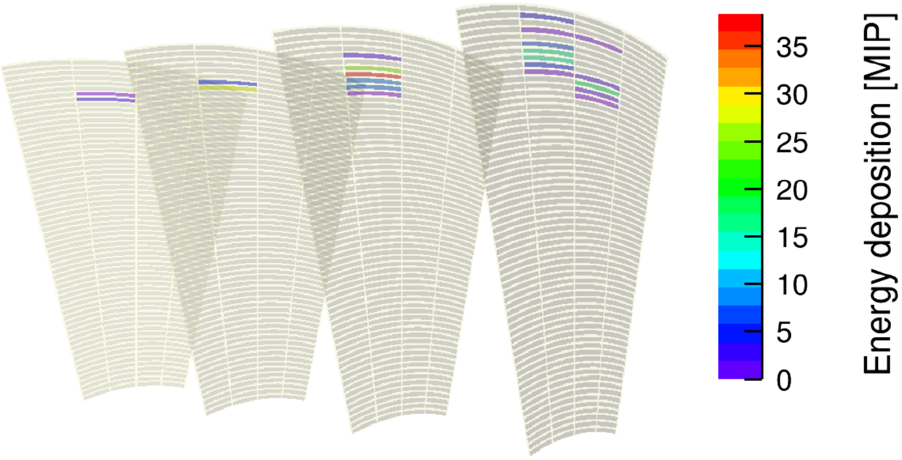

Figure 4.21: Visualization of a full event after processing.

A visualization of one full event after processing is presented in Fig. 4.21. The energy deposition in each pad in each layer is represented by the color assigned to that pad; the dominant gray color represents pads without signal. The event presented in this figure demonstrates quite well the development of the electromagnetic shower. When the electromagnetic shower evolves along the longitudinal Z direction of the calorimeter, more and more pads have energy deposits. In addition these deposits increase with the depth of the shower and spread over larger distances transverse to the shower path in the calorimeter. The event exemplifies the stochastic nature of the electromagnetic shower development.

In order to analyze the longitudinal development of the electromagnetic shower, the distribution of the sum of the deposited energy per layer is used. Examples of energy distribution in a few selected layers, in units of MIP, are shown in Figure 4.22. From the first configuration, in which the first sensor layer was placed after one absorber, the energy sum distribution of this first layer is presented in Figure 4.22(a). From the second configuration, where the first sensor layer was placed after three absorber layers, the distribution of the deposited energy in layer 5 is shown in Figure 4.22(b) and for layer 9 in Figure 4.22(d). In Figure 4.22(c) layer 6 is shown from the third configuration, where the first layer was placed after four absorber layers. In all four cases, the simulation is also shown and agrees well with the measurements.

The uncertainty is dominated by a 5% calibration uncertainty [77], based on the analysis of the signal spread, channel by channel, obtained with a test pulse. This was applied to the average energy measured in six of the nine layers. However, since layers number 3, 5 and 7 were sampled in both configurations 1 and 2, the uncorrelated uncertainties were reduced by $\sqrt{2}$. Systematic uncertainties in the simulation originate from the measurement uncertainties of the plate thicknesses, which are estimated using local derivatives of the shape, as done in Ref. [83]. They are progressively higher towards the last layers, reaching 2% in the 9^{th} layer.

The longitudinal development of electron showers is shown in Figure 4.23(a) in terms of average shower energy deposits per plane as a function of the number of absorber layers in front of the plane. In Figure 4.23(b) the shower development determined for each of the three layer configurations is presented, with each color representing a different configuration. Here the same layers in different configurations can be compared and are found to be in good agreement with each other. The results were compared with the prediction of the simulation, and agreement between the simulation and the data is found within the quoted uncertainties (not shown for the simulation). The shower maximum is observed after 6 radiation lengths. The difference in layer one, where the simulated deposition is slightly smaller than that observed in the data, is understood as due to preshowering caused by upstream elements not included in the simulation.

4.3.2 Resolution of the position reconstruction

The silicon sensor segmentation has a pitch of 1.8 mm in its radial direction (pad), as shown in Figure 4.4, and, at the location of the beam spot, an arc length in the azimuthal direction of 2.5 cm with a sagitta of 0.4 mm. For further considerations, it is convenient to use a Cartesian coordinate system in the transverse plane with the origin coinciding with the shower axis, the Z axis, and the Y axis running along the radial direction of the LumiCal sensor. In the following, unless stated otherwise, the arc shape of the pads will be approximated by strips.

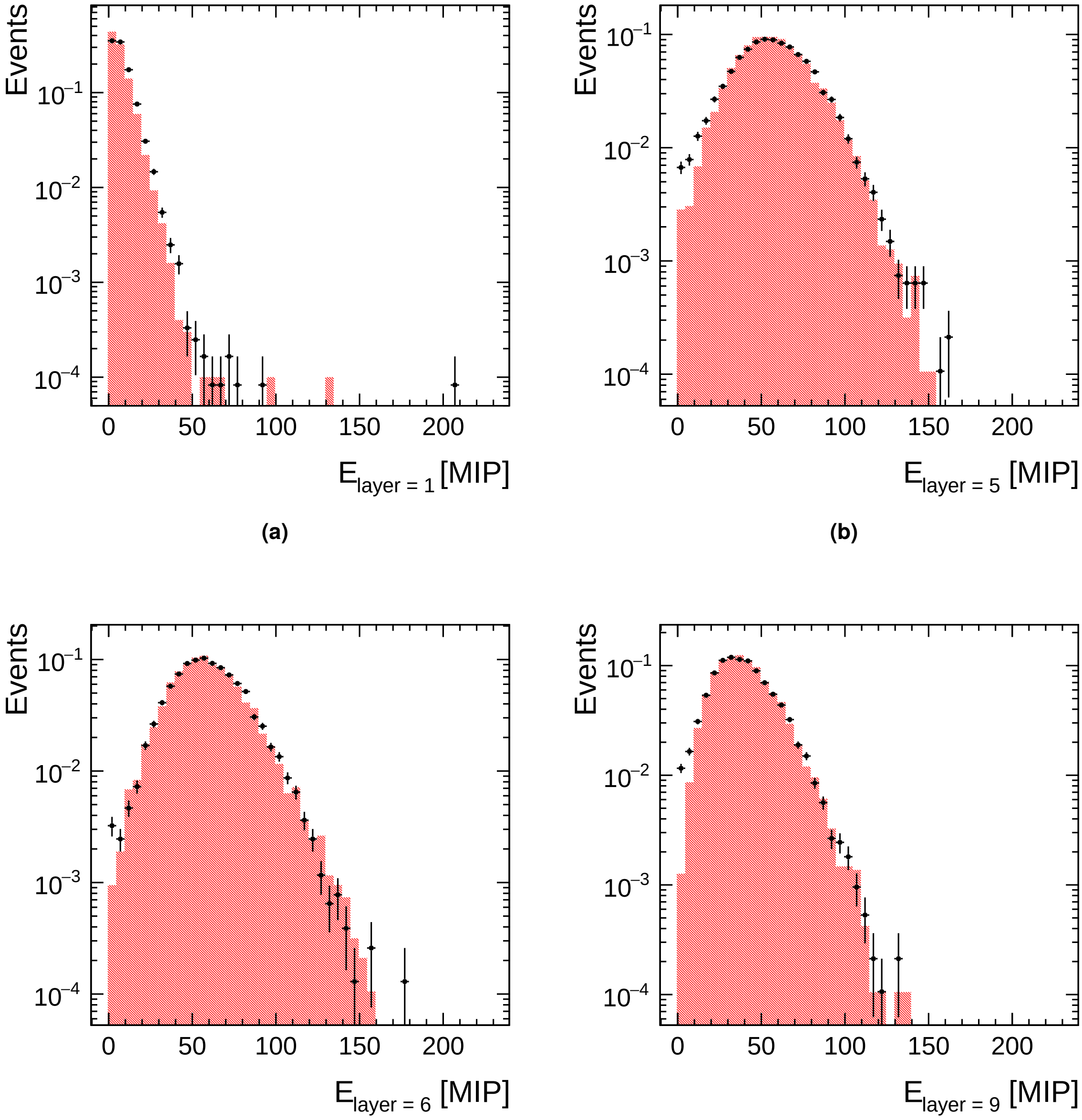

(a) (b)

(c) (d)

Figure 4.22: Distribution of the energy sum per layer, E_{layer}, in units of MIP, for (a) layers 1 from configuration 1, (b) layers 5 from configuration 2, (c) layer 6 from configuration 3 and (d) layer 9 from configuration 2. The data (dots) are compared to the simulation (shaded region).

Denoting E_{nkl} as the energy deposited in the sensor pad for layer l, sector k and radial pad index n, the one-dimensional deposited energy distribution for one event along the Y axis can be obtained from the following sum:

$$E_n = \sum_{k,l} E_{nkl}\,, \tag{4.6}$$

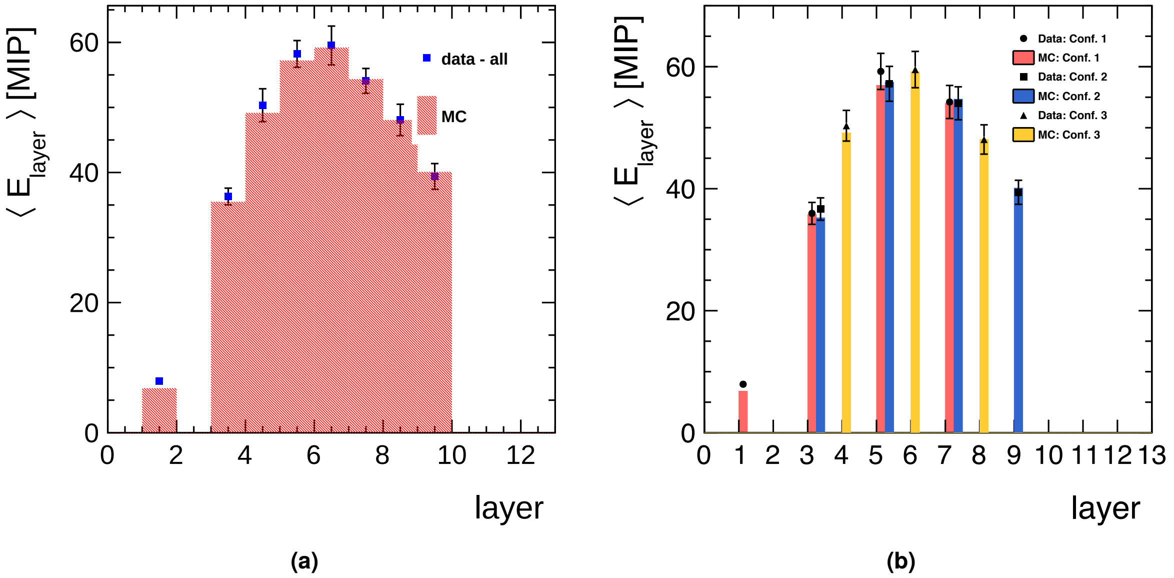

Figure 4.23: Average energy deposited in the detector planes of the LumiCal prototype as a function of the number of tungsten absorber layers for three configurations (a) combined and (b) separately. The dots (squares and triangles) are data and the shaded area corresponds to the simulation.

where the layer index l runs over all sensitive planes in the stack, from 1 to 4, and the sector index k runs from 1 to 2, for the two sectors connected to the readout electronics. All pads with the same index, are summed over the layers to form a tower. The energy deposited in a tower of pads with index n is denoted by E_n. An example of the E_n distribution for a single event is shown in Figure 4.24. The position of the beginning of the shower on the surface of the first layer projected onto the radial coordinate, Y, can be estimated as the mean of the Gaussian fitted to the E_n distribution.

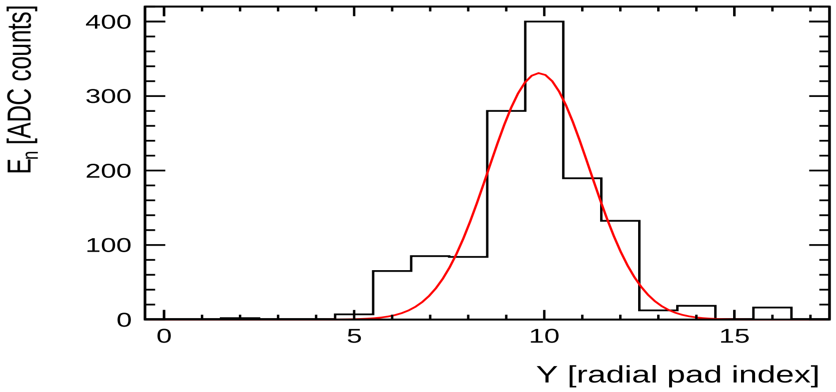

Figure 4.24: The deposited energy sum for a single event, E_n, as a function of Y expressed in terms of the pad number n. The curve is the result of a Gaussian fit to the data.

The distribution of the radial shower position Y is shown in Figure 4.25. Most of the estimated shower positions are in the radial pads within the trigger area which spreads over 10 mm. For comparison, the distribution of the extrapolated radial hit position from the beam telescope track is also presented. The two distributions, which correspond to the beam profile, are in good agreement with each other.

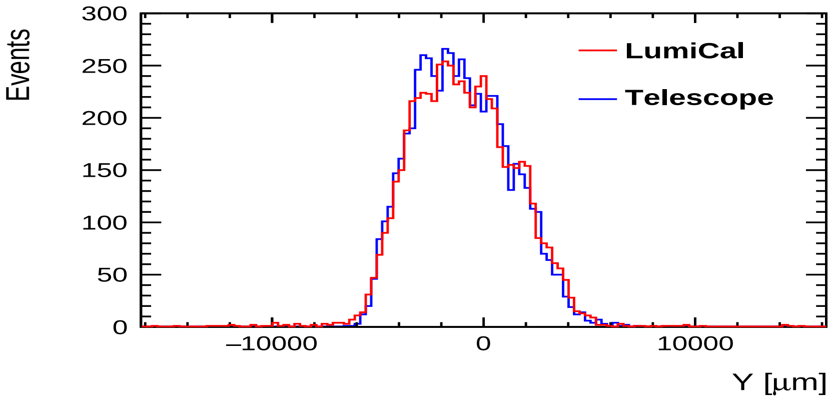

Figure 4.25: The distribution of the radial shower position Y (red line) and the radial hit position reconstructed from the beam telescope data (blue line). For ease of comparison, the two distributions are slightly shifted with respect to each other.

For each event, the reconstructed position of the shower in the radial direction is compared with the extrapolated track impact point position provided by the telescope. The distribution of the difference in the Y coordinate, ΔY, together with the Gaussian fit, are shown in Figure 4.26. Since the telescope position resolution is much better than that of the LumiCal, the resolution of the latter is obtained from the standard deviation of the fit of 505 ± 10 μm. This number is the result of multiple scattering and statistical fluctuations in the shower development, and is in rough agreement with the obtained from the simulation, which predicts a resolution of 480 ± 10 μm.

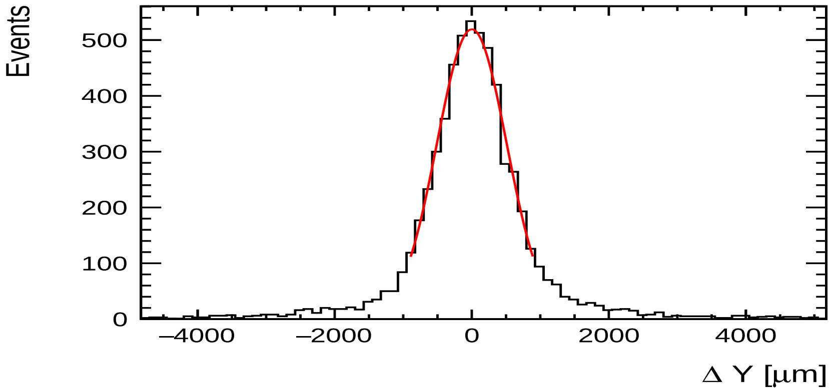

Figure 4.26: The distribution of the residuals between the reconstructed and the predicted position of the showering particle, ΔY. The curve represents the Gaussian fit to the distribution.

4.3.3 Effective Moliére radius

The Molière radius, $R_{\mathcal{M}}$, is a characteristic constant of a material giving the scale of the transverse dimension of the fully contained electromagnetic shower initiated by an incident high energy electron or photon. By definition, it is the radius of a cylinder with axis coinciding with the shower axis, containing on average 90% of the energy deposition of the shower. Since the shower measured in the beam-test is not contained, the measurements describe here and in the next chapter are measurements of the the effective Moliére radius[1] of the prototype.

4.3.3.1 Calculation of the effective Molière radius

The Molière radius, $R_{\mathcal{M}}$, is given by [84]

$$R_{\mathcal{M}} = X_0 \frac{E_s}{E_c} , \tag{4.7}$$

where the multiple-scattering energy $E_s = 21$ MeV, E_c is the critical energy [85], and X_0 is the radiation length of the material. For a composite material or a construction like the LumiCal prototype used in this beam test, the Molière radius can be obtained [84] as follows:

$$\frac{1}{R_{\mathcal{M}}} = \frac{1}{E_s} \sum \frac{w_j E_{cj}}{X_{0j}} = \sum \frac{w_j}{R_{\mathcal{M}j}} , \tag{4.8}$$

where j runs over elements composing the material or the setup, w_j is the mass fraction of element j and $R_{\mathcal{M}j}$ is its Molière radius.

Other than the absorber plates composed of two different tungsten alloys described in section Section 4.1.1, the stack contains also materials like the silicon sensors, the PCB and air. The Molière radii calculated using formula (4.8) for the absorber plates are presented in Table 4.2. The table also contains the data for the other materials of the stack. The total thickness of each material in the stack for different configurations used during the beam-test and the calculated Molière radii, using Eq. (4.8), are presented in Table 4.3.

material	W	Cu	Ni	W-95	W-93	Air	Si	PCB
density $[g/cm^3]$	19.3	8.96	8.9	18.0*	17.8*	0.0012	2.33	1.7
$R_{\mathcal{M}}[g/cm^2]$	18.0	14.0	13.4	17.7**	17.6**	8.8	11.5	10.3
$R_{\mathcal{M}}[mm]$	9.3	15.7	15.1	9.8	9.9	73300	49.4	60.6

Table 4.2: Summary of all the materials used in the stack setup with their density and Molière radii. Values marked with a star are taken from the manufacturer data sheet, while those marked with a double-star are calculated based on the material properties and weight fractions.

It is important for the LumiCal operation to achieve the smallest possible transverse size of the electromagnetic shower. The shower of single high energy electrons has to be reconstructed on a

---

[1] For simplicity, the term Molière radius is sometimes used in the text without the "effective" qualifier, but in all instances the effective Molière radius is implied unless stated otherwise

Configuration	W-93	W-95	Air	Si	PCB	Total	$R_M[cm]$
1	10.5	17.5	15.7	1.28	10.0	55.0	1.81
2	17.5	17.5	17.7	1.28	10.0	64.0	1.71
3	21.0	17.5	18.7	1.28	10.0	68.5	1.67

Table 4.3: Summary of the total thickness in mm along the Z axis of the different components in the stack, for the different configurations and the corresponding Molière radius.

widely spread background from beamstrahlung and two-photon processes. A small Molière radius facilitates this reconstruction, minimizes the energy bias and extends the range in the polar angle for high performance shower reconstruction [48]. In the stack used in this beam-test, the main contribution to the increase of the transverse size of the shower comes from the air gaps between the layers. This is also illustrated in Figure 4.27 which shows the Molière radius as a function of the gap size between tungsten plates of $1X_0$ thickness.

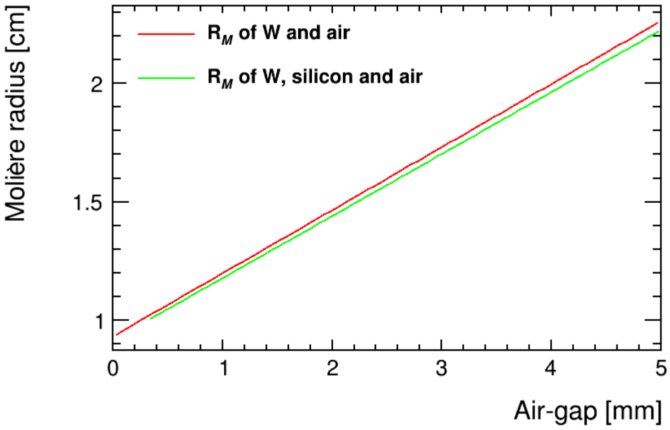

Figure 4.27: The Molière radius of a stack of $1X_0$ tungsten absorber plates as a function of the air-gap between them.

4.3.3.2 The Molière radius measurement principle

For an average energy density function $F_E^V(Z, r, \varphi)$, with V denoting volume, the total average energy is

$$E_{total} = \int F_E^V(Z, r, \varphi)dV = \int F_E^V(Z, r, \varphi)dZd\varphi rdr \; . \tag{4.9}$$

Assuming that the average energy density function has a radial symmetry, the expected energy per pad tower is obtained by integration along Z,

$$\int F_E^V(Z, r)dZ = F_E(r) \; . \tag{4.10}$$

As noted before, on average, only 10% of the deposited energy lies outside the cylinder with a radius of one $R_{\mathcal{M}}$,

$$0.9 = \frac{E_{r<R_{\mathcal{M}}}}{E_{total}} = \frac{\int_0^{2\pi} d\varphi \int_0^{R_{\mathcal{M}}} F_E(r) r dr}{\int_0^{2\pi} d\varphi \int_0^{\infty} F_E(r) r dr} \; . \tag{4.11}$$

The LumiCal pads are long (strip like) and act like 1D integrators making it impossible to directly access the form of $F_E(r)$. Neglecting the sagitta of the pads, the energy density in the Y direction can be expressed as

$$G_E(Y) = \int_{X_{min}}^{X_{max}} F_E(\sqrt{X^2 + Y^2}) dX \; . \tag{4.12}$$

Assuming a parameterized form of $F_E(r)$, its parameters can be recuperated by performing a fit to $G_E(Y)$. Depending on the form of the trial function $F_E(r)$, the integrations (Eq. (4.11) and Eq. (4.12)) can be performed either analytically or numerically.

4.3.3.3 Energy distribution in the transverse plane

In order to construct the average transverse distribution of the deposited energy, the distribution E_n for each event, as shown in Figure 4.24, had to be shifted to the same origin. This accounts for the fact that the incoming beam had a spread, as was presented in Fig. 4.25. The origin was set to be the center of the middle radial pad of the instrumented area. The extrapolated hit position in LumiCal from the reconstructed track in the beam telescope was used for the shifting of the data in the Y direction, while in the simulation the track information was used. Then the average values of E_n for each n, $< E_n >$, were calculated. To express the fact that the pad index was shifted to a new value, the shifted pad index will be denoted by m. The index $m = 0$ is assigned to the central core of the shower and ranges from -10 to +10 units of pads.

The extrapolated hit position on the face of the LumiCal was also used to determine where in the pad (in the Y direction) the shower started. Only events for which the shower started within 600 μm of the pad center were used. In addition, the difference between the extrapolated hit position in LumiCal and the position reconstructed from the LumiCal information, was required to be smaller than 2 pads (3.6 mm).

An example of the energy distributions for the shower core (m=0) and for that in the wings for pads m=3 and m=-5 is shown in Figure 4.28. The data are compared to the simulation. The shape of the distribution for m=3 and m=-5 is very well reproduced. The core distribution (m=0) in the data is slightly wider and shifted, most probably due to calibration and misidentified core position. However, the mean values of the measured and simulated distributions, used for the calculation, are in agreement.

For calculating the uncertainty on the average energy of a given tower, the correlation between towers was checked. The energy of different towers could be correlated through the systematic uncertainty from the energy calibration for each layer. The correlation factor , $\rho_{m,m'}$, between all tower pairs was calculated according to Eq. (4.13), from the average of the deposited energy distribution E_m

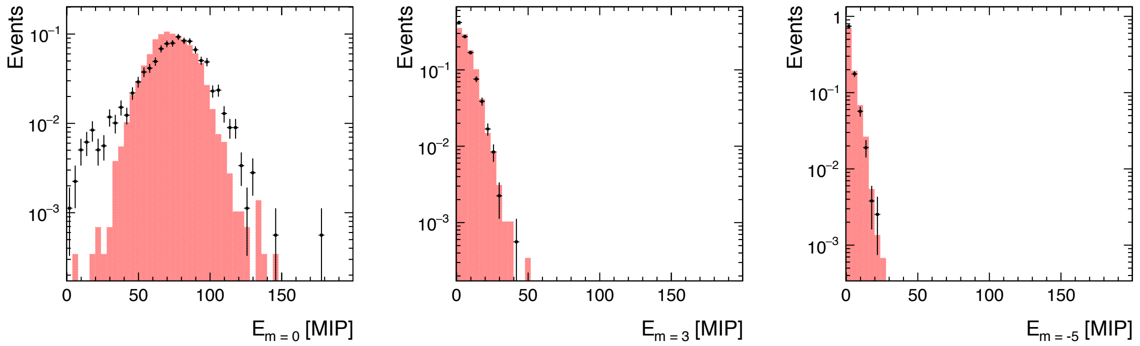

(a) **(b)** **(c)**

Figure 4.28: Sum of the deposited energy distribution from configuration 2, in units of MIP, for the radial pads with index $m = 0$, 3 and -5 from the shower core in (a) (b) and (c), respectively. The data (dots) are compared to the simulation (shaded area).

(example of which was shown in Fig. 4.28), and the average of the distribution of towers energy product $E_m E_{m'}$.

$$\begin{aligned}\rho_{m,m'} &= \frac{< E_m E_{m'} > - < E_m >< E_{m'} >}{\sigma_m \sigma_{m'}} \\ \sigma_m &= \sqrt{< E_m E_m > - < E_m >< E_m >}\end{aligned} \tag{4.13}$$

The correlation between towers was calculated for both simulation and data for every configuration used. An example of the correlation maps of configuration 2 for both simulation and data is presented in Fig. 4.29. The maps show the correlation factor for each tower pair, where m and m' represent the distance, d_{core}, in pad units from the shower core ($m = 0$). Both data and simulations indicate similar pattern for each configuration and the correlation coefficients overall are small. The conclusion is that the stochastic nature of the electromagnetic shower pretty much destroys the correlation introduced by the energy calibration.

The correlation coefficients are small enough to be neglected and the energy deposits in the towers can be treated as uncorrelated. Thus the uncertainty of each tower consists of the statistical uncertainty and the 5% systematic uncertainty from the energy calibration from each layer, added in quadrature. Figure 4.30 summarizes the contribution of the systematic and statistical uncertainties from all layers in configuration 2 to the overall uncertainty in each tower.

4.3.3.4 Functional form

The distribution of the average deposited energy in the transverse plane is symmetric with respect to the longitudinal shower axis and does not depend on the azimuthal angle. Its radial dependence

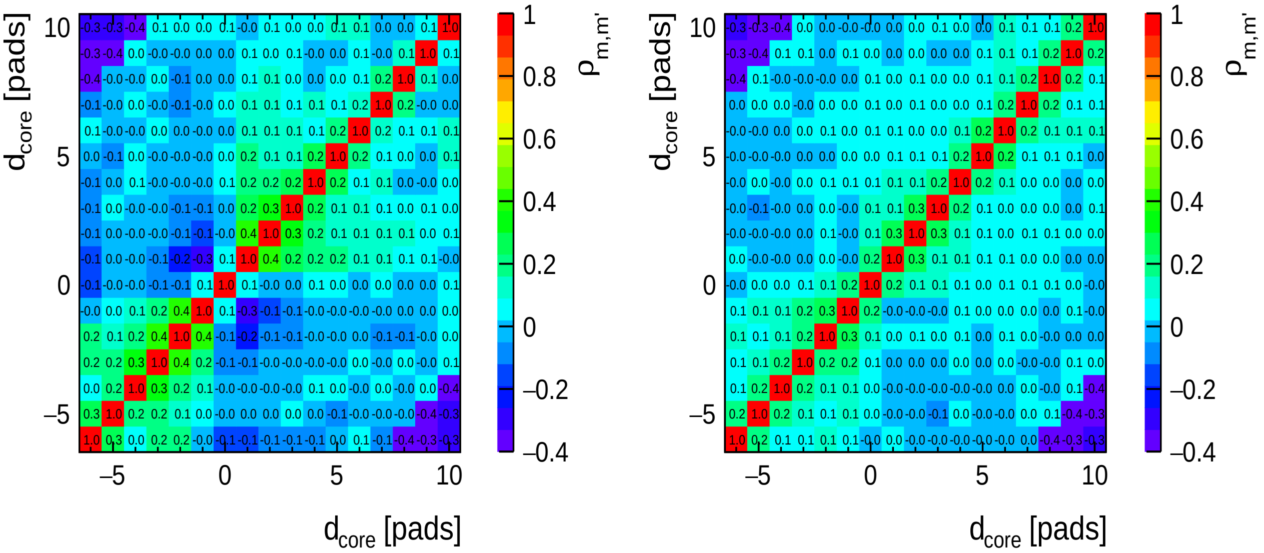

(a) **(b)**

Figure 4.29: The correlation maps of configuration 2 for data (a) and simulation (b). The correlation factor was calculated using Eq. (4.13) and its value is included in the plots, on top of the colored scale, for each tower pair (m, m').

is characterized by a narrow core and a broad base. The function used to describe the average transverse energy profile of the shower is a Gaussian for the core part and a form inspired by the Grindhammer-Peters parameterization [86] to account for the tails,

$$F_E(r) = A_C e^{-\left(\frac{r}{R_C}\right)^2} + A_T \frac{2r^\alpha R_T^2}{(r^2 + R_T^2)^2} , \tag{4.14}$$

and integrating over the horizontal position X, the vertical energy distribution $G_E(Y)$ is

$$G_E(Y) = \int_{X_{min}}^{X_{max}} \left(A_C e^{-\left(\frac{\sqrt{X^2+Y^2}}{R_C}\right)^2} + A_T \frac{2(\sqrt{X^2+Y^2})^\alpha R_T^2}{((X^2+Y^2)+R_T^2)^2} \right) dX . \tag{4.15}$$

Here A_C, R_C, A_T, R_T and α are parameters to be determined by fitting the function to the measured distribution. The range (X_{min}, X_{max}) is defined by the sensor geometry which corresponds to two sectors. The integration is performed numerically. By fitting $G_E(Y)$ to the shower transverse profile, and finding its parameters, the original $F_E(r)$ can be recovered and then used to determine R_M from Eq. (4.11).

The form of the function at Eq. (4.14) was chosen because it describes best the data, though it is known [84] that such functions can be used to describe the data only up to about 3.5 Molière radii (99% of the energy containment).

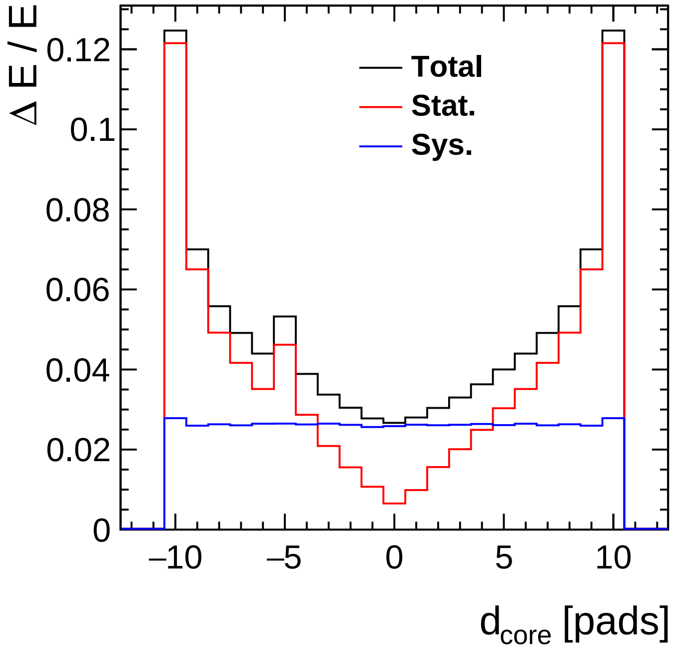

Figure 4.30: The contribution of the systematic (in blue) and statistical (in red) uncertainty, from all layers in configuration 2, to the overall uncertainty in each tower.

4.3.3.5 Simulation of a complete Calorimeter

For the numerical integration, the integration limits of the normalization integral in the denominator of Eq. (4.11) must be chosen such that the relevant range in r is covered. The part of the function in Eq. (4.14) which describes the energy deposition far from the shower axis does not provide a fast convergence of that integral. That is why the solution of Eq. (4.11) may depend on the upper limit of the integration.

To this end, additional MC samples with a slightly modified geometry of the calorimeter was used in order to estimate the systematic uncertainties caused by the choice of the trial function in Eq. (4.14) and its normalization in Eq. (4.11). For this study, the sensitive detector of the sampling calorimeter was implemented with a fine granularity of 0.5×0.5 mm^2 and the transverse size of the calorimeter was extended up to 40×40 cm^2. Twenty thousand electrons with 5 GeV momenta were simulated.

In this detailed simulation, 99% of the deposited energy for the second configuration of the beam test setup was contained inside an area limited by a radius of $R = 84.5 \pm 0.5$ mm. This limit was used for the integration of Eq. (4.11) and the left hand side of the equation was changed accordingly to 0.9091. This simulation also allowed to estimate the fraction of the energy collected by the part of the LumiCal sensor which was equipped with readout electronics (97.8 %). This fraction was used as a sanity check for the fit results, since it can be derived also from the ratio of the integral of the fitted energy distribution function over the instrumented area to the total integral. Finally it was established that the effect of the approximation of the circular shape of LumiCal sensor pads by strips is negligibly small in the center of the distribution in Eq. (4.15) and it is below 2% in the tails where the statistical uncertainty is significantly higher.

4.3.3.6 Effective Molière radius results

The average transverse distribution of the deposited energy, $< E_m >$, was constructed as noted above, for both data and simulation for each configuration. An example of the shower transverse profiles (data in blue and simulation in red) for configuration 2, expressed as the distance from the shower core, d_{core} in units of pads, is presented in Fig. 4.31(a). The vertical energy distribution $G_E(Y)$, introduced in Eq. (4.15), was fitted separately to the data and the MC sample and is shown in Fig. 4.31(a) as the solid line. For the fitting procedure, the integral of the function inside the bin, normalized by the bin width, was used. The fit results set the values of the parameters that are shared between the vertical energy distribution, $G_E(Y)$, and the original energy density function $F_E(r)$ introduced in Eq. (4.14).

Figure 4.31(b) describes the behavior of the normalized average energy density function integral in the radial direction, I, presented in Eq. (4.11), calculated numerically. The horizontal dashed line represents the 0.9091 level, and the crossing point between the line and, I, represents the numerical solution for Eq. (4.11), and determines the value of the effective Molière radius.

The results of the calculation are summarized in Table 4.4, where the effective Molière radius is given for all the configurations used in the beam-test and for the corresponding simulations. In order to estimate the systematic uncertainty of the numerical calculation, the fit to the shower transverse profile and the effective Molière radius extraction was repeated 1000 times for each set. In each repetition, every point in the transverse profile was shifted randomly according to a Gaussian distribution with a σ equal to the point uncertainty, before the fit procedure.

	Data			MC		
Configuration	R_M [mm]	χ^2/NDF	α	R_M [mm]	χ^2/NDF	α
1	21.5 ± 0.8	1.8	1.39 ± 0.03	20.4 ± 0.8	2.0	1.26 ± 0.05
2	23.7 ± 1.1	0.6	1.38 ± 0.05	24.3 ± 0.9	0.9	1.28 ± 0.04
3	23.1 ± 0.6	0.4	1.36 ± 0.05	23.2 ± 0.9	1.1	1.26 ± 0.05

Table 4.4: The effective Molière radius results, data and simulation, together with the χ^2/NDF and the value of α from the fit to the radial distribution.

The three configurations, when properly combined, allow to follow the development of the shower in more detail than each configuration separately and in steps of 1 X_0. The average energy deposition in each radial distance from the shower core per layer is denoted by $< E_{ml} >$. For the layers that are probed more than once, the appropriate average is used. The variable $< E_{ml} >$ as a function of the distance from the shower core, d_{core}, is plotted for each layer in the lego plot presented in Figure 4.32 for data and for simulation. The simulation is in good agreement with the measurements.

In order to build the shower transverse profile for all measured layers, the average energy deposited per layer, $< E_m >$, is constructed as the sum of $< E_{ml} >$ over all layers. The shower transverse profile for the combination of all layers from the three configurations, is presented in Figure 4.33.

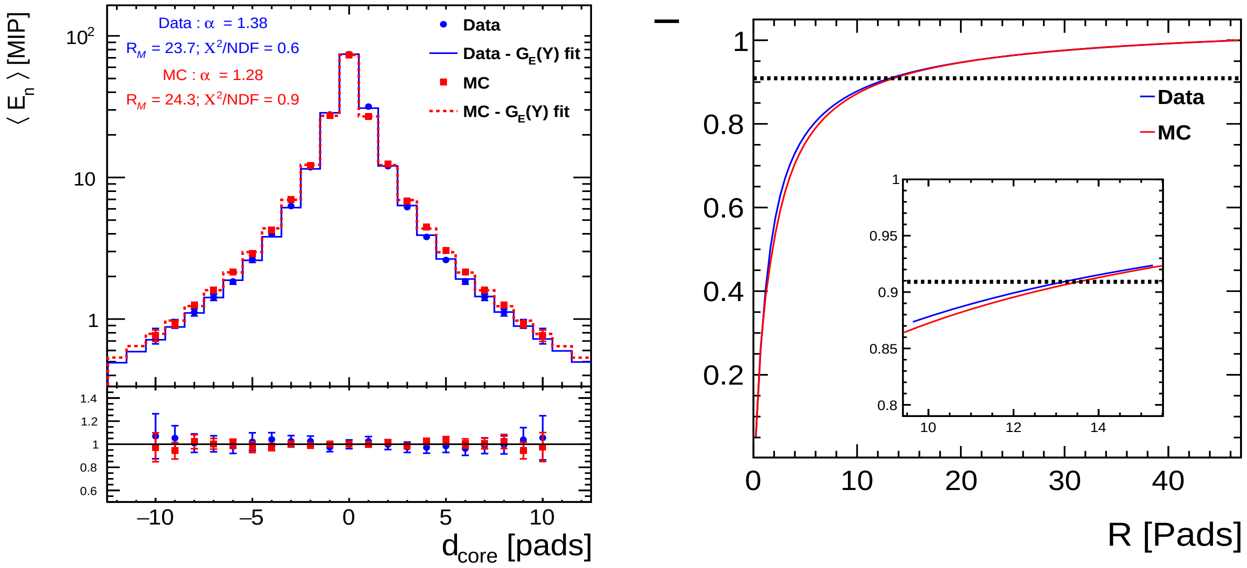

(a) **(b)**

Figure 4.31: (a) The shower transverse profile $< E_m >$, as a function of d_{core} in units of pads, from data and simulation, after symmetry corrections and fit. The lower part of the figure shows the ratio of the distributions to the fitted function, for the data (blue) and the simulation (red). (b) The integral on $F_E(r)$, I, that was extracted from the fit in (a). The insert in (b) shows an expanded view of the region $10 < R < 15$ pads.

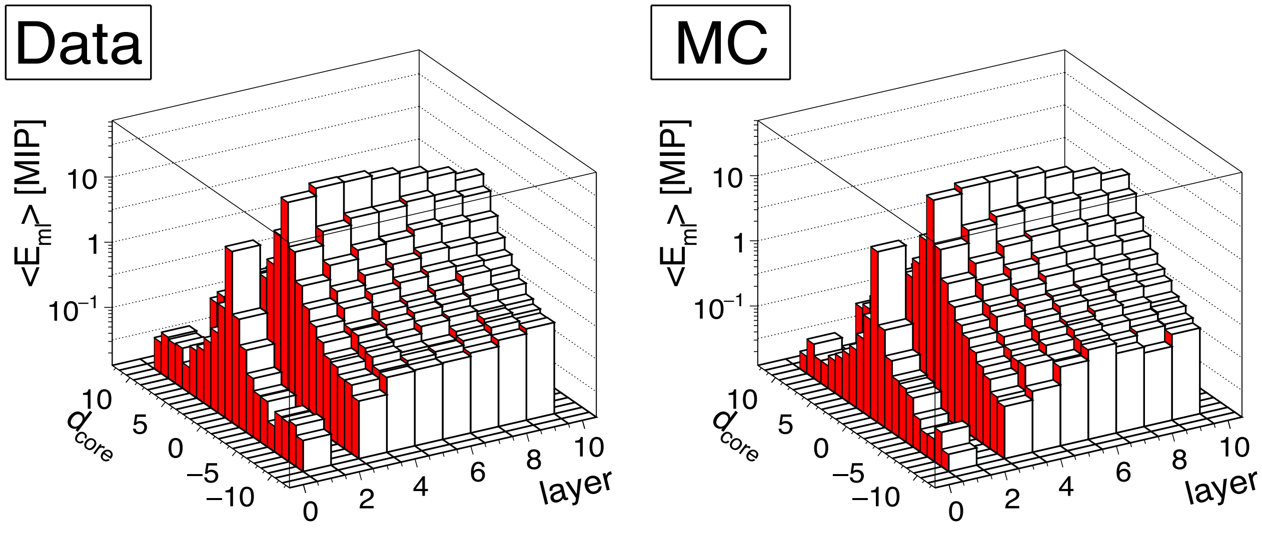

(a) **(b)**

Figure 4.32: A lego plot of the transverse profile $< E_{ml} >$, as a function of d_{core} in units of pads, for each layer from the beam-test data (a) and for the simulation (b).

The fit and the solution of the algebraic Eq. (4.11) were calculated numerically in the same manner as for each configuration separately.

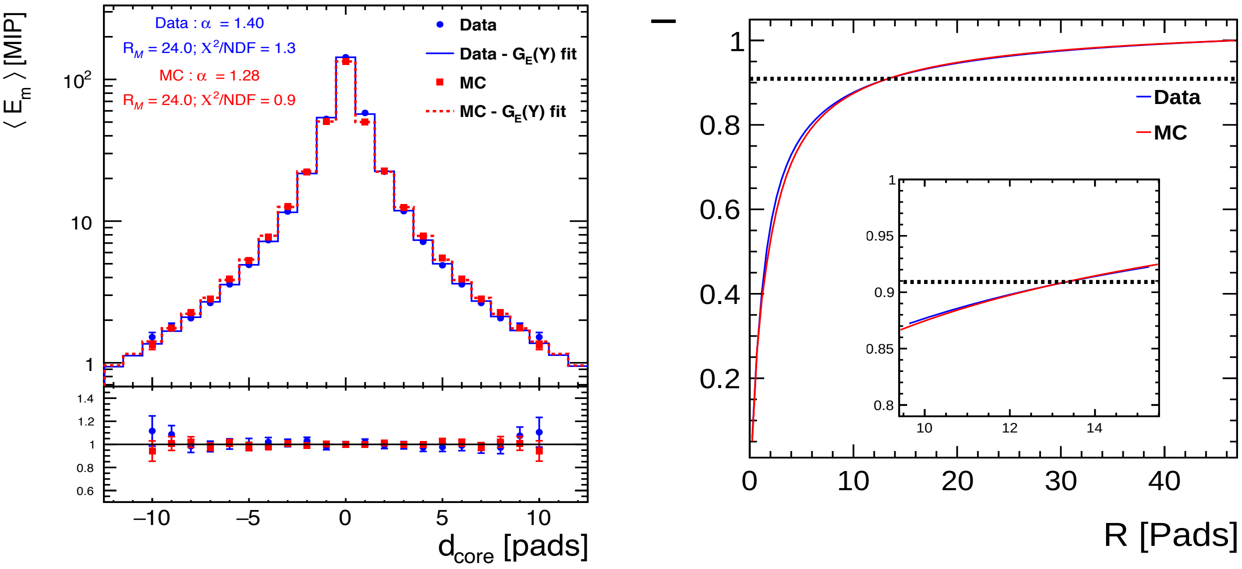

(a)

(b)

Figure 4.33: (a) The shower transverse profile $< E_m >$, as a function of d_{core} in units of pads, of the joint distribution of all three configuration from beam-test data and the simulation, after symmetry corrections and fit. The lower part of the figure shows the ratio of the distributions to the fitted function, for the data (blue) and the simulation (red). (b) The integral on $F_E(r)$, I, that was extracted from the fit in (a). The insert in (b) shows an expanded view of the region $10 < R < 15$ pads.

Data			MC		
R_M [mm]	χ^2/NDF	α	R_M [mm]	χ^2/NDF	α
24.0 ± 0.6	1.3	1.40 ± 0.03	24.0 ± 0.6	0.9	1.28 ± 0.03

Table 4.5: The effective Molière radius results, data and simulation, together with the χ^2/NDF and the value of α from the fit to the radial distribution.

The results of the calculation are summarized in Table 4.5, where the effective Molière radius is given for the combination of all configurations used in the beam-test and for the corresponding simulation.

It is worth noting that the value obtained by using the formula for composite material given in [84] is lower (∼17 mm) than the one obained from this analysis. This is due to the fact that the composite material formula is not precise enough to describe a layered structure with the thickness of the layers large compared to the appropriate radiation length [87], as was the case in the present setup.

The systematic uncertainty was estimated by taking into account the uncertainty of the normalization factor used from the complete calorimeter, from the integration range in X and of the constraint of

97.8%, also from the complete calorimeter. After adding them in quadrature, the total systematic uncertainty results in ± 1.5 mm. Thus the result of the effective Molière radius determination is

$$R_{\mathcal{M}} = 24.0 \pm 0.6(\text{stat.}) \pm 1.5(\text{syst.})\text{mm} \,. \tag{4.16}$$

4.4 Summary

The 2014 beam-test was the first time a multi-plane operation of a LumiCal prototype was carried out. The beam-test demonstrated that major LumiCal components, to be used at a future experiment at CLIC or ILC, developed by the FCAL collaboration, can be operated as a system. The development of the electromagnetic shower was investigated and shown to be well described by a GEANT4 Monte Carlo simulation.

The beam-test information allows to get a few meaningful results, that can show that the calorimeter design is well understood and should meet the expected performance. The first is its ability to measure the electromagnetic shower, and to separate between different particles according to their shower signature. It was also possible to get the shower position resolution from the calorimeter for 5 GeV electrons and it was measured to be 505 ± 10 μm. A similar result was obtained with the simulation. This outcome suggests that the obtained results are in line with the resolution of the full detector simulation. It was also possible to determine the effective Molière radius of the configurations used in this beam-test to be 24.0 ± 0.6 (stat.) ± 1.5 (syst.) mm with an excellent agreement between data and simulation. This latter result, is higher than expected in the detector design, due to large air gaps between absorber layers. In order to improve this result a new thin LumiCal module was design and tested during a beam-test in 2016. The new module and the 2016 beam-test with its results are the subject of the next chapter.

CHAPTER 5

LumiCal compact prototype study

One of the main LumiCal design requirements is to keep it very compact. As was previously argued, this ensures an optimal angular acceptance for low-angle Bhabha scattering, while limiting the space with maximally reduced material content within the full detector system. In order to meet this design goal, LumiCal is foreseen as a dense structure of silicon sensor and tungsten absorber layers, where the space between two absorber layers is set to be 1 mm. The tungsten structure for beam-test purposes was designed accordingly Section 4.1.1.

During the first LumiCal multi-plane beam-test held in 2014 at CERN and discussed in Chapter 4, the LumiCal first sensor module was built from a thick 2.5 mm PCB board. Because of that, the module could not be inserted in the 1 mm gap between two absorber layers. Since the mechanical tungsten structure had a fixed pitch-size, the only way to insert the sensor module was by removing one absorber layer after every two layers, which left an extra 5.5 mm air-gap between the absorbers. This relatively large air-gap caused a wider transverse shower, resulting in a large effective Molière radius, higher than expected in the detector design. In order to improve this result, a new thin LumiCal sensor module was designed, as described in Section 3.4, and tested during the beam-test in 2016 at DESY.

The details of the 2016 beam-test set-up and its results are the subjects of this chapter.

5.1 Beam-test setup

Prototypes of thin LumiCal modules were installed in the 1 mm gap between the tungsten absorbers and tested in two beam-test campaigns in 2015 and 2016 in test area 21 at the DESY-II synchrotron with secondary electrons of energies between 1 GeV and 5 GeV.

The electron beam is generated as illustrated in Fig. 5.1. First a bremsstrahlung beam is generated from a 25 μm thick carbon fiber (primary target) in the synchrotron beam of the DESY-II ring. A metal plate (secondary target) is used to convert the bremsstrahlung photons into electron and positron pairs. A dipole magnet spreads the beam out into a horizontal fan, and a set of collimators form the extracted beam. The magnet setting was used also to control the energy of the beam, by selecting the momentum of the particles that pass through the collimator at the entrance to the test area. This provided electrons with energies from 1 to 5 GeV in the test area. A detailed description of the DESY-II beam-test can be found in [88].

After the entrance to the test area, the electron beam passes through a narrow (5×5 mm) square lead-collimator that helps to limit the beam spread along the test setup. The geometry of the test setup is shown in Fig. 5.2. Upstream of the LumiCal test structure, the AIDA/EUDET beam telescope was placed. The telescope was split into two parts, each containing an arm with three layers of the MIMOSA-26 detectors and two thin scintillator counters for the trigger system. The telescope front arm was placed before the test area dipole magnet, to record the incoming electrons.

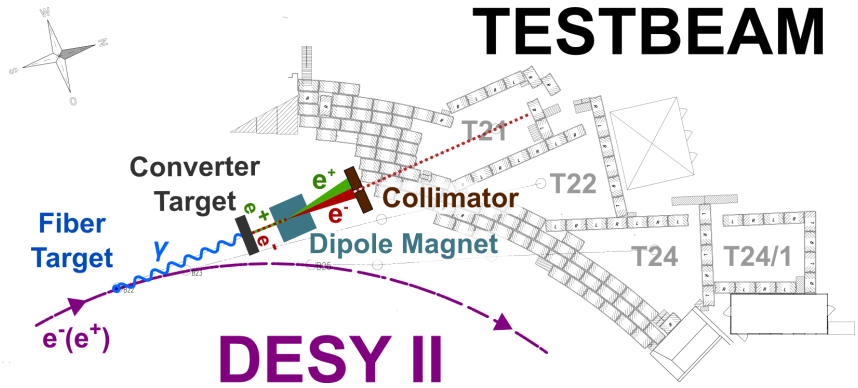

Figure 5.1: Schematic layout of the electron beam generation at DESY-II beam-test area.

This dipole magnet was used to test the idea of installing tracking detectors in front of LumiCal in order to enable separation of photons from electrons. The magnet was active only in dedicated runs, in which a copper target mounted in front of it was used to generate bremsstrahlung photons.

The rear arm of the telescope was placed after the dipole to record the electrons from the beam or, in the runs with the copper target, to separate them from the radiated photons. Two of the LumiCal sensor modules were placed in front of the calorimeter prototype and acted as tracking devices.

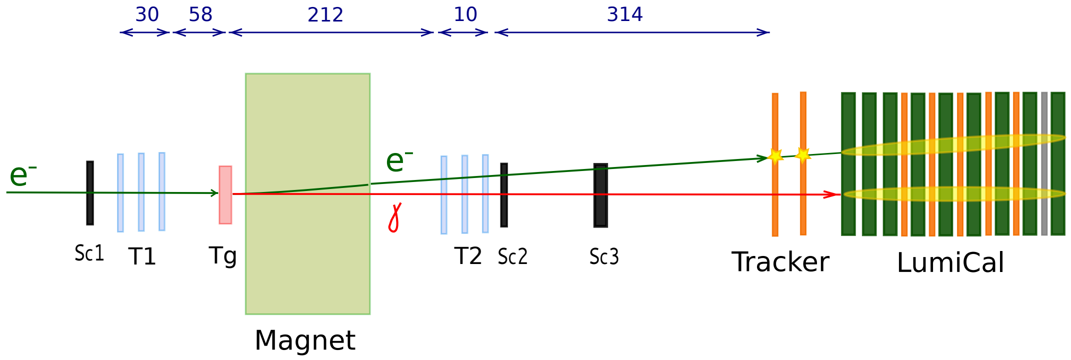

Figure 5.2: Diagram of the beam test setup (not in scale). Sc1, Sc2 and Sc3 are scintillator counters; T1, T2 – the three pixel detector planes of the telescope and Tg the insertable copper target for generating bremsstrahlung photons. Distances, rounded to integer numbers in centimetres, are shown in the upper part of the figure.

The LumiCal prototype and tracker were assembled in the same mechanical structure as was used in the 2014 test campaign at CERN (see Section 4.1.1 for details). The thin LumiCal module was attached to the tungsten absorber plate by adhesive tape. The tungsten plate was permanently glued to the permaglass frame and fixed in the comb slots of the mechanical structure. For the LumiCal assembly six of the eight new thin modules were used (modules 3-8). The sensor modules were inserted every 1 X_0 starting after the 3^{rd} absorber layer. The two remaining thin LumiCal modules (modules 1-2), constitute the tracker part of the setup and were installed in front of the calorimeter. The assembly of the LumiCal prototype is illustrated in Fig. 5.2 where the layers layout is presented and can be seen from a top view before the installation in the beam in Figure 5.3. The last module (module 8) was assembled using the TAB bonding technique (as mentioned in Section 3.4), and was not used in the present analysis which therefore reports only on the results of the other seven layers setup.

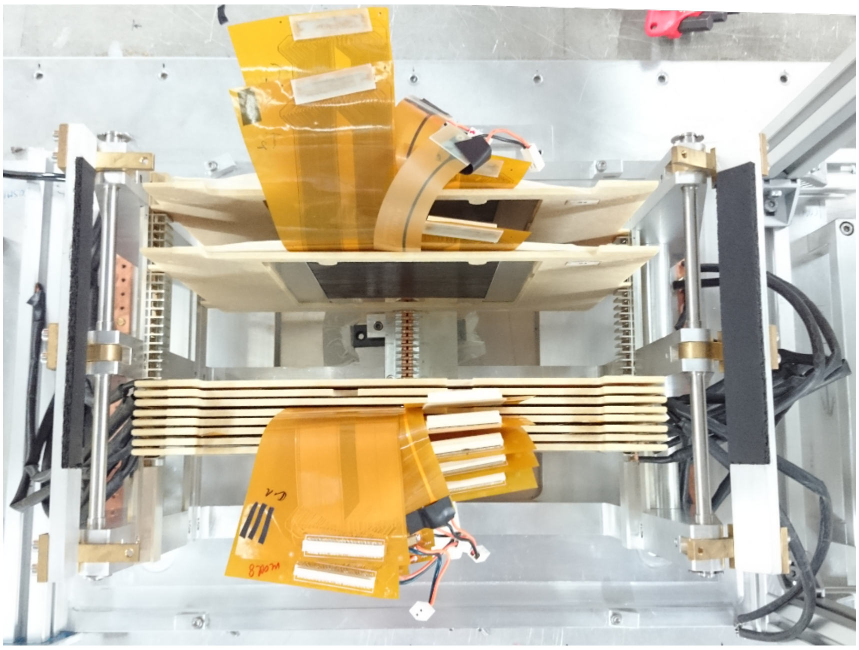

Figure 5.3: Top view of the assembled LumiCal prototype.

5.1.1 Readout electronics

The FCAL readout board, that was used in the 2014 tests [89] and during previous campaigns [66], described in Chapter 4, was not suitable for the 2016 test beam. It was too thick compared to the new sensor modules, and it contained only four sets of eight channel front-end and ADC ASICs, for a total of 32 out of 256 channels in a layer. In addition it was not designed to operate in large numbers as a full system. A new set of multi-channel ASICs for LumiCal, under the name FLAME [90], are under development in the FCAL collaboration, but they were not yet ready for this test beam campaign.

As an intermediate solution, a Scalable Readout System (SRS) [91] with a front-end hybrid board [92] based on the APV25 chip was adopted and was used for the readout. The APV25 chip has 128 readout channels, each consisting of a charge-sensitive preamplifier and a shaper with an effective CR-RC filter producing a 50 ns shaped voltage pulse [93]. The output of the shaper is sampled at 40 MHz and stored in an analog pipeline. During the beam-test, the APV25 boards were configured to operate in multi-mode transmission of 21 consecutive pipeline samples of each channel to the Adapter Board of the SRS through HDMI cables of 3 m length. These samples were converted by a 12-bit ADC in the SRS Adapter Board and transmitted to the data acquisition PC over an ethernet connection.

Simulation results for the present configuration showed that a single pad in a shower can be hit by up to 80 relativistic particles, hereafter referred to as MIPs (see Fig. 5.10 in Section 5.2.2). The APV25 board, which has a dynamic range for energy depositions of up to 8 MIPs, is not meant to read out sensor pads inside an electromagnetic shower. In order to enable measurements of a wider range of deposited energies, a dedicated capacitive charge divider was connected to the input of the APV25 board. The attenuation factor of the charge divider was optimized by using the results from simulation. The simulation of the observed noise level and the geometry of the present calorimeter showed that an attenuation of the signal by a factor of 3.5 – 4.5, is adequate. With this attenuation factor, small signals from pads with low energy depositions, for example from the tails of the shower, fall below the detection threshold. This effect leads to a loss of information on the development of the electromagnetic shower, the treatment of which will be described later.

5.1.2 AIDA Telescope

The AIDA/EUDET-type beam telescopes are tabletop tracking detectors commonly used in beam-tests mainly for detector performance and detector R&D studies. The original telescope was constructed as part of the EUDET project (in the FP7 European Commission programme). The success of the telescope program and the increasing demand of the detector R&D community led to the construction of several replicas, commonly called AIDA/EUDET-type beam telescopes. Such an AIDA/EUDET-type beam telescope, DATURA, is installed in beam line 21 used in the 2016 LumiCal beam-test.

The telescope consists of six pixel-detector planes equipped with fine-pitch MIMOSA-26 sensors. The planes are organized in two arms, holding three sensors each, usually the device under test (DUT) inserted between the two arms of the telescope. In this configuration the telescope pointing resolution on the DUT can reach 3 μm. In addition, the telescope is equipped with two pairs of scintillation counters (denoted as Sc1 and Sc2 in Fig. 5.2) and a trigger logic unit TLU. The telescope is operated by the EUDAQ data acquisition system that was developed under the same framework for easy integration between the telescope and the DUT to a single DAQ.

In the 2016 test beam, the telescope arms were placed one before and one after the dipole magnet. The LumiCal prototype calorimeter was placed down-stream of the second arm shown in Fig. 5.2. The configuration was set in this manner in order to study the identification of electrons and photons in the LumiCal calorimeter. The analysis of the identification and separation between photons is not part of the scope of this study and will not be discussed further.

During the beam-test, the telescope scintillation counters and the TLU were used for triggering. The information from the telescope had to be synchronized with the LumiCal data.

5.1.3 DAQ

Figure 5.4 presents a sketch of the DAQ connection of the test setup. The DAQ consisted of two interdependent DAQ systems. The first one was the EUDAQ system to control the beam telescope and the TLU. The second one was the LumiCal DAQ, this time based on the SRS developed by the RD51 collaboration and described in the next section.

A trigger signal was generated in the TLU, as a combination of signals from the Sc1 and Sc2 counters. The TLU then sent the trigger signal to both the telescope DAQ and to the SRS. In order to prevent the TLU from sending more signals before the event acquisition ends, a BUSY signal was needed. The SRS does not have a BUSY signal, so an artificial signal was provided by a NIM logic system, which duplicated the trigger signal and sent it to the SRS.

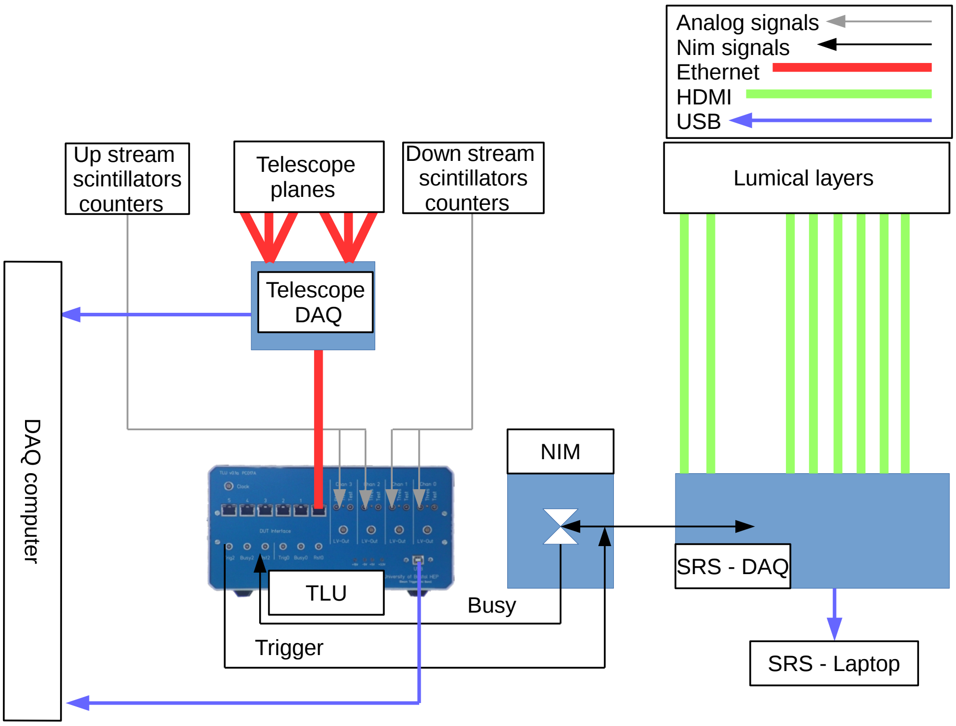

Figure 5.4: Schematic description of the Data Acquisition System used in the 2016 beam-test.

5.1.4 Simulation

The LUCAS stand-alone software, that was used for the 2014 beam-test simulation Section 4.2.2, was modified in accordance with the 2016 beam-test setup. A new LumiCal sensor module was introduced to simulate the new sub-millimeter carbon fiber module. The carbon fiber was defined as 50% carbon and 50% epoxy by weight, with a total density of$1.6\,\mathrm{g/cm^3}$.The carbon fiber thickness was set to be 790 μm and the silicon sensor and fan-out parts were embedded in it.

The silicon sensor was updated to include the back and front 20 μm aluminum metalization on top of the 320 μm thick silicon part. Fan-out parts were composed as a mixture of Kapton, copper and epoxy, and included the adhesive layers attached to them. In the sensor area, the carbon fiber thickness was set to 130 μm, the difference between the total width of the support structure and the sum of all the sensor parts.

The simulated calorimeter structure consisted of eight sensor layers, two of which formed the tracker system while the other six were inserted between the tungsten absorber layers, similar to the actual setup used in the beam-test. The tungsten absorber layers were composed of two alloys as described in Section 4.1.1, and were placed according to the sequence used in the beam-test. The setup was placed at a distance of 3.3 m from the particles source position, similar to the distance from the telescope to the LumiCal in the beam-test.

The beam was simulated as coming from a square source with an area of $7.6 \times 7.6\,\mathrm{mm}^2$, and the track angular distribution was generated such that the beam profile would imitate the beam profile measured in LumiCal. The center of the square was shifted such that the center of the beam would hit pad 45 between the two central sector as in the beam-test. For each beam energy used in the test

$(1 - 6\ GeV)$, a set of 50k electrons was generated. For calibration, the same energy scale as in the 2014 test beam simulation was used. The energy deposited in each pad was counted in MIPs, where 1 MIP was set to 88.5 keV, the MPV of the energy deposited by a simulated 5 GeV muon in the silicon sensor.

5.2 Data analysis

5.2.1 Signal processing

In the LumiCal DAQ, the readout in each channel consisted of 21 consecutive samples, 25 ns apart. The signal-reading window could be adjusted relative to the trigger time to account for the length of the trigger lines and logic. The time window was set such that it contained the entire signal. An example of the signal for a single channel, after baseline and common-mode noise subtraction, is presented in figure 5.5.

During the test beam, before each set of measurement runs, and after every change in the system, a pedestal run was taken. A pedestal run is a run without beam where the readout system is triggered by an internal software trigger. In a pedestal run, around 5-10k events were collected for all connected channels. The data collected in the pedestal run were used to calculate the baseline and noise parameters for each channel, which were then used in the zero suppression (ZS) processing during data collection with the beam. The baseline for each channel was calculated as an average of all the samples in the pedestal run, and the noise was estimated as the standard deviation of the samples in the run. In a beam run, the average of 21 samples of each channel was calculated for each trigger and compared to the ZS threshold. If it was below the threshold, the data for that channel were not recorded. The threshold was set to 0.4 times the channel noise which resulted in a low enough threshold so as not to reject real signals.

Since the data were collected in an asynchronous mode, like in the 2014 test beam, the signal was not sampled exactly at its maximum. To evaluate the signal maximum it was fitted with a $CR - RC$ filter response function:

$$S(t) = A\frac{t - t_0}{\tau}e^{-\frac{t-t_0}{\tau}}\Theta(t - t_0), \tag{5.1}$$

where t_0 is the arrival time of the signal, $\tau = 50$ ns is the peaking time of the APV25 chip and A is the signal amplitude. The function $\Theta(t - t_0)$ is the Heaviside step function. In this approach, the signal amplitude is estimated as Ae^{-1}, which gives an unbiased estimation of the signal.

The relatively low ZS threshold allowed a significant amount of the noise to pass through and further signal selection criteria were applied for the analysis. First, an artificial neural network (ANN) was used to analyze the signal and classify the data based on its shape. The training set for different signal amplitudes was generated using the function (5.1) with a Gaussian noise added to each sample. In addition, some particular noise-patterns from the data were included in the training set. After signal preselection based on the ANN, it was fitted with (5.1) (Figure 5.5), where the signal amplitude, arrival time t_0 and peaking time τ were used as parameters. To further improve the purity of the signal, the selection criteria were applied to the parameters t_0 and τ. The efficiency of the selection was studied using an external pulse, as described in Section 5.2.2.

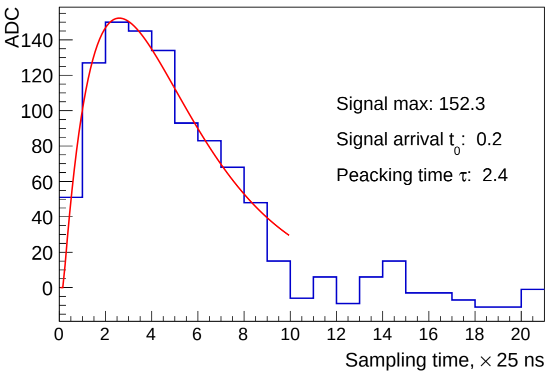

Figure 5.5: Signal waveform sampled in 25 ns time intervals. The red line is a fit with $CR-RC$-response function (5.1).

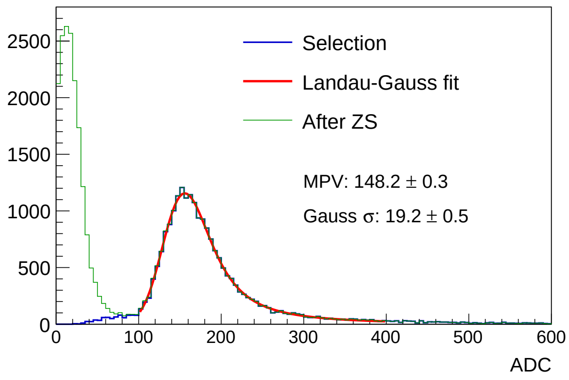

Figure 5.6: Signal distribution in a single pad of the tracking layer. The green line – after zero suppression, blue – after additional selection criteria and red – fit with convolution of Landau and Gauss distribution functions.

Figure 5.6 shows the distribution of the signal produced by a 5 GeV electron beam and measured in a single channel of one of the tracking planes. The distribution is shown for the signal with only the ZS threshold and after applying additional selection criteria. The latter lead to a very effective noise suppression in the analysis. The MPV of the signal is estimated using a fit with a convolution of the Landau and Gauss distribution functions. The σ parameter of the Gaussian distribution is considered as a noise measurement. The MPV values of the signal produced by the 5 GeV electrons in channels affected by the beam are presented in Figure 5.7. The higher MPVs for small pad numbers reflect the geometry of the sensor where these pads have smaller area and smaller capacitance. The same effect is observed for the signal-to-noise ratio presented in Figure 5.8. Since the beam profile has blurry edges, the statistical uncertainties increase for pads which correspond to the periphery of the beam. For most of the channels the signal-to-noise ratio is within a range of 7 to 10.

For the modules which were installed in the calorimeter prototype and used the charge divider, the single particle signal-to-noise ratio cannot be measured. Taking into account the design of the charge divider and the noise which is measured in the pedestal run (Fig. 5.9), the estimated value of signal-to-noise ratio is in the range of 2 – 3. In spite of such a small S/N, the signal-shape analysis using ANN with additional selection-criteria on the fitted shape parameters, provide an effective way to identify the signal and reject the noise.

5.2.2 Calibration of APV 25

The linearity of the APV25 boards was studied with the bare chip [92, 93] and it was found to be very good for signals of up to 3 MIPs and better than 5% up to 5 MIPs. As noted before, the APV25 boards, connected to calorimeter layers, were equipped with a capacitive charge divider. The measured energy range in a pad inside the calorimeter, equipped with a charge divider, exploit the full dynamical range of the APV25 and even saturates it. Therefore it is essential to understand the known non-linear behavior of the APV25.

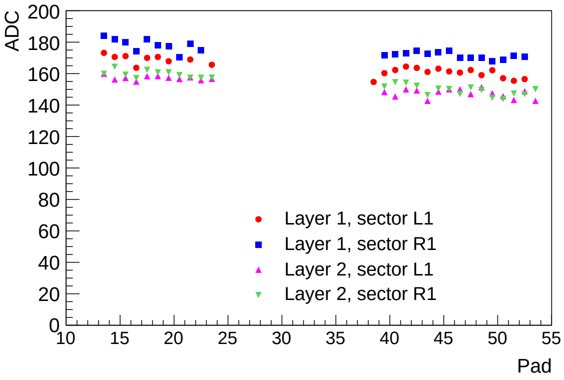

Figure 5.7: Most probable value of the signal in the pads of the tracking layers covered by an electron beam of 5 GeV.

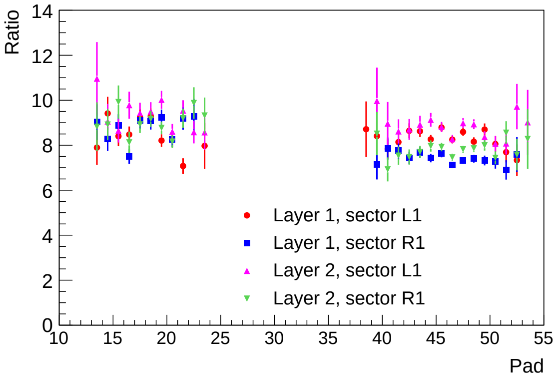

Figure 5.8: Signal to noise ratio for the pads of the tracking layers covered by an electron beam of 5 GeV.

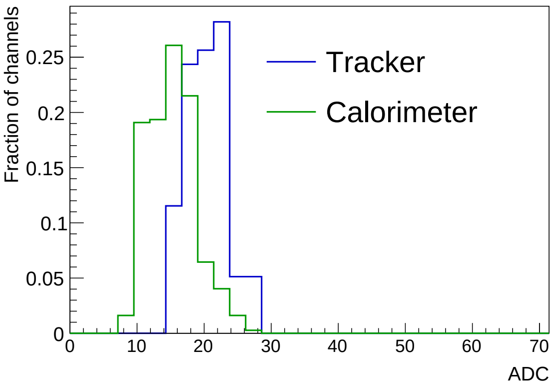

Figure 5.9: Noise distribution in channels of tracking layers (blue) and calorimeter layers (green) from a calibration run.

Since the APV25 board is widely used in many experiments, its nonlinearity was widely studied. Studies like in [94] suggest to use an exponential extrapolation to describe its behavior in the nonlinear regime.

A comparison of the pad energy distribution in the third calorimeter layer (after 5 tungsten plates), between the simulation and the beam-test data treated with different APV25 response functions is presented in Fig. 5.10. With the linear response function, the data clearly deviate from the MC samples expectations while for an exponential extrapolation of the response function for large signals, the comparison improves though there is still a marked disagreement. The exponential extrapolation was obtained, following the recommendation of [94], by requiring a smooth continuation of the response function and its slope starting in the middle of the dynamical range.

In order to improve the results, the relative response of the APV25 channels equipped with a capacitive charge divider was measured in the lab. A voltage pulse was supplied to the channel input through a capacitor of 2 pF. The detector capacitance was simulated by a 7 pF capacitor connected in parallel to the channel input. About 10 randomly-chosen channels for each APV25 board were measured and the average response curve was calculated for each APV25. Figure 5.10 presents also the data corrected with the response function obtained by interpolation between the measured values. The measured distribution of the deposited energy in a single pad is well reproduced by the simulation for signal amplitudes larger than 5 MIPs.

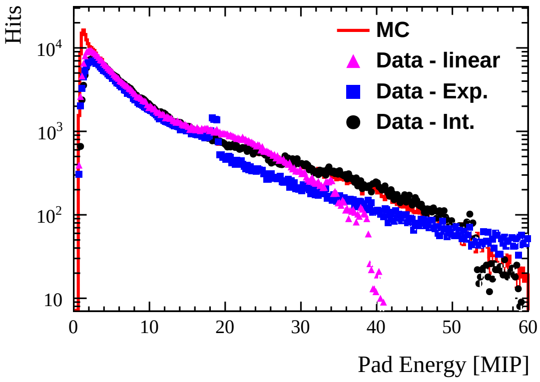

Figure 5.10: Distribution of the deposited energy in a sensor pad after 5 tungsten plates. The red histogram is the MC simulation and the pink triangles are the data assuming a linear APV25 response function. The blue Squares are obtained with an exponential extrapolation of the response function from the middle of the APV25 dynamical range and the black circles correspond to data obtained using the measured response function of the APV25 board.

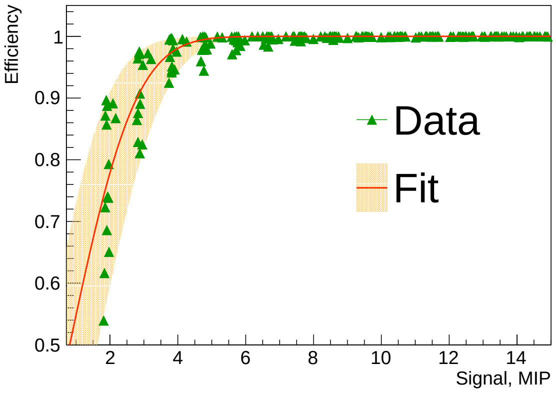

Figure 5.11: Efficiency of signal identification as a function of the signal amplitude. Green triangles are measured for different channels, the red line is an average of the fit using Eq. (5.2) to a large number of channels, and the shaded area corresponds to the spread of fits at small amplitudes.

The APV25 board with charge divider approaches saturation at about 1600 ADC counts. In this analysis, the maximum signal size is 1450-1550 ADC counts, reasonably well below the saturation limit. However, smaller signals become masked by the noise. This loss of signals is visible in Figure 5.10, where for small amplitudes the experimental distribution is below the MC sample expectation.

In order to understand this loss of signals, the efficiency ϵ of identifying the signal of a small amplitude is studied with the same setup using an external voltage pulse.

The efficiency of signal identification is defined as the ratio of the number of identified signals to the number of generated ones. For each APV25 board, about 10 channels are measured. This ratio depends on the signal-to-noise ratio and therefore it is slightly different for different APV25 boards, as shown in Figure 5.11 where the results for channels of different APV25 boards are presented. For signals larger than 10 MIPs, the efficiency is 100% in all channels. For a smaller number of MIPs, some channels give lower efficiencies. The measurements of the efficiency, ϵ, are fit by the following expression:

$$\epsilon = p_0 \left(1 + erf\left(\frac{S - S_0}{p_1}\right)\right), \tag{5.2}$$

where *erf* is the error function, S the signal amplitude and p_0, p_1 and S_0 are fit parameters. The curve in Figure 5.11 represents the average of the fit of a large number of channels and the shaded area, the spread of the fit in these channels at low signal amplitudes. Subsequently, the efficiency correction for small signals is applied to the beam-test simulation using the results of the fit to Eq. (5.2).

5.2.3 Energy calibration

The APV25 calibration procedure described above brings the average response of all APV25 boards to the same level. In order to compare the simulation results with the data, both should be calibrated to the same energy unit. As noted before, the simulation was scaled to the same energy unit used in the 2014 test beam analysis of 1 MIP as the MPV of the energy deposited by a 5 GeV muon, which is 88.5 keV. Since the DESY beam line does not provide muons, a test bench for cosmic muons was set up in the TAU lab in an attempt to measure the cosmic muon spectra in each channel. However, it quickly became apparent that the inefficiency in reconstructing small signals with the charge divider distorts the muon spectrum such that the MPV is biased.

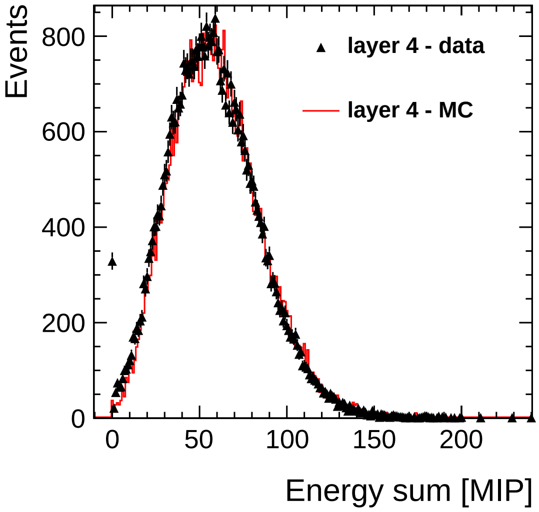

Figure 5.12: The energy distribution deposited in the second layer of the calorimeter, after 4 absorber layers, in the data (black) and in the MC sample (red), following the calibration procedure described in the text.

In order to set the MIP calibration in the data, another approach was used. The distributions of the deposited energy in the second layer of the calorimeter, after four absorber plates, in both data and simulation were extracted. The choice of the second sensor layer is arbitrary to the extent to which it was checked that it had no bad channels. The data energy scale was set such that the mean value of the distribution was equal to the mean of the MC sample distribution. The comparison of the distribution in the data and in the MC samples is presented in Fig. 5.12, after the data energy scale was set. A good agreement is observed also in the shape of the distributions.

5.2.4 Geometrical cuts and bad pads

When examining the recorded data, a few unexpected features appeared that needed to be taken into consideration during the analysis. The first one was the appearance of channels with an unusual response; they were defined as bad pads.

The efficiency curve for each APV25 board is averaged over 10 channels. As can be seen in Fig. 5.11, the average efficiency function reaches its plateau around 2-5 MIPs. The position where the function reaches the maximal height can change from channel to channel and depends on the noise level in the channel. In some cases, when noise levels are high, the inefficiency extends up to more than 20-30 MIPs, and thus most of the information from this channel is lost. An example of such a case can be seen in Fig. 5.13 where the response of pad 45 of layer 6 is compared between the two middle sectors L1 and R1. Since the beam is aligned on the sensor center between the two sectors, the response of the pads should be similar. However, due to the high noise in the R1 pad, the amount of events in the energy range up to 25 MIPs is significant lower than the number of events in sector L2. This kind of behavior will cause a bias in the measured response. Therefore such channels were marked as bad channels and were excluded from the analysis. Thy were added to the list of channels with no response at all, defined earlier as bad channels.

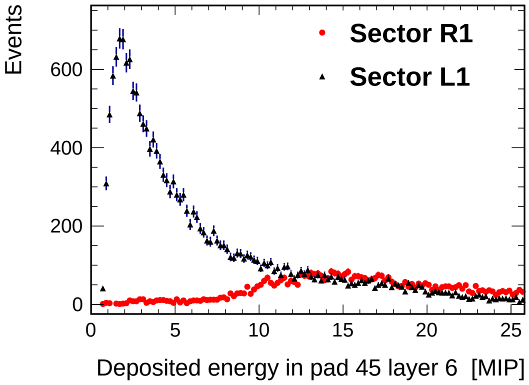

Figure 5.13: Comparison between the distribution of the energy deposited in pad 45 of layer 6 in sector L1 (black) and in sector R1 (red).

The second behavior which had to be considered is seen in Fig. 5.14, where the average of the energy deposited in each pad is presented for each sector of sensor layer 7 as a function of the pad number in the sector. Here the performance of "mirror" sectors (L1 as mirror of R1 and L2 as mirror of R2) can be compared, since the beam was directed into the center of the sensor layer between sectors L1 and R1. The main structure in Fig. 5.14 is the energy deposition from the electromagnetic shower centered in pads 40-50. The main peak appears in sectors L1 and R1, and a shallower peak, centered in the same pads, can be seen in sectors L2 and R2. When comparing sector L1 with R1 and L2 with R2, two unexpected structures appear. A small peak pops up in sector L1 between pads 10-20, while in sector R1 no such peak is observed. Similarly, a small peak can be seen in sector R2 (yellow) centered between pads 35-45 on top of the wider distribution, while in sector L2 (black) only the main bump exists. Since this effect was observed in runs with only a mono-energetic electron beam, the effect most probably originates from either the sensor or the electronics.

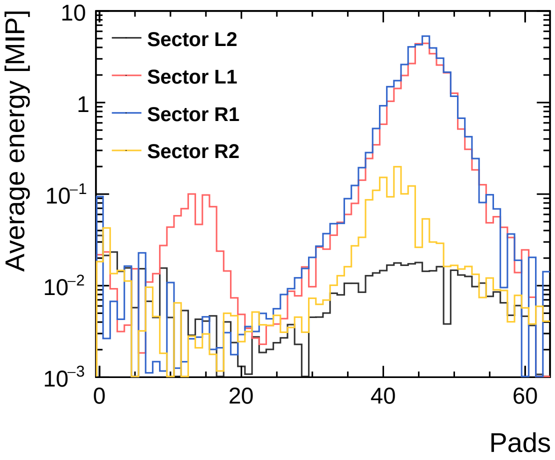

Figure 5.14: Average energy deposited in each pad as a function of the pad number, for each of the four sectors L_1, L_2, R_1 and R_2, for sensor layer 7.

In fact, this outcome was traced back as coming from the APV25 board. From a study on the APV25 performance [95], a cross-talk between separate channels of the APV25 was observed. When large signals, like those in the core of the electromagnetic shower, were measured, cross-talk signals appeared in the APV25 channels where no signal was expected. These channels were separated by about 30 channels from the injected channel. Since these signals appear as real signals and thus cannot be rejected, neither by the signal selection criteria nor by the ANN, a fiducial cut had to be applied, and only the central sectors, L1 and R1, with pads above pad 24 were used for the analysis. The exclusion of bad pads and the fiducial cut were applied on the simulation in the same manner as on the data.

To obtain the radial distribution of the energy deposition in each sensor layer, the energy deposits in L1 and R1 were summed up for each pad, after applying the fiducial cut. Since the beam position along the radial axis is not changing from layer to layer, the differences in the position of the energy deposition between the layers reflects the alignment of the sensor layers. An example is presented in Fig. 5.15, where the radial energy deposition of layers 1 and 2 (tracker layers) are shown on the same axis. The two similar distributions are shifted with respect to each other by 0.5 *pad*, which corresponds to 0.9 mm. To measure the relative displacement between all layers, the mean value of the radial energy deposition in each layer was used. The results of the displacement of each layer relative to the center of pad 45 (the center of the beam spot) are presented in Fig. 5.16. The measured displacements were then implemented in the simulation and after repeating for the MC samples the same analysis as for the data, the resulting misalignment was found to adequately reproduce the one observed in the data as shown in Fig. 5.16.

An example of the LumiCal layers response to a single event, after signal reconstruction, calibration, fiducial cuts and removal of the bad pads is presented in Fig. 5.17. The first two layers, marked as 1 and 2, are the tracker layers. The amount of energy deposited in the tracker layers, is of the order of 1 MIP, and is contained in one pad in each layer. The remaining layers are calorimeter sensor layers and the number assigned to them represents the order of the sensor layer and also the amount of absorber in front of it. The development of the electromagnetic shower along the calorimeter axis

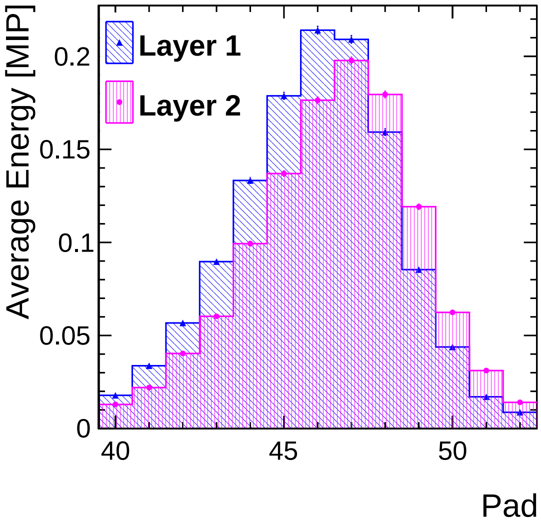

Figure 5.15: Radial energy deposition in pad numbers of tracker layer 1, in blue, and tracker layer 2, in pink.

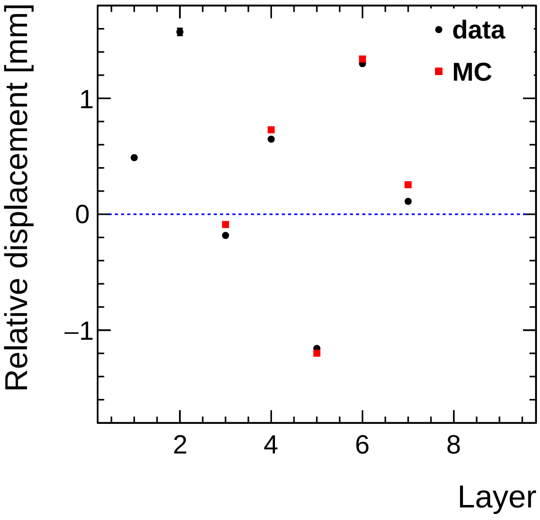

Figure 5.16: Displacement of each sensor layer with respect to the center of pad 45 (beam spot center) in mm, for the data in black and for the MC in red.

both in terms of energy, and transverse dimension, is clearly seen.

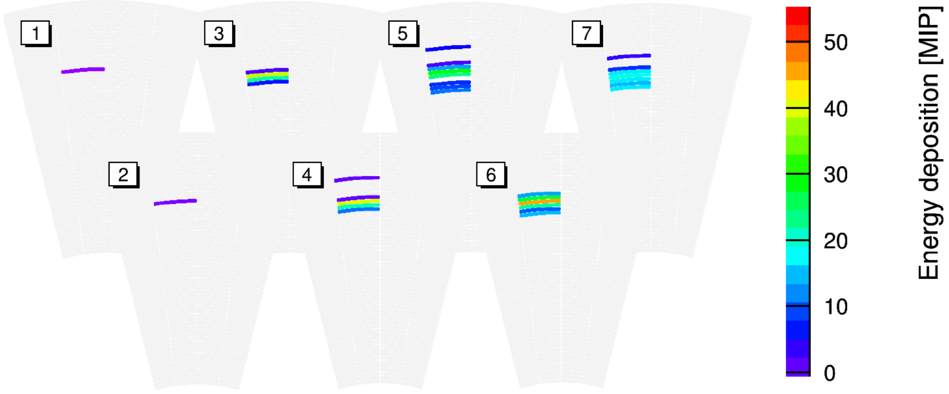

Figure 5.17: LumiCal sensor layer response, to a single event, after the signal reconstruction, calibration, fiducial cuts and removal of bad pads. Layers 1 and 2 belong to the tracker, while the subsequent layer numbers (3 to 7) carry information about the amount of traversed absorber. The pad color represents the amount of energy deposited in units of MIP.

5.3 Results

More than seven million events were collected in an electron beam from 1 GeV to 5 GeV energy, available in 1 GeV steps, for different setup configurations to measure the precision of the shower position, the electromagnetic shower development in longitudinal and transverse directions and the effective Molière radius.

5.3.1 Position reconstruction

The AIDA/EUDET beam telescope was placed upstream of the LumiCal test structure. The telescope can achieve a hit-position resolution of the order of 3 μm [88] when the DUT is placed between the telescope arms. The performance of the telescope depends on the material budget that induces multiple scattering, and on the telescope and DUT configurations. Since the test setup was aimed for the separation of photons from electrons, the LumiCal stack was placed 3.3 m downstream from the end of the telescope. This distance alone can enhance the effect of multiple scattering on the spatial resolution of the telescope. On top of the large distance, trigger scintillators were placed inside the gap for the trigger system. The effect of the material budget between the telescope and the LumiCal can be estimated by the projected distance distribution width from the Coulomb multiple scattering, y^{RMS}, expressed by [84]

$$y^{RMS} = \frac{1}{\sqrt{3}}\theta_0 \,, \tag{5.3}$$

where θ_0 is the width of the angular distribution defined by

$$\theta_0 = \frac{13.6\ \mathrm{MeV}}{\beta c p} z\sqrt{x/X_0}[1 + 0.038\ \ln(x/X_0)] \,. \tag{5.4}$$

Here $p, \beta c$, and z are the momentum, velocity, and charge number of the beam electron, and x/X_0 is the thickness of the scattering medium in units of radiation length. Applying Eq. (5.3) to the effective radiation length of air and scintillators, the estimated spatial resolution of the telescope in the LumiCal setup is about of 1.5 mm.

One of the aims of the prototype performance study was to determine the resolution of the hit position reconstructed from the energy deposited in the calorimeter. The resolution is expected to be better than the sensor segmentation and was measured in previous tests, with similar configurations, to be about 500 μm. The resolution, in the current setup, could not be measured using the information from the telescope and a different approach was needed. The resolution of the position reconstruction in the LumiCal prototype could be estimated using the residuals between the reconstructed hit position in the tracker layers in front of the calorimeter and in the calorimeter itself.

The first step was to measure the hit position from the LumiCal calorimeter stack in a similar way as in the 2014 test beam analysis described in Section 4.3. In the calorimeter part, the information collected for each event, after proper processing, was used to build the radial deposited energy distribution, by summing the energy in each radial pad from all sectors and along all layers. As before, by denoting E_{nkl} as the energy deposited in the the radial pad with index n from layer l and sector k, the one-dimensional radial deposited energy distribution for one event along the Y axis could be obtained from the following sum:

$$E_n = \sum_{k,l} E_{nkl} \,, \tag{5.5}$$

where l runs over all calorimeter layers, and k runs over the two middle sectors L1 and R1.

The radial distribution is fitted with a simple Gaussian distribution to reconstruct the radial position of the shower entry-point. An example of the sum of energy deposited along the radial direction for one event is presented in Figure 5.18.

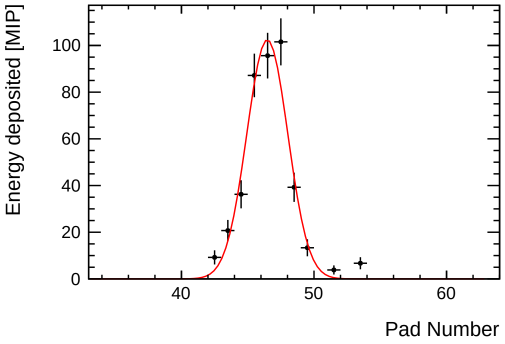

Figure 5.18: Example of the distribution of the sum of deposited energy along the radial direction for a single event, fitted with a Gaussian distribution for hit position reconstruction.

In the tracker, because of the relatively large pad size and the strong electric fields in the sensor, in most of the pad area all the charge induced by a MIP is collected in this one pad. Only in a small band around the pad border, charge sharing between pads occurs. About 95% of the reconstructed hits in the tracking planes consist of one pad, which means that charge sharing between pads has a negligible effect on the particle position reconstruction. The hit position of a single pad hit is assigned to the middle of the pad. In this case the uncertainty of the position reconstruction, for a symmetric beam, can be well approximated by a uniform distribution within the pitch of the sensor, which is $p = 1.8$ mm. Assuming that the uncertainty of the position reconstruction in the calorimeter has a Gaussian distribution, the distribution of the residuals between the position in the tracking layers and in the calorimeter can be described by the following convolution:

$$F(x) = \frac{B}{p\sigma\sqrt{2\pi}} \int_{-\frac{p}{2}}^{\frac{p}{2}} e^{-\frac{(x-z)^2}{2\sigma^2}} \mathrm{d}z\,, \tag{5.6}$$

where σ is the position resolution in the calorimeter, p the pitch of the tracking plane and B provides the normalization. Figure 5.19(a) shows the distribution of the residuals of the reconstructed radial position between the calorimeter and each of the two tracker planes.

The tails of the residual distribution originate from events where the reconstruction of the hit was off by more then one pad. Such a situation can occur because of fluctuations in the energy depositions, the residual misalignment between the layers, and also because of missing channels (pads). In order to improve the fit procedure, the tails of the residual distributions were described by

$$G(x) = \frac{1}{p\sigma\sqrt{2\pi}} \left(B_{-} \int_{-\frac{3p}{2}}^{-\frac{p}{2}} e^{-\frac{(x-z)^2}{2\sigma^2}} \mathrm{d}z + B_{+} \int_{\frac{p}{2}}^{\frac{3p}{2}} e^{-\frac{(x-z)^2}{2\sigma^2}} \mathrm{d}z \right), \tag{5.7}$$

where B_{-} and B_{+} provide the normalization for a given number of events for the negative and positive tails.

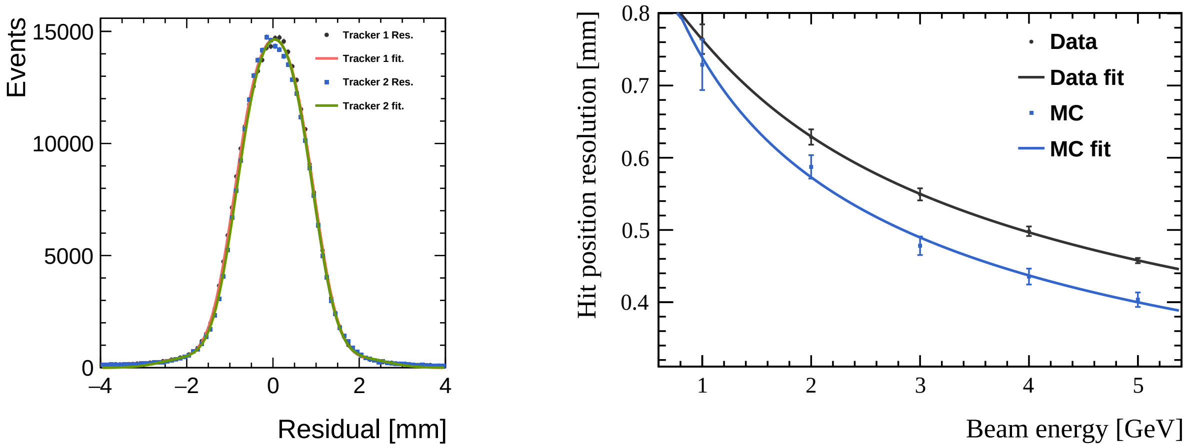

(a) **(b)**

Figure 5.19: (a) Residuals distributions between the hit position reconstructed in the calorimeter at 5 GeV, and each of tracker layers fitted with the sum $F(x) + G(x)$ from equations (5.6) and (5.7). (b) The extracted resolutions for each electron energy measured in the beam-test and in the simulation, fitted with Eq. (5.8).

The two residual distributions in Fig. 5.19(a) were fitted with the sum $F(x) + G(x)$, to extract the calorimeter resolution. The values of p found in the fit are in good agreement with the sensor pitch. The resolution of the position reconstruction in the calorimeter obtained from the fit is $\sigma = 460 \pm 20\ \mu$m. The distortion seen at the peak of the distribution is explained by the small asymmetry in the beam profile and by the circular geometry of the sensor which, in combination, result in a departure from the uniform distribution of the position uncertainty in the tracking planes. The same approach was applied to the results of the MC simulation, yielding an expected position resolution of 400 ± 15 μm for the same setup. The small difference can be potentially explained by the fact that the simulation does not reproduce perfectly the beam condition and does not take into account the beam profile. The presence of bad pads also contributes to worsening of the beam-test resolution.

The position resolution was extracted for beam energies between 1 and 5 GeV for each of the tracker planes. The average of the two results as a function of the beam energy, from data and MC simulation, is presented in Fig. 5.19(b). In the figure, the uncertainty was estimated as half of the difference between the two numbers used for averaging. The energy dependence was fitted with the function described in Eq. (5.8). This function is similar to the one used to describe the energy dependence of a calorimeter resolution and was used by the ATLAS collaboration [96] also to describe the energy dependence of the position resolution,

$$\sigma(E) = \frac{a}{\sqrt{E_{Beam}}} + \frac{b}{E_{Beam}} + c\ . \tag{5.8}$$

Assuming that this dependence holds at all energies, the results of the fit can be used to estimate the resolution of the calorimeter stack at the designed energy of the ILC beam of 250 GeV. By extrapolating to 250 GeV, a resolution of 115 μm is expected for the data, higher than the designed value of 55 μm that was obtained in the 250 GeV simulation for the full calorimeter [54]. However, the simulation of the calorimeter stack under test, yielded a resolution of 100 μm, consistent with the result from the data. Taking into account that the data and MC are in agreement for only one sixth of the full calorimeter thickness, and the resolution was calculated with a simplified method, the present result seems acceptable.

5.3.2 Energy response

Figure 5.20 shows the distributions of the energy deposited in the calorimeter, E_{dep}, for electrons at different beam energies collected during the beam-test. The deposited energy E_{dep} is obtained as the sum of energy deposited in all pads, after proper cuts, in the calorimeter,

$$E_{dep} = \sum_{n,k,l} E_{nkl} \ . \tag{5.9}$$

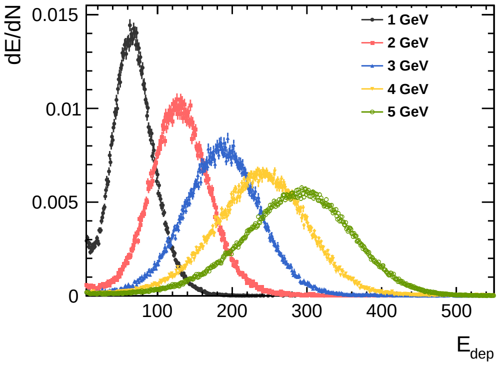

Figure 5.20: Distributions of the energy deposited, E_{dep}, in the calorimeter for electrons for the different beam energies.

The average deposited energy, $< E_{dep} >$, as a function of the electron beam energy is presented in Fig. 5.21. The measured raw values increase with increasing beam energy, with a tendency to deviate from a linear dependence. The deviation from linearity is caused by substantial energy leakage. The prototype consists of only seven layers, equivalent to less than 7 X_0, and not the required 30 layers in the design of LumiCal. Since the position of the shower maximum changes with energy, for different energies the percentage of the energy deposited varies with beam energy. The deposited raw energy is corrected by a factor extracted from a dedicated simulation, in which the test setup was extended to the full length of 30 absorber layers [97]. In the simulation, the fraction of energy deposited in the test setup was estimated for each beam energy. The dependence of the corrected $< E_{dep} >$ on beam energy is presented in Fig. 5.21 together with the corresponding linear fit. The ratio between the corrected and uncorrected average energy deposits to the linear fit results are shown in the bottom panel of Fig. 5.21. For the corrected $< E_{dep} >$, the departure from linearity is below 0.5%

Figure 5.22 presents the relative energy resolution for each beam energy measured in the beam-test. The relative energy resolution for each energy is the standard deviation, σ_E, obtained from the Gaussian fit to the distributions of the energy deposited, presented in Fig. 5.20, divided by the

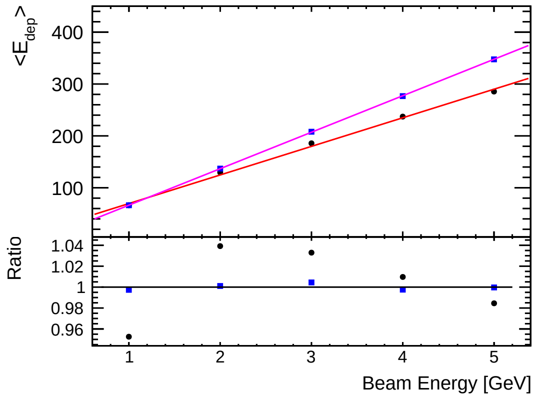

Figure 5.21: The average deposited energy, $< E_{dep} >$ as measured (black circles) and after corrections as explained in the text (blue squares), as a function of the electron beam energy compared to the respective linear fits. The ratio between the measured (corrected) $< E_{dep} >$ and the linear fit is shown in the bottom panel.

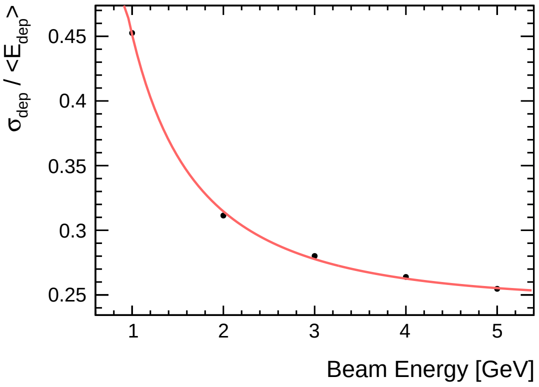

Figure 5.22: The relative energy resolution as a function of electron energy. The curve represents the fit result with Eq. (5.10) to extract the stochastic energy resolution.

average deposited energy, $< E_{dep} >$. The relative energy resolution is an important parameter of the calorimeter, and is usually parameterized by

$$\frac{\sigma_E}{E_{dep}} = \frac{a}{\sqrt{E_{Beam}}} + \frac{b}{E_{Beam}} + c\,, \tag{5.10}$$

where a represent the stochastic energy resolution term, b is referred to as the noise term and c is a free constant. From fitting Eq. (5.10) to Fig. 5.22, a stochastic energy resolution of $0.269 \pm 0.015\sqrt{GeV}$ is extracted. This is to be compared to the expected energy resolution of the LumiCal design of $0.205 \pm 0.0005\sqrt{GeV}$. The results are quite close, though the tested prototype consists of only seven absorber layers sampled with five sensor modules and the stochastic term is extracted at much lower energy than used for the LumiCal design.

5.3.3 One dimensional transverse shower profile

About 5% of randomly distributed channels in the prototype exhibit large noise levels. These channels are referred to as bad channels. As long as the bad channels are randomly spread, their effect on the shower development study is small. In case the bad channels are closely packed, like in layer 6 where 5 channels within pads 40-50 are considered as bad, the effect on the shower development study is large, especially since these pads lie within the core of the beam profile. The influence of these channels on the shower development study is eliminated by building a one dimensional, radial, transverse shower profile per layer, $\langle E_{ml} \rangle$, for all indexes m and l, only from properly working channels.

Since the particle position changes from event to event due to the transverse beam size of about 10 pads, the distribution E_n has to be shifted to the same origin. In both simulation and data analysis, the reconstructed hit position from the calorimeter data, described in Section 5.3.1, was used for the shift. Then the average values of E_n for each n, $< E_n >$, were calculated. To express the fact that the pad number was assigned a new value, the shifted pad index will be denoted by m. The index m = 0 is assigned to the pad in the central core of the shower and m ranges from -10 to +10 units of pads. An example of the distributions of E_{ml} for the shower core ($m = 0$) and pads with $m = -2$, and $m = -5$ for the sensor layer inserted after seven tungsten plates are shown in Figure 5.23.

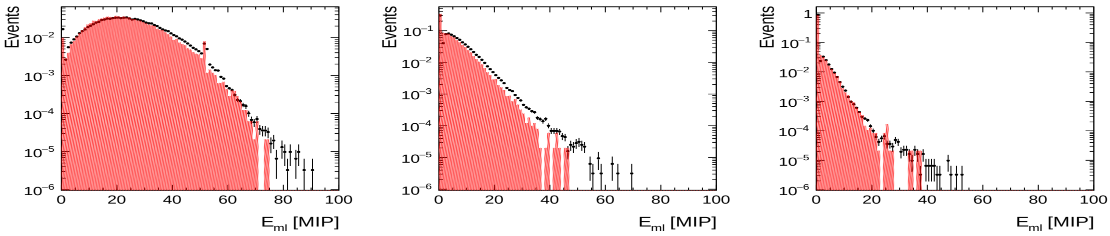

(a) **(b)** **(c)**

Figure 5.23: Distributions of deposited energy E_{ml} summed over two sensor sectors L1 and R1 in a layer after seven tungsten plates for radial pads which correspond to (a) the shower core, (b) two pads away from the core and (c) five pads away from the core.

An example of a one dimensional, radial, transverse shower profile, $\langle E_{ml} \rangle$, for all indexes $-10 \leq m \leq +10$ is presented in Fig. 5.24 for both layer 5 (after 5 absorber layers) in Fig. 5.24(a) and layer 6, (after 6 absorber layers) in Fig. 5.24(b). The small difference in the structure at the core of the two distributions indicates a residual miss-alignment of the two layers. As can be seen in both Fig. 5.23 and Fig. 5.24, data are well described by the simulation.

5.3.4 Longitudinal shower profile

The effect of the bad channels also affects the longitudinal shower profile studies. One way to calculate $\langle E_l^{layer} \rangle$ for each layer, l, is to take the mean of the sum of the energy deposited over all channels in the layer, as was done in Section 4.3.1 for the 2014 test beam analysis. A different approach is to use the one dimensional, radial, transverse shower profile per layer, $\langle E_{ml} \rangle$, by rewriting the average of the sum as the sum of the averages,

$$\langle E_l^{layer} \rangle = \langle \sum_m E_{ml} \rangle = \sum_m \langle E_{ml} \rangle . \tag{5.11}$$

The simulated data samples are used to estimate the impact of bad channels on the longitudinal shower profile. The bad channels are introduced for these samples at the exact same location as found in the beam-test data. The longitudinal shower profiles without and with bad channels are compared in Figure 5.25. The bad channels introduce a definite bias in the determination of the longitudinal evolution of the shower. Also shown in Figure 5.25 is the longitudinal shower profile obtained with bad channels included, after summing up over the individual transverse profiles for which the influence of bad channels was eliminated as described in Section 5.3.3. The summation over individual transverse radial profiles reproduces perfectly the longitudinal shower profile obtained without any bad channels.

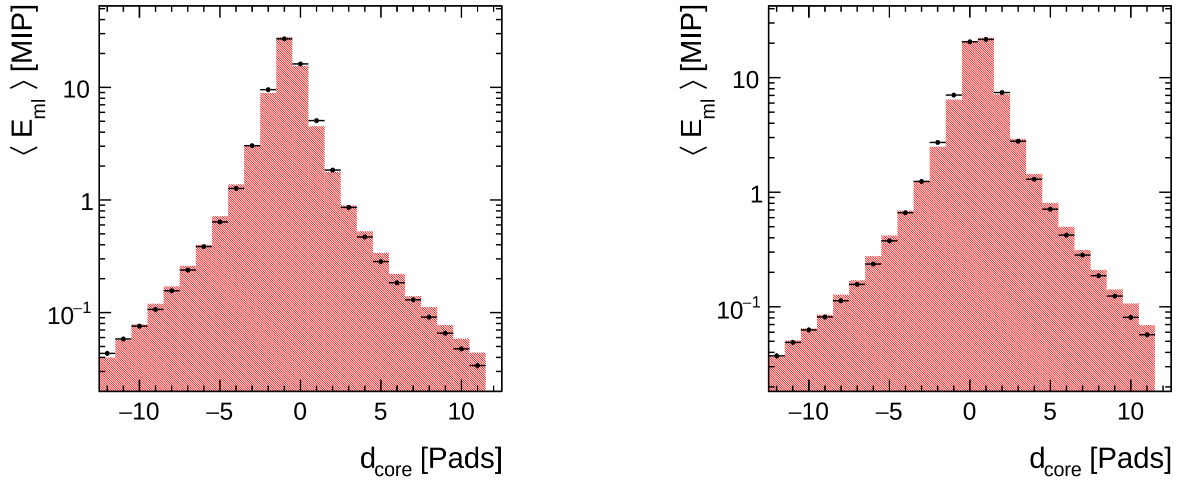

(a)

(b)

Figure 5.24: The one dimensional, radial, average transverse shower profile in terms of the corrected average energy depositions, $\langle E_{ml} \rangle$, in neighboring pads for layer 5 (Fig. 5.24(a)), placed after 5 absorber layers, and 6 (Fig. 5.24(a)) placed after 6 absorber layers. Also shown is the corresponding MC samples expectations.

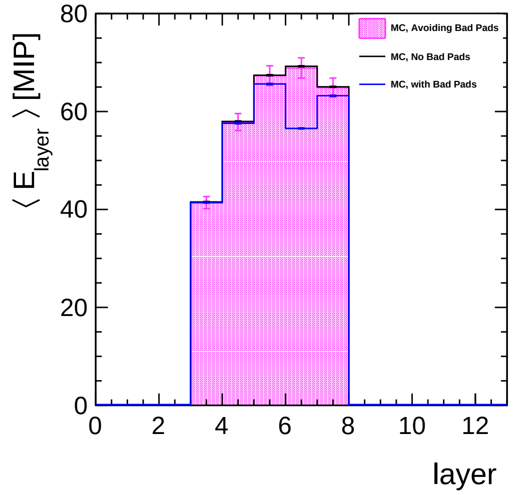

Figure 5.25: Longitudinal shower profile, as obtained in the simulation assuming no bad pad channels present (black histogram), assuming bad channels as observed in the data (blue histogram) and obtained after summing over individual transverse radial distributions which were reconstructed avoiding the bad channels.

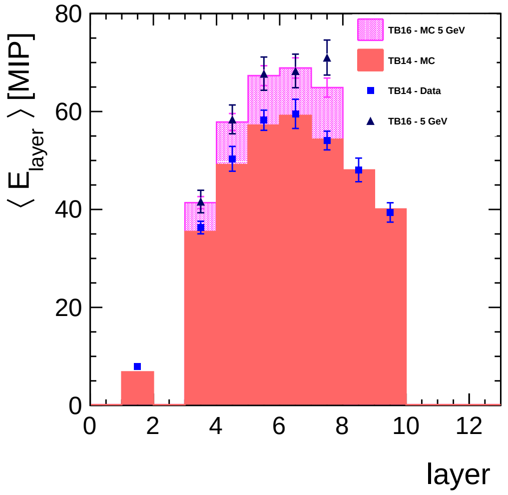

Figure 5.26: Longitudinal shower profile, as obtained in the 2014 and 2016 beam-test data for 5 GeV electrons compared to the respective simulations as described in the legend.

The development of the longitudinal shower profile is then measured using only events with properly working channels. For the 2016 beam-test and for 5 GeV electrons, Figure 5.26 shows the average deposited energy as a function of the layer number in the data and in the corresponding simulation. The distributions are in good agreement The simulation shape implies that the shower maximum is reached in layer 6, while in the data, layer 7 seems to indicate that the maximum is reached deeper. However, the excess over simulation in layer 7 is most probably due to calibration issues in a few pad channels. Since the APV25 board calibration was performed only for some channels in each layer, it is likely that some channels that were not directly calibrated exhibit deviations from the average behavior.

Figure 5.26 also presents a comparison of the longitudinal shower profile measured in the 2014 test beam data with the corresponding MC simulation (see Fig. 4.23). The shower shapes are similar for both beam-tests, while the difference in the amount of deposited energy per layer derives from the difference in the area sampled by the sensors in the two campaigns.

5.3.5 Effective Molière radius

For the measurement of the effective Molière radius of the LumiCal stack used in the 2016 beam-test, the same method as for the 2014 beam-test analysis was used with some small modifications. The main idea of this measurement is to solve numerically the definition that on average, 90% of the deposited energy lies inside a cylinder with a radius of one Molière radius, as expressed before in Eq. (4.11).

In order to solve Eq. (4.11), the parameters of the average radial energy density function $F_E(r)$ have to be determined from the data. Since LumiCal has long strip-like pads, it is possible to extract $F_E(r)$ by fitting its integrated radial distribution, described by Eq. (4.12) as $G_E(Y)$, to the average transverse profile, $\langle E_m \rangle$.

In the previous analysis, the arc shape of the pads was approximated for simplicity by a straight strip. The effect of this approximation was studied in a simulation [98] and it was shown that the difference between values of E_m calculated for pads of arc shape and for strip-like shape depends on the pad position with respect to the shower centre. It was estimated to amount to at most 2% and was included in the systematic uncertainty. This effect was suppressed in the data analysis because the sensor planes had limited number of pads connected to the readout, and some values of E_m could not be measured directly, but were recovered assuming a symmetry with respect to the shower core.

In the present study, the numerical integration is done using the correct geometry of the sensor pad instead of the Cartesian coordinates. To this end, it is convenient to use cylindrical coordinates which are linked to the sensor geometry. Changing the coordinates to $\vec{r} = \vec{r}\,' - \vec{R}_0'$, where $\vec{R}_0'$ is the position of the shower axis in the sensor reference frame, the pad-tower energy can be obtained by the integration

$$E_m = \int\limits_{\varphi'_{min}}^{\varphi'_{max}} \int\limits_{r'_n}^{r'_{n+1}} F_E(|\vec{r}\,' - \vec{R}_0'|) r' \, \mathrm{d}r' \mathrm{d}\varphi', \tag{5.12}$$

where φ'_{min} and φ'_{max} correspond to the sectors of the sensor and r'_n to the radius of the sensor pad n. The integration over φ' comprises the sectors L1 and R1. This corresponds to a coverage of about 40 mm. Since the transverse size of the beam is $\sigma_{x,y} \approx 4.2$ mm and the expected Molière radius is around 10 mm, the two sectors safely cover one Molière radius of the shower.

The trial function used to describe the average transverse energy profile of the shower was not changed, and has a Gaussian shape for the core part and a form inspired by the Grindhammer-Peters to account for the tails (see Eq. (4.14)). The energy E_n deposited in the pad number n depends on the shower position $\vec{R}'_0$ and pad position $\vec{r}'_n$. Since the beam transverse size is significantly smaller than the radius R'_0, the calculation of E_n is done for a value of R'_0 which corresponds to the position of the maximum in the beam profile. This maximum is observed in a pad with $n = 45$ and $r'_n = 161$ mm.

The average transverse profile of the electromagnetic shower is determined by summing the one dimensional, radial, transverse shower profiles per layer, $\langle E_{ml} \rangle$, over all detector layers,

$$\langle E_m \rangle = \sum_l \langle E_{ml} \rangle \ . \tag{5.13}$$

The dependence of the averaged transverse energy values, $\langle E_m \rangle$ on the distance from the core in units of pad size, was fitted by the function in Eq. (5.13). Results for data and MC samples obtained for 5 GeV electrons are shown in Figure 5.27. The fitted function reproduces the experimental and the simulated transverse shower profiles with an accuracy better than 5%. Figure 5.28 shows the right part of Eq. (4.11) as a function of the radial integration limit R for data and simulation with the horizontal line set at 90% shower containment as expected for the Molière radius. The result is (8.2 ± 0.1 (stat) ± 0.3 (syst)) mm, a value well reproduced by the simulation (8.5 ± 0.1) mm.

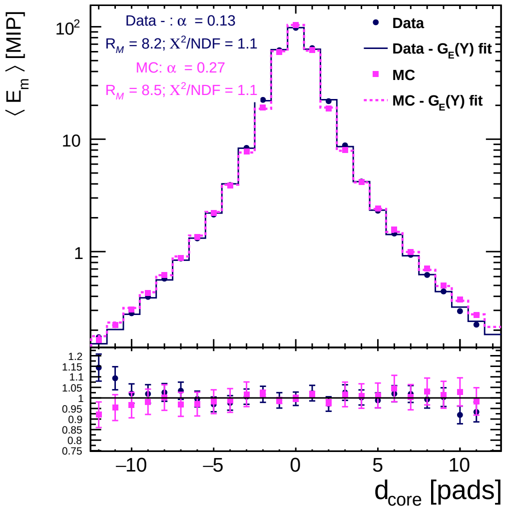

Figure 5.27: The average transverse shower profile, $\langle E_m \rangle$, as a function of the distance from the core, d_{core}, in units of the pad dimension (1.8 mm), for data (black circles) and MC samples (pink squares). The histograms are the results of fits to data and Monte Carlo simulation of the function in Eq. (5.13). The lower panel in the figure shows the ratio of the distributions to the fitted function, for data (black) and simulation (pink).

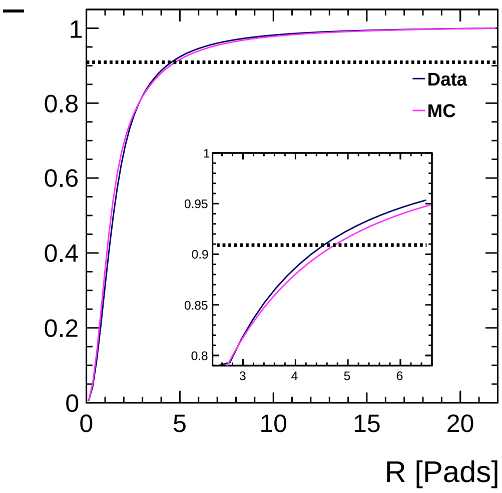

Figure 5.28: The ratio of the integrals in Eq. (4.11) using $F_E(r)$ obtained from the fit, as a function of the radius R in units of the pad dimension (1.8 mm), for data (black) and MC (pink). The insert shows an expanded view of the region $2 < R < 6$ pads.

5.3.6 Systematic uncertainties of the effective Molière radius

The study of the systematic uncertainties of the measured average energy deposition in the transverse direction $\langle E_{ml} \rangle$ includes the following contributions:

- uncertainty on the measured efficiency of the signal identification;
- uncertainty on the particle impact position measurement and on misalignment of detector planes;
- uncertainty due to bad channels;
- noise uncertainty;
- calibration uncertainty.

The uncertainty due to the efficiency of the signal reconstruction is evaluated by changing the efficiency according to high and low edges of the shaded area in Fig. 5.11. The result for the effective Molière radius changes by ± 0.16 mm.

The effect of layers misalignment on the effective Molière radius comes from the sum in Eq. (5.13) where the radial pad index m denotes pads in different layers which are assumed to be aligned in the longitudinal direction. Due to misalignment, the average lateral deposited energy $\langle E_m \rangle$ for a given distance from the shower core, determined by the index m, gets contribution from pads which are at different distances from the shower core. A similar effect arises from the uncertainty of the particle impact position. This uncertainty is estimated by calculating the effective Molière radius from simulations with perfectly aligned sensors and sensors displaced within the estimated misalignment as presented in Fig. 5.16.The change of the Molière radius is found to be 0.08 mm.

In spite of the fact that bad channels are avoided in the determination of the radial distribution, the simulation with and without bad channels results in a change of the effective Molière radius by 0.14 mm. Some of this effect could be due to statistical fluctuations, however to be on the conservative side, this change is treated as a systematic uncertainty.

The effect due to the usage of one single radius R'_0 in Eq. (5.12) for the calculation of E_m is estimated by selecting only events for which the particle impact position is limited to the sensor pad with the radial index $m = 45$. The relative change of the effective Molière radius is within 0.13 mm.

To estimate the effect of electronic noise on the final result, the simulation was performed with and without noise addition. The noise was generated as a Gaussian addition to the signal based on the values obtained for the data. The effect on the effective Molière radius was significantly below 1%.

Based on the APV25 calibration runs, a relative calibration uncertainty of 5% was assumed. It was added in quadrature to the statistical uncertainty for each value of $\langle E_{ml} \rangle$ in Eq. (5.13). As in the 2014 beam-test analysis, it was assumed that the calibration uncertainty does not introduce any correlations between the pads. To estimate the resulting uncertainty of the Molière radius, 1000 transverse shower profiles were generated by randomly varying each $\langle E_m \rangle$ using a Gaussian distribution function with a mean value corresponding to the measured $\langle E_m \rangle$ and a σ determined by the uncertainty. For each shower, the Molière radius was determined anew and the RMS of the resulting distribution is considered as a contribution to the statistical uncertainty of the effective Molière radius measurement.

The contributions to the systematic uncertainty are considered to be independent. The total systematic uncertainty on the effective Molière radius measurement is obtained by adding all the contributions in quadrature and amounts to 0.3 mm.

5.4 Summary

In the last LumiCal beam-test campaign during 2016, a new thin, sub-millimeter detector layer design was tested successfully. It allowed to operate and test, for the first time, a small prototype of the LumiCal calorimeter constructed according to the foreseen compact design.

During the tests, for the first time, the calorimeter energy resolution was estimated. It was extrapolated to the calorimeter design energy range and found to be compatible with simulation results used for the calorimeter design. Measurements of the shower position and of the longitudinal and transverse shower shapes were found to be in good agreement with the Monte Carlo simulations of the test setup. The effective Molière radius of this compact calorimeter prototype was determined at 5 GeV to be (8.2 ± 0.1 (stat) ± 0.3 (syst)) mm, a value well reproduced by the simulation (8.5 ± 0.1) mm. It is much smaller than the one determined for the calorimeter prototype used during the 2014 beam-test with larger air gaps between the tungsten plates, which yielded (24.0 ± 1.6) mm [89]. This improvement is clearly visible from the transverse shower profiles comparison presented in Fig. 5.29. These results indicate that it is possible to build a compact calorimeter consistent with the conceptual design, which is optimised for a high precision luminosity measurement in future e^+e^- collider experiments. Nevertheless the reconstruction of the electron shower position and the position resolution and bias should be carefully studied on the next test beams with a full length prototype.

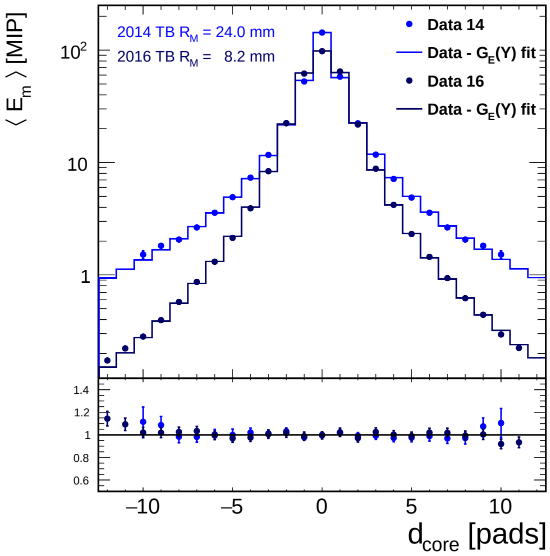

Figure 5.29: The average transverse shower profiles, as a function of distance from the core, and their fits (histogram), from the 2014 test (blue points presented in Fig. 4.33) and from the 2016 test (black points presented in Fig. 5.27). The lower part of the figure shows the ratio of the distributions to the fitted function.

CHAPTER 6

Summary

There is a consensus in the particle physics community that the next large accelerator facility should be an e^+e^- collider which can probe in depth the physics of the newly discovered Higgs boson. Any of these facilities will require a precision detector for luminosity measurements. And the highest precision can be achieved with a theoretically well controlled process, that of Bhabha scattering. Therefore a precise compact detector to identify the Bhabha process and to measure the rate of Bhabha scattering events is going to be the luminometer of choice. The design of the LumiCal based on a tungsten/silicon sensor sandwich calorimeter, as proposed by the FCAL Collaboration, is meant to address the precision requirements for such a detector.

This thesis addresses important issues in the design of such a calorimeter. It addresses the issue of how to test finely granulated silicon sensor planes in large bulk under controlled conditions. It provides a mechanical solution for constructing thin sensor layers which allow to achieve the optimal transverse shower development, limited by the inherent fluctuations in the absorption of an electromagnetic shower. It demonstrates that data collected during dedicated beam-tests as well as the shower development characteristics can be well understood and reproduced through Monte Carlo simulations based on the widely used GEANT4 tool.

Much remains to be done before a technical design report of the LumiCal design can be finalized. The performance of the final electronic readout will require extensive tests. The issue of sensor planes alignment during the construction and in situ needs to be addressed, as is the issue of in situ energy calibration. However, by controlling the issues addressed in this thesis, there is a reason to believe that such a design can be achieved, to a large extent through simulations. This statement is supported by the fact that the results of the beam-test data with a very restricted prototype calorimeter are reproduced by the appropriate MC simulations, which in case of a full LumiCal lead to a performance in line with the design requirements for a 250 GeV electron beam.

In recent years, the design of the detectors for an e^+e^- collider has undergone a tremendous review. The details of the LumiCal will have to follow suit and the contribution of this thesis will make it an easier task.

Bibliography

[1] *The Nobel Prize in Physics 2013*, `http://www.nobelprize.org/nobel_prizes/physics/laureates/2013/`.

[2] F. Englert and R. Brout, *Broken Symmetry and the Mass of Gauge Vector Mesons*, Phys. Rev. Lett. **13** (1964) 321–323, [,157(1964)].

[3] P. W. Higgs, *Broken symmetries, massless particles and gauge fields*, Phys. Lett. **12** (1964) 132–133.

[4] P. W. Higgs, *Broken Symmetries and the Masses of Gauge Bosons*, Phys. Rev. Lett. **13** (1964) 508–509, [,160(1964)].

[5] G. S. Guralnik, C. R. Hagen, and T. W. B. Kibble, *Global Conservation Laws and Massless Particles*, Phys. Rev. Lett. **13** (1964) 585–587, [,162(1964)].

[6] ATLAS Collaboration, G. Aad et al., *Observation of a new particle in the search for the Standard Model Higgs boson with the ATLAS detector at the LHC*, Phys.Lett. **B716** (2012) 1–29, `arXiv:1207.7214 [hep-ex]`.

[7] CMS Collaboration, S. Chatrchyan et al., *Observation of a new boson at a mass of 125 GeV with the CMS experiment at the LHC*, Phys.Lett. **B716** (2012) 30–61, `arXiv:1207.7235 [hep-ex]`.

[8] J. Bagger et al., *Discovering the quantum universe: the role of particle colliders*. DOE/NSF, [S.l.], 2006. `https://cds.cern.ch/record/2239607`.

[9] A. Arbey et al., *Physics at the e+ e- Linear Collider*, Eur. Phys. J. **C75** no. 8, (2015) 371, `arXiv:1504.01726 [hep-ph]`.

[10] K. Fujii et al., *Physics Case for the International Linear Collider*, `arXiv:1506.05992 [hep-ex]`.

[11] H. Baer, T. Barklow, K. Fujii, et al., *The International Linear Collider Technical Design Report - Volume 2: Physics*, `arXiv:1306.6352 [hep-ph]`.

[12] CLIC, CLICdp Collaboration, P. Roloff, R. Franceschini, U. Schnoor, and A. Wulzer, *The Compact Linear e^+e^- Collider (CLIC): Physics Potential*, `arXiv:1812.07986 [hep-ex]`.

[13] HL/HE WG2 group Collaboration, M. Cepeda et al., *Higgs Physics at the HL-LHC and HE-LHC*, `arXiv:1902.00134 [hep-ph]`.

[14] H. Abramowicz et al., *Higgs physics at the CLIC electron–positron linear collider*, Eur. Phys. J. **C77** no. 7, (2017) 475, `arXiv:1608.07538 [hep-ex]`.

[15] *The European Strategy for Particle Physics Update 2013. La stratégie européenne pour la physique des particules Mise à jour 2013. 16th Session of European Strategy Council*, `https://cds.cern.ch/record/1567258`.

[16] M. Mangano et al., *Future Circular Collider*, Tech. Rep. CERN-ACC-2018-0056, CERN, Geneva, Dec, 2018. `https://cds.cern.ch/record/2651294`. Submitted for publication to Eur. Phys. J. C.

[17] M. Benedikt et al., *Future Circular Collider*, Tech. Rep. CERN-ACC-2018-0057, CERN, Geneva, Dec, 2018. `https://cds.cern.ch/record/2651299`. Submitted for publication to Eur. Phys. J. ST.

[18] M. Benedikt et al., *Future Circular Collider*, Tech. Rep. CERN-ACC-2018-0058, CERN, Geneva, Dec, 2018. `https://cds.cern.ch/record/2651300`. Submitted for publication to Eur. Phys. J. ST.

[19] CEPC Collaboration,, *CEPC Conceptual Design Report: Volume 1 - Accelerator*, `arXiv:1809.00285 [physics.acc-ph]`.

[20] CEPC Collaboration, M. Dong and G. Li, *CEPC Conceptual Design Report: Volume 2 - Physics & Detector*, `arXiv:1811.10545 [hep-ex]`.

[21] E. Todesco and F. Zimmermann, eds., *Proceedings, EuCARD-AccNet-EuroLumi Workshop: The High-Energy Large Hadron Collider (HE-LHC10)*, CERN. CERN, Geneva, 2011. `arXiv:1111.7188 [physics.acc-ph]`. `http://cdsweb.cern.ch/record/1344820?ln=de`.

[22] A. Blondel and F. Zimmermann, *A High Luminosity e^+e^- Collider in the LHC tunnel to study the Higgs Boson*, `arXiv:1112.2518 [hep-ex]`.

[23] *Future Circular Collider Study Kickoff Meeting, University of Geneva*, `https://indico.cern.ch/event/282344/`, 2, 2014.

[24] *European Strategy for Particle Physics Update 2018 - 2020*, `https://council.web.cern.ch/en/content/european-strategy-particle-physics-update-2018-2020`.

[25] F. Zimmermann et al., *Future Circular Collider*, Tech. Rep. CERN-ACC-2018-0059, CERN, Geneva, Dec, 2018. `https://cds.cern.ch/record/2651305`. Submitted for publication to Eur. Phys. J. ST.

[26] K. Oide et al., *Design of beam optics for the Future Circular Collider e^+e^--collider rings*, Phys. Rev. Accel. Beams **19** no. 11, (2016) 111005, `arXiv:1610.07170 [physics.acc-ph]`, [Addendum: Phys. Rev. Accel. Beams 20,no.4, (2017) 049901].

[27] M. Zobov et al., *Test of crab-waist collisions at DAFNE Phi factory*, Phys. Rev. Lett. **104** (2010) 174801.

[28] T. Behnke, J. E. Brau, B. Foster, et al., *The International Linear Collider Technical Design Report - Volume 1: Executive Summary*, `arXiv:1306.6327 [physics.acc-ph]`.

[29] *European XFEL web site*, `https://www.xfel.eu/`.

[30] T. Barklow et al., *ILC Operating Scenarios*, `arXiv:1506.07830 [hep-ex]`.

[31] *Compact Linear Collider (CLIC)*, `http://clic.cern/`.

[32] L. Linssen et al., *Physics and Detectors at CLIC: CLIC Conceptual Design Report*, Tech. Rep. CERN-2012-003, CERN, Geneva, 2012. `arXiv:1202.5940 [physics.ins-det]`.

[33] M. Aicheler et al., *A Multi-TeV Linear Collider Based on CLIC Technology: CLIC Conceptual Design Report*, Tech. Rep. CERN-2012-007, CERN, Geneva, 2012.

[34] P. Lebrun et al., *The CLIC Programme: Towards a Staged e+e- Linear Collider Exploring the Terascale : CLIC Conceptual Design Report*, `arXiv:1209.2543 [physics.ins-det]`.

[35] CLIC, CLICdp Collaboration, M. J. Boland et al., *Updated baseline for a staged Compact Linear Collider*, `arXiv:1608.07537 [physics.acc-ph]`.

[36] T. I. C. Group, *The International Large Detector: Letter of Intent*, `arXiv:1006.3396 [hep-ex]`, DESY-2009-87, FERMILAB-PUB-09-682-E, KEK-REPORT-2009-6.

[37] E. Aihara, H. et al., *SiD Letter of Intent*, `arXiv:0911.0006 [physics.ins-det]`, Letter of Intent for SiD detector concept presented to ILC IDAG.

[38] CLICdp Collaboration, D. Arominski et al., *A detector for CLIC: main parameters and performance*, `arXiv:1812.07337 [physics.ins-det]`.

[39] M. Thomson, *Particle flow calorimetry and the PandoraPFA algorithm*, Nuclear Instruments and Methods in Physics Research Section A: Accelerators, Spectrometers, Detectors and Associated Equipment **611** no. 1, (2009) 25 – 40, `http://www.sciencedirect.com/science/article/pii/S0168900209017264`.

[40] S. Jadach, *Theoretical error of luminosity cross-section at LEP*, in *Proceedings, Electroweak precision data and the Higgs mass. Zeuthen, Germany, February 28-March 1, 2003*. `arXiv:hep-ph/0306083 [hep-ph]`.

[41] S. Jadach et al., *The path to 0.01% theoretical luminosity precision for the FCC-ee*, Phys. Lett. **B790** (2019) 314–321, `arXiv:1812.01004 [hep-ph]`.

[42] *Z physics at LEP1: Standard physics*, CERN-89-08-V-1, CERN-YELLOW-89-08-V-1.

[43] T. Behnke, J. E. Brau, P. N. Burrows, et al., *The International Linear Collider Technical Design Report - Volume 4: Detectors*, `arXiv:1306.6329 [physics.ins-det]`.

[44] ECFA/DESY LC Physics Working Group Collaboration, J. Aguilar-Saavedra et al., *TESLA: The Superconducting electron positron linear collider with an integrated x-ray laser laboratory. Technical design report. Part 3. Physics at an e+ e- linear collider*, `arXiv:hep-ph/0106315 [hep-ph]`.

[45] K. Moenig, *Physics Needs for the Forward Region*, Aug, 2004. Talk given at the FCAL Meeting, Zeuthen.

[46] *FCAL Collaboration*,. URL: `http://fcal.desy.de/`.

[47] C. Grah and A. Sapronov, *Beam parameter determination using beamstrahlung photons and incoherent pairs*, JINST **3** (2008) P10004.

[48] H. Abramowicz et al., *Forward Instrumentation for ILC Detectors*, JINST **5** (2010) P12002, `arXiv:1009.2433 [physics.ins-det]`, DESY-10-142.

[49] O. Karacheban et al., *Investigation of a direction sensitive sapphire detector stack at the 5 GeV electron beam at DESY-II*, JINST **10** no. 08, (2015) P08008, `arXiv:1504.04023 [physics.ins-det]`.

[50] S. Schuwalow, *Design of ILD forward region - L**, Presented at the 29 FCAL Workshop, Tel-Aviv, URL: https://agenda.linearcollider.org/event/7354/contributions/37350/attachments/30534/45672/Design_of_ILD_forward_region_for_reduced_L_star.pdf, 9, 2016.

[51] Y. SATO, *Study of PAIR-MONITOR for ILD*, pp. , 95–98. INN VInca, 2008. URL: http://www.vin.bg.ac.rs/hep/pub/FCAL_Belgrade.pdf.

[52] R. Ingbir, *A Luminosity Detector for the ILC*, MSc. thesis, Tel Aviv University, 2006.

[53] H. Abramowicz, R. Ingbir, S. Kananov, and A. Levy, *A luminosity detector for the International Linear Collider*, LC-DET-2007-006.

[54] I. Sadeh, *Luminosity Measurement at the International Linear Collider*, MSc. thesis, Tel Aviv University, 2010. arXiv:1010.5992.

[55] I. Levy, *Detector devlopment for the instruments in the forward region of future linear colliders*, MSc. thesis, Tel Aviv University, Mar, 2012. CERN-THESIS-2012-346.

[56] V. Lukianchuk, *Energy linearity and resolution of the LHCal calorimeter of the ILD detector for the ILC experiment*, MSc. thesis, National University of Kyiv, Kyiv, June, 2016.

[57] O. Rosenblat, *Uniformity of detector prototypes for instrumentation in the very forward region of future linear colliders*, MSc. thesis, Tel Aviv University, 2016.

[58] M. Bergholz, *I/V and C/V Measurements on Hamamatsu Si - Detectors*, Jun, 2009. https://indico.desy.de/getFile.py/access?contribId=14&sessionId=0&resId=0&materialId=slides&confId=2000. FCAL Meeting, Zeuthen.

[59] A. L. Poley, *Studies of adhesives and metal contacts on silicon strip sensors for the ATLAS Inner Tracker*. PhD thesis, Apr, 2018.

[60] *200 mm Semi-automated Probe System DATA sheet*, https://www.cascademicrotech.com/files/PA200-DS.pdf. by Cascade Microtech.

[61] E. J.Bwocki, W.Daniluk and others., *Silicon Sensors Prototype for LumiCal Calorimeter*, EUDET-Memo-2009-07.

[62] *The center of research excellence in the quantum universe*, http://www.weizmann.ac.il/icore/quantum_universe/.

[63] F. M. Pitters et al., *ARRAY: An Open Source, Modular and Probe-Card based System with Integrated Switching Matrix for Characterisation of Large Area Silicon Pad Sensors*, Tech. Rep. CLICdp-Pub-2019-002, CERN, Geneva, Mar, 2019. https://cds.cern.ch/record/2668752.

[64] CMS Collaboration, C. Seez, T. Virdee, et al., *The Phase-2 Upgrade of the CMS Endcap Calorimeter*, Tech. Rep. CERN-LHCC-2017-023. CMS-TDR-019, CERN, Geneva, Nov, 2017. http://cds.cern.ch/record/2293646. Technical Design Report of the endcap calorimeter for the Phase-2 upgrade of the CMS experiment, in view of the HL-LHC run.

[65] *ARRAY at the CERN Open Hardware Repository*, March, 2019. https://www.ohwr.org/project/array.

[66] FCAL Collaboration, H. Abramowicz et al., *Performance of fully instrumented detector planes of the forward calorimeter of a Linear Collider detector*, JINST **10** no. 05, (2015) P05009, `arXiv:1411.4431 [physics.ins-det]`.

[67] M. Bregant et al., *Assembly and validation of the ALICE silicon microstrip detector*, Nucl. Instrum. Meth. **A570** (2007) 312–316.

[68] *CERN East Area documentation.*, `http://sba.web.cern.ch/sba/BeamsAndAreas/East/East.htm`.

[69] F.-X. Nuiry, *Collected documents on the FCAL-AIDA precision mechanical infrastructure and tungsten plates.*, `https://edms.cern.ch/document/1475879/`.

[70] M. Idzik, S. Kulis, and D. Przyborowski, *Development of front-end electronics for the luminosity detector at ILC*, Nuclear Instruments and Methods in Physics Research Section A: Accelerators, Spectrometers, Detectors and Associated Equipment **608** no. 1, (2009) 169 – 174, `http://www.sciencedirect.com/science/article/pii/S0168900209013151`.

[71] M. Idzik et al., *A 10-Bit Multichannel Digitizer ASIC for Detectors in Particle Physics Experiments*, IEEE Transactions on Nuclear Science **59** no. 2, (2012) 294–302.

[72] S. Kulis et al., *A general purpose multichannel readout system for radiation detectors*, Journal of Instrumentation **7** no. 01, (2012) T01004–T01004, `https://doi.org/10.1088%2F1748-0221%2F7%2F01%2Ft01004`.

[73] J. Baudot et al., *First test results of MIMOSA-26: A fast CMOS sensor with integrated zero suppression and digitized output*,.

[74] D. G. Cussans, *Description of the JRA1 Trigger Logic Unit (TLU), v0.2c*, EUDET-Memo-2009-04 (2009), `http://www.eudet.org/e26/e28/e42441/e57298/EUDET-MEMO-2009-04.pdf`.

[75] J. Baudot, *TAF short manual*, `http://www.iphc.cnrs.fr/IMG/pdf/taf_shortdoc.pdf`.

[76] T. Lawrence Bienz, *Strangeonium Spectroscopy at 11 Gev/c and Cherenkov Ring Imaging at the SLD*. PhD thesis, Stanford University, July, 1990. DOI:10.2172/6641103.

[77] J. Moron, *Development of novel low-power, submicron CMOS technology based, readout system for luminosity detector in future linear collider*. PhD thesis, AGH - UST, Cracow, 7, 2015. Ph. D. dissertation.

[78] J. Aguilar, *Luminosity detector at ILC: Monte Carlo simulations and analysis of test beam data*, MSc. thesis, WFiIS AGH and IFJ-PAN, Krakow, February, 2012.

[79] GEANT4 Collaboration, S. Agostinelli et al., *GEANT4: A Simulation toolkit*, Nucl. Instrum. Meth. **A506** (2003) 250–303.

[80] R. Brun and F. Rademakers, *ROOT: An object oriented data analysis framework*, Nucl. Instrum. Meth. **A389** (1997) 81–86.

[81] P. Mora de Freitas and H. Videau, *Detector simulation with MOKKA / GEANT4: Present and future*, pp. , 623–627. 2002. `http://www-library.desy.de/cgi-bin/showprep.pl?lc-tool03-010`.

[82] *QGSP BERT Reference Physics Lists.*, http://geant4-userdoc.web.cern.ch/geant4-userdoc/UsersGuides/PhysicsListGuide/html/reference_PL/QGSP_BERT.html.

[83] E. Longo and I. Sestili, *Monte Carlo Calculation of Photon Initiated Electromagnetic Showers in Lead Glass*, Nucl. Instrum. Meth. **128** (1975) 283, [Erratum: Nucl. Instrum. Meth.135,587(1976)].

[84] Particle Data Group Collaboration, C. Patrignani et al., *Review of Particle Physics*, Chin. Phys. **C40** no. 10, (2016) 100001.

[85] B. Rossi and K. Greisen, *Cosmic-ray theory*, Rev. Mod. Phys. **13** (1941) 240–309.

[86] G. Grindhammer and S. Peters, *The Parameterized simulation of electromagnetic showers in homogeneous and sampling calorimeters*, in *International Conference on Monte Carlo Simulation in High-Energy and Nuclear Physics - MC 93 Tallahassee, Florida, February 22-26, 1993*. 1993. arXiv:hep-ex/0001020 [hep-ex].

[87] R. Wigmans, *Calorimetry: Energy Measurement in Particle Physics*. International series of monographs on physics. Oxford University Press, 2017.

[88] H. Jansen et al., *Performance of the EUDET-type beam telescopes*, EPJ Tech. Instrum. **3** no. 1, (2016) 7, arXiv:1603.09669 [physics.ins-det].

[89] FCAL Collaboration, H. Abramowicz et al., *Measurement of shower development and its Molière radius with a four-plane LumiCal test set-up*, Eur. Phys. J. **C78** no. 2, (2018) 135, arXiv:1705.03885 [physics.ins-det].

[90] M. Idzik, *FLAME - readout ASIC for luminosity calorimeter at future linear collider*, Presented at twepp 2018, topical workshop on electronics for particle physics, 2018. https://indico.cern.ch/event/697988/contributions/3055910/attachments/1718342/2772974/idzik_TWEPP2018_FLAME.pdf.

[91] S. Martoiu et al., *Development of the scalable readout system for micro-pattern gas detectors and other applications*, JINST **8** (2013) C03015.

[92] S. Martoiu, H. Muller, and J. Toledo, *Front-end electronics for the Scalable Readout System of RD51*, pp. , 2036–2038. 2011.

[93] M. J. French et al., *Design and results from the APV25, a deep sub-micron CMOS front-end chip for the CMS tracker*, Nucl. Instrum. Meth. **A466** (2001) 359–365.

[94] A. Z. V. Bhopatkar, M. Hohlmann, *Measurement of the Charge Induced on the Readout Strips of a GE1/1 Detector Prototype for the CMS Muon Endcap GEM Upgrade.*, Cms internal note, cms in -2017/001., 2017.

[95] O. Borisov, *Thin LumiCal Module Performance During TB2016*, Presented at 32 FCAL workshop, Krakow, URL: https://indico.cern.ch/event/697164/contributions/2987416/attachments/1647586/2633796/lumical_thin_module.pdf, 5, 2018.

[96] R. Sacco, *Position resolution of an ATLAS electromagnetic calorimeter module*, ATL-LARG-2003-008.

[97] H. Abramowicz et al., *Performance and Moli'ere radius measurements using a compact prototype of LumiCal in an electron test beam*, `arXiv:1812.11426 [physics.ins-det]`.

[98] FCAL Collaboration, O. Borysov, *Beam Tests of a Multilayer LumiCal Prototype*, in *Proceedings, International Workshop on Future Linear Colliders 2016 (LCWS2016): Morioka, Iwate, Japan, December 05-09, 2016.* 2017. `arXiv:1703.09955 [physics.ins-det]`.

תקציר

מדידת עוצמת הארה של מאיץ אלקטרון פוזיטרון קווי עתידי, תתבצע בגלאי אנרגיה קומפקטי ויעודי הצפוי באזור הקדמי של הניסוי. הגלאי מתוכנן כגלאי אנרגיה שכבתי הבנוי משכבות של סיליקון וטנגסטן. מאמץ המחקר והפיתוח הנערך ע"י קבוצת שיתוף הפעולה FCAL מכוון לקראת אב טיפוס שלם של הגלאי שידגים באופן מעשי את ביצועי הגלאי המלא.

שתי שיטות לבדיקה אוטומטית של חיישני סיליקון שימשו למדידות ואפיון של אב הטיפוס של חיישני הסיליקון המיועדים לשימוש בגלאי. במדידות אלו נמדדו הקיבול הסופי, מתח המחזור המלא, צפיפות האלוחים השליליים והזרם השחור של כל רכיב חישה (דיודה) בחיישן.

אב טיפוס ראשוני המורכב ממערך של ארבעה חיישני סיליקון נוסה בקו-קרן T9 במאיץ PS השוכן ב-CERN בשנת 2014. אב טיפוס נוסף, חדש, וקומפקטי המשתמש במערך של לוחות חיישן דקים וחדשים, נבדק ב-DESY, בקרן אלקטרונים באנרגיה של 1 עד 6 מיליארד אלקטרון וולט (GeV). בניסויים אלו נבדקו תגובות הגלאי, התפתחות המטר (shower) האלקטרומגנטי וכושר ההפרדה בשחזור המיקום ובמדידת והאנרגיה. רדיוס מוליר (Moliere) האפקטיבי של אבות הטיפוס נמדד בעזרת מודל פרמטרי של צורת המטר בכיוון הניצב. עבור אב הטיפוס הראשון נמדד ערך של $24 \pm 0.6(stat.) \pm 1.5(syst.)mm$, בעוד לאב הטיפוס הקומפקטי נמדד ערך נמוך משמעותית של $8.2 \pm 0.1(stat.) \pm 0.3(syst.)mm$. הסכמה טובה מאד התגלתה בהשוואת התוצאות המדודות למול תוצאות ההדמיה הממוחשבת. הערך הנמוך שהושג עבור רדיוס מוליר האפקטיבי של האב-טיפוס הקומפקטי מראה שהגלאי הקומפקטי המלא יוכל לבצע מדידות הארה בדיוק הרצוי בזמן ביצוע אמת של הניסוי.

להגר ובנותינו,
ולזכרה של סבתא הלינה.

העבודה הוכנה בחוג לפיזיקת החלקיקים של אוניברסיטת תל-אביב,
בהדרכתם של פרופ' **הלינה אברמוביץ** ופרופ' **אהרן לוי.**

The Raymond and Beverly Sackler
School of Physics and Astronomy
The Raymond and Beverly Sackler
Faculty of Exact Sciences
Tel Aviv University

בית הספר לפיזיקה ולאסטרונומיה
ע״ש ריימונד ובברלי סאקלר
הפקולטה למדעים מדויקים
ע״ש ריימונד ובברלי סאקלר
אוניברסיטת תל אביב

RAMAT AVIV, 69978 TEL AVIV, ISRAEL

פיתוח גלאים לקראת מדידה מעשית של עוצמת הארה באזור הקידמי של מאיצי אלקטרון-פוזיטרון קווים עתידיים

חיבור זה הוגש לסנאט של אוניברסיטת תל-אביב,
כחלק מהדרישות לקבלת תואר "דוקטור לפילוסופיה"

על-ידי

איתמר לוי

מאי 2019

העבודה הוכנה בהדרכתם של
פרופ' **הלינה אברמוביץ** ופרופ' **אהרן לוי.**